Fermilab Library
0 1160 0003735 2

Search for the Top Quark in Electron-Muon Events in the Collider Detector at Fermilab

by

Milciades Contreras

LIBOFFCE
FERMILAB
THESIS

SEARCH FOR THE TOP QUARK IN ELECTRON-MUON EVENTS IN THE COLLIDER DETECTOR AT FERMILAB

A Dissertation

Presented to

The Faculty of the Graduate School of Arts and Sciences

Brandeis University

Department of Physics

In Partial Fulfillment
of the Requirements for the Degree of
Doctor of Philosophy

by
Milciades Contreras
April, 1990

This dissertation, directed and approved by the candidate's Committee, has been accepted and approved by the Graduate Faculty of Brandeis University in partial fulfillment of the requirements for the Degree of

DOCTOR OF PHILOSOPHY

Dean, Graduate School of Arts and Sciences

Dissertation Committee

James Bensinger, Chairman

Laurence F. Abbott

John F. C. Wardle

J. Scott Whitaker (Boston Univ)

ABSTRACT

SEARCH FOR THE TOP QUARK IN ELECTRON-MUON EVENTS IN THE COLLIDER DETECTOR AT FERMILAB

(A Dissertation Presented to the Faculty of the Graduate School of Arts and Sciences of Brandeis University, Waltham, Massachussetts)

by Milciades Contreras

A search for $t\bar{t} \to e\mu + X$ in $p\bar{p}$ collisions at $\sqrt{s} = 1.8$ TeV is described. The production and decay of top quark-antiquark pairs is considered in the context of the Standard Model. The analysis is based on data with an integrated luminosity of 4.4 pb^{-1} recorded with the Collider Detector at Fermilab in the 1988-1989 run. An upper limit on the $t\bar{t}$ cross section is obtained and the top quark in the mass range 28 to 72 GeV/c^2 is excluded at the 95% CL. The same limits apply to a possible fourth generation, charge $-\frac{1}{3}$, b' quark, decaying via the charged current.

Acknowledgements

I want to thank my advisor Jim Bensinger for giving me the opportunity to work at CDF and for his continuous help, support and encouragment throughout my years as a graduate student. I am especially grateful to my friend and colleague G.P. Yeh for his participation in the analysis and for a great time looking for the top. Many thanks to Bill Foster for important contributions to the analysis and to John Yoh for many useful discussions and for sharing his enthusiasm for physics.

I wish to thank all my colleagues at CDF for their dedication to the experiment. Many people helped with the analysis in one way or another. I want to thank Peter Berge, Morris Binkley, Craig Blocker, Jim Freeman, Lina Galtieri, Mike Gold, Phil Kesten, Aseet Mukherjee, Cathy Newman-Holmes, Adam Para, Jim Proudfoot, J.J Schmidt, David Smith, Shlomit Tarem, Paul Tipton, Fumi Ukegawa, Tom Westhusing and Barry Wicklund. Special thanks to Craig Blocker, Steve Behrends, Jim Bensinger and G.P. Yeh for a careful reading of the thesis and for their comments and suggestions.

My greatest appreciation goes to my family for their love and support. This thesis is dedicated to my wife Josefina, my son Vicente and to my parents and sisters.

Table of Contents

Abstract ii

Acknowledgements iii

List of Tables v

List of Figures vii

1. INTRODUCTION 1

1.1. STATUS OF SEARCHES FOR THE TOP QUARK 3

1.2. PHENOMENOLOGICAL CONSTRAINTS 4

1.3. HADRONIC PRODUCTION OF HEAVY QUARKS 8

1.4. FRAGMENTATION AND DECAY OF HEAVY QUARKS 10

1.5. SIGNATURES FOR THE TOP QUARK AT THE TEVATRON . 12

2. EXPERIMENT SETUP 36

2.1. THE TEVATRON 36

2.2. THE CDF DETECTOR 37

2.2.1. Tracking 38

2.2.2. Calorimetry 40

2.2.3. Muon Detectors 43

2.2.4. Trigger 44

3. DATA ANALYSIS I : EVENT SELECTION 61

3.1. TRIGGERING 61

3.1.1. Inclusive Electron Trigger 61

3.1.2. Inclusive Muon Trigger 62

3.1.3. Electron-Muon Trigger 63

3.2. DATA PROCESSING 64

3.3. ELECTRON SELECTION 65

3.3.1. Electron Selection Criteria 65

3.3.2. Electron Selection Efficiency 70

3.4. MUON SELECTION 72

3.4.1. Muon Selection Criteria 73

3.4.2. Muon Selection Efficiency 75

3.5. CONCLUSIONS 77

4. DATA ANALYSIS II : COMPARISON WITH MONTE CARLO 115

4.1. MONTE CARLO DATA SAMPLES 115

4.2. DEFINITION OF THE $t\bar{t} \to e\mu + X$ SIGNAL REGION 116

4.3. EFFICIENCIES FOR $t\bar{t} \to e\mu + X$ 117

4.3.1. Geometrical and P_T cuts 118

4.3.2. Electron Reconstruction Efficiency 120

4.3.3. Muon Reconstruction Efficiency 121

4.3.4. The total $t\bar{t} \to e\mu + X$ efficiency 122

4.4. THE DATA 123

4.5. COMPARISON WITH $b\bar{b}$ BACKGROUND MONTE CARLO . . 127

4.6. BACKGROUNDS TO THE CANDIDATE EVENT 129

4.7. CONCLUSIONS 132

5. DATA ANALYSIS III : TOP QUARK MASS LIMITS 188

5.1. SYSTEMATIC UNCERTAINTIES 188

5.2. LIMITS ON $t\bar{t}$ PRODUCTION 190

5.3. LIMITS ON THE MASS OF THE t' QUARK 193

6. CONCLUSION AND OUTLOOK 198

References 202

List of Tables

1.1. The three generations of quarks and leptons. The top quark and the tau-neutrino have not been observed. Quark masses are indicative only. Other masses were taken from reference [35]. 14

1.2. Heavy quark production cross section in $p\bar{p}$ collisions at 1.8 TeV. From reference [28]. 15

2.1. Summary of Calorimeter Characteristics 48

3.1. Electron selection cuts and their efficiencies for electrons from $Z^0 \rightarrow e^+e^-$ going into the fiducial region of the calorimeter. 78

3.2. Muon selection cuts and their efficiencies from $Z^0 \rightarrow \mu^+\mu^-$ for CMUOs (muons with an associated muon chamber track) and for CMIOs (muons with no associated track going into the fiducial region of the calorimeter). 79

4.1. The contributions to the $t\bar{t} \rightarrow e\mu + X$ signal : i) both leptons come directly from the top decay; ii) at least one lepton is coming from the decay of a τ; and iii) leptons coming from the decays of a b or c quark are involved 133

4.2. Acceptance to the η and P_T cuts normalized to the double semileptonic branching ratio of $\frac{2}{81}$. The acceptance has been taken as the intermediate value between the ISAJET and PAPAGENO calculations, the associated systematic uncertainty is half the difference of the acceptances. 133

4.3. The top electron efficiencies. ϵ^e_{top} is the total electron detection efficiency inside the fiducial volume, including losses due to overlapping particles and to the photon conversion cuts. Only the Monte Carlo statistical uncertainty is included. 134

4.4. The top muon efficiencies. ϵ^μ_{top} is the total muon detection efficiency inside the fiducial volume, including losses due to overlap with other particles. Only Monte Carlo statistical errors are included. . 135

4.5. The $t\bar{t} \rightarrow e\mu + X$ efficiencies for: i) the P_T cuts , ii) geometric acceptance (after P_T cuts), iii) dilepton reconstruction (after P_T and geometry cuts), and iv) total. Only the Monte Carlo statistical uncertainty is included. 136

4.6. Backgrounds to $t\bar{t} \rightarrow e\mu + X$. Here, $\sigma_{obs} = \sigma \cdot Br \cdot \epsilon_{Geom,P_T} \cdot \epsilon^{e\mu}_{Rec}$. 137

4.7. Characteristics of the top candidate event. Calorimeter E_T is used in the P_T column for the electron and jet clusters. 138

5.1. The systematic uncertainties on the expected number of $t\bar{t} \rightarrow e\mu + X$ events as a function of M_{top}. 194

5.2. The upper limits on the number of $e\mu$ events and on the $t\bar{t}$ production cross section , together with the theoretical cross section. $A^{e\mu}_{t\bar{t}}$ is the $e\mu$ channel acceptance. 195

6.1. The total $t\bar{t}$ production cross section, together with estimates of the CDF detected cross sections into the $e\mu$ and $l + jets$ channels. 201

6.2. The estimated number of detected $e\mu$ events, and of $l + jets$ events with at least one B jet tagged by the silicon vertex detector, for integrated luminosities of 20 pb^{-1} and 100 pb^{-1}. 201

List of Figures

1.1. Feynman diagrams for the process $e^+e^- \to b\bar{b}$. 16

1.2. Contributions to semileptonic b decay from a)charged current decay and b) neutral current decay. 17

1.3. Box diagrams for a) $B_d^0\bar{B}_d^0$ and b) $B_s^0\bar{B}_s^0$ mixing. 18

1.4. Diagrams for one-loop radiative corrections. 19

1.5. The electroweak correction factor Δr as a function of M_{top}. From reference [19]. 20

1.6. The $\pm 1\sigma$ uncertainties in $\sin^2\theta_W$ by various determinations. See the text for an explanation. From reference [21]. 21

1.7. Lowest order Feynman diagrams for heavy quark production. . . . 22

1.8. Feynman diagrams for a) gluon splitting and b) flavor excitation. 23

1.9. The top quark cross section vs. μ at 1.8 TeV. From reference [27]. 24

1.10. The $t\bar{t}$ predicted cross section by Altarelli et. al [28], based on the next-to-leading order calculation by Nason, Dawson, and Ellis [26]. 25

1.11. The bottom quark cross section vs. μ at 1.8 TeV. From reference [27]. 26

1.12. An example of top quark fragmentation. 27

1.13. The fragmentation functions for $c \to D^*$ and $b \to B$ from the Argus and Mark-J experiments, compared to Peterson model for $\epsilon = 0.18$ and $\epsilon = 0.018$ respectively. From reference [31]. 28

1.14. Comparison of the $Q = c, b, t$ fragmentation functions in the Peterson model, assuming $\epsilon = 0.40/m_Q^2$ with $m_c = 1.5, m_b = 4.7$ and $m_t = 40$ GeV/c^2. From reference [31]. 29

1.15. Decay width Γ_{top} for the top quark as a function of its mass. At low mass $\Gamma_{top} \sim M_{top}^5$, at large mass $\Gamma_{top} \sim M_{top}^3$. From reference [32]. 30

1.16. The weak charged current decay of the top quark. 31

1.17. The fractional energy spectra $z_i = 2E_i/m_Q$ of decay leptons and quarks for b and c semileptonic decays. From reference [31]. . . . 32

1.18. The charged lepton spectrum in $t \to bl\nu$ for different top masses. The dashed lines correspond to the approximation of zero W width. From reference [33]. 33

1.19. The bottom quark spectrum in $t \to bl\nu$ for different top masses. From reference [33]. 34

1.20. Parton final states and event topologies for a) W decay and b) top pair production. Only final states containing at least one electron or muon from the top decay are shown. The branching ratios are indicated in parentheses. 35

2.1. The Fermilab accelerator complex. 49

2.2. The Antiproton Source. 50

2.3. A squematic perspective view of the CDF detector. 51

2.4. A cut-away view of the forward half of the CDF. The detector is forward-backward symmetric about the interaction point. 52

2.5. Schematic view of two of the VTPC modules. 53

2.6. End view of the Central Tracking Chamber showing the disposition of the superlayers and cells within the superlayers. 54

2.7. A 90° section of hadron calorimeter towers. Module or calorimeter system boundaries are indicated with heavy lines. The ϕ coverage of the EM calorimeters is complete out to $|\eta| = 4.2$. 55

2.8. A central calorimeter wedge, showing the light-gathering system. . 56

2.9. Quadrant of the calorimeter where A, B, C show the central, end-wall and plug respectively. 57

2.10. Central muon chamber location with respect to a central calorimeter wedge. 55
2.11. Cross section of a central muon chamber. 59
2.12. One plane of beam-beam counters viewed from the beam-line. . . 60
3.1. The 12 GeV Electron trigger efficiency from 7 GeV Electron trigger data. From reference [59]. 80
3.2. The radius of conversion R_c for low mass pairs. Two clear peaks are present, distinguishing pairs from Dalitz decays and conversions at the VTPC inner wall (at 2.5 cm) from pairs from conversions at the outer VTPC wall and inner wall of the CTC (at $\sim$ 28 cm). . . 81
3.3. The $HAD/(EM + HAD)$ distribution for 50 GeV test-beam electron and charged pion showers and for electrons from $W \rightarrow e\nu$ decays. From reference [66]. 82
3.4. The strip chamber χ^2 distribution for 50 GeV test-beam electron and charged pion showers and for electrons from $W \rightarrow e\nu$ decays From reference [66]. 83
3.5. The invariant mass ($M_{e^+e^-}$) for the dielectron sample. 84
3.6. The HAD/EM distribution for the $Z^0 \rightarrow e^+e^-$ sample. 85
3.7. The Lateral Sharing ($Lshr$) distribution for the $Z^0 \rightarrow e^+e^-$ sample. 86
3.8. The track to strip matching in azimuth ($R\delta\phi$) for the $Z^0 \rightarrow e^+e^-$ sample. 87
3.9. The track to strip matching along the beam direction (δz) for the $Z^0 \rightarrow e^+e^-$ sample. 88
3.10. The strip chamber χ^2 distribution in the azimuthal view (χ^2_ϕ) for the $Z^0 \rightarrow e^+e^-$ sample. 89
3.11. The strip chamber χ^2 distribution in the beam direction (χ^2_z) for the $Z^0 \rightarrow e^+e^-$ sample. 90
3.12. The E/P distribution for the $Z^0 \rightarrow e^+e^-$ sample. 91
3.13. The strip chamber χ^2 in the azimuthal view (χ^2_ϕ) versus E/P for the $Z^0 \rightarrow e^+e^-$ sample. 92

3.14. The electron track momentum distribution, P^e_T, for the $Z^0 \rightarrow e^-e^-$ sample 93
3.15. The distribution of the transverse energy inside a cone of R=0.7 about the electron, excluding the electron energy , for the $Z^0 \rightarrow e^+e^-$ sample. 94
3.16. The distribution of the transverse energy inside a cone of R=0.4 about the electron, excluding the electron energy, for the $Z^0 \rightarrow e^+e^-$ sample 95
3.17. The impact parameter (d_0) for electron tracks from a $W \rightarrow e\nu$ sample selected by requiring $E^e_T > 25$ GeV and $E^{miss}_T > 25$ GeV. . 96
3.18. The track-to-vertex distance along the beamline ($|Z_{track} - Z_{vertex}|$) for tracks from the $W \rightarrow e\nu$ sample. 97
3.19. Test-beam measurement of the CEM energy deposition (E^{tower}_{EM}) for 57 GeV/c muons. From reference [49]. 98
3.20. Test-beam measurement of the CHA energy deposition (E^{tower}_{HAD}) for 57 GeV/c muons. From reference [49]. 99
3.21. Test-beam measurement of $E^{tower}_{EM} + E^{tower}_{HAD}$ for 57 GeV/c π^-'s . The small peak corresponds to minimum ionizing pions and some untagged muons. From reference [48]. 100
3.22. The invariant mass ($M_{\mu^+\mu^-}$) distribution for the dimuon sample. . 101
3.23. The invariant mass ($M_{\mu^+\mu^-}$) distribution for CMUO-CMUO events. 102
3.24. The invariant mass ($M_{\mu^+\mu^-}$) distribution for CMUO-CMIO events. 103
3.25. Plot of η versus ϕ (modulo 15°) for CMUOs from $Z \rightarrow \mu^+\mu-$. The central muon chamber coverage of $|\eta| < 0.6$ is apparent, as well as the gaps between modules at 0° and 15° 104
3.26. Plot of η versus ϕ (modulo 15°) for CMIOs from $Z \rightarrow \mu^+\mu-$ before calorimeter fiducial cuts. The CMIO coverage within $\eta < 1.2$ is complementary to the muon chamber coverage illustrated in the previous figure. 105

3.27. Plot of η versus ϕ (modulo 15°) for CMIOs from $Z \to \mu^+\mu-$ after calorimeter fiducial cuts are applied. 106
3.28. The distribution of E_{EM}^{tower} for CMUOs from $Z \to \mu^+\mu-$. 107
3.29. The distribution of E_{HAD}^{tower} for CMUOs from $Z \to \mu^+\mu-$. 108
3.30. The distribution of $E_{EM}^{tower} - E_{HAD}^{tower}$ for CMUOs from $Z \to \mu^+\mu-$. 109
3.31. The distribution of the azimuthal distance at the muon chamber radius between the extrapolated track and the muon chamber track ($\delta X_{track-stub}$) for CMUOs from $Z \to \mu^+\mu-$. 110
3.32. The distribution of E_{EM}^{tower} for CMIOs from $Z \to \mu^+\mu-$. 111
3.33. The distribution of E_{HAD}^{tower} for CMIOs from $Z \to \mu^+\mu-$. 112
3.34. The distribution of $E_{EM}^{tower} - E_{HAD}^{tower}$ for CMIOs from $Z \to \mu^+\mu-$. . 113
3.35. The distribution of the transverse energy in the towers within a cone of R=0.4 , excluding the muon energy ($E_T^{R<0.4} - E_T^{tower}$) for CMIOs from $Z \to \mu^+\mu-$. 114
4.1. The generated P_T spectra of a) the top quark, and b) the leptons from t-decay , for direct $t\bar{t}$ pair production at $M_{top} = 70$ GeV/c^2. 139
4.2. The generated P_T spectra of a) the top quark, and b) the leptons from t-decay , for direct $t\bar{t}$ pair production at $M_{top} = 28$ GeV/c^2. 140
4.3. The generated P_T spectra of a) the bottom quark, and b) the leptons from b-decay , for direct $b\bar{b}$ production. 141
4.4. a) E_T^e versus P_T^μ , and b) lepton pseudorapidity distribution, for $t\bar{t}$ pairs of $M_{top} = 70$ GeV/c^2. 142
4.5. a) E_T^e versus P_T^μ , and b) lepton pseudorapidity distribution, for $t\bar{t}$ pairs of $M_{top} = 28$ GeV/c^2. 143
4.6. a) E_T^e versus P_T^μ , and b) lepton pseudorapidity distribution, for directly produced $b\bar{b}$ pairs. 144
4.7. The expected number of opposite-sign events for 4.4 pb^{-1} with $E_T^e > P_T^{min}$ and $P_T^\mu > P_T^{min}$ as a function of the threshold P_T^{min} for ISAJET $t\bar{t}$ and $b\bar{b}$ events. 145

4.8. The $t\bar{t} \to e\mu + X$ efficiencies for: i) the P_T cuts , ii) geometric acceptance (after P_T cuts), iii) dilepton reconstruction (after P_T and geometry cuts), and iv) total. 146
4.9. The transverse energy inside a cone of R= 0.4 about the electron, excluding the electron transverse energy, for electrons from top decay for $M_{top} = 28$ GeV/c^2. 147
4.10. The transverse energy inside a cone of R= 0.4 about the electron, excluding the electron transverse energy, for electrons from top decay for $M_{top} = 70$ GeV/c^2. 148
4.11. The transverse energy inside a cone of R= 0.4 about the electron, excluding the electron transverse energy, for electrons from $b\bar{b}$ Monte Carlo. 149
4.12. Inclusive electron spectrum for CDF data with integrated luminosity of 4.4 pb^{-1}. 150
4.13. $K\pi$ invariant mass for track pairs near an electron. The peak corresponds to $D^0 \to K\pi$ decays from $B \to D^0 e\nu$. From reference [76]. 151
4.14. Electron transverse energy vs. muon transverse momentum for CDF data with an integrated luminosity of 4.4 pb^{-1}. Only opposite-sign events are shown in this figure. 152
4.15. Electron transverse energy vs. muon transverse momentum for $t\bar{t}$ Monte Carlo data ($M_{top} = 28$ GeV/c^2) with an integrated luminosity of 3 pb^{-1}. Only opposite-sign events are shown in this figure. 153
4.16. Electron transverse energy vs. muon transverse momentum for $t\bar{t}$ Monte Carlo data ($M_{top} = 70$ GeV/c^2) with an integrated luminosity of 80 pb^{-1}. Only opposite-sign events are shown in this figure. 154
4.17. P_T^{min} =Min(E_T^e, P_T^μ) versus the azimuthal separation between electron and muon for CDF data with an integrated luminosity of 4.4 pb^{-1}. Only opposite-sign events are shown in this figure. 155

4.18. P_T^{min} =Min(E_T^e, P_T^μ) versus the azimuthal separation between electron and muon for $t\bar{t}$ Monte Carlo data (M_{top} = 28 GeV/c^2) with an integrated luminosity of 3 pb^{-1}. Only opposite-sign events are shown in this figure. 156
4.19. P_T^{min} =Min(E_T^e, P_T^μ) versus the azimuthal separation between electron and muon for $t\bar{t}$ Monte Carlo data (M_{top} = 70 GeV/c^2) with an integrated luminosity of 80 pb^{-1}. Only opposite-sign events are shown in this figure. 157
4.20. A CTC display of the top candidate event. 158
4.21. A calorimeter display of the top candidate event. 159
4.22. Electron isolation, $Iso = (E_T^{R<0.7} - E_T^e)/E_T^e$, for CDF data with an integrated luminosity of 4.4 pb^{-1}. Only opposite-sign events are shown in this figure. 160
4.23. Electron isolation, $Iso = (E_T^{R<0.7} - E_T^e)/E_T^e$, for $t\bar{t}$ Monte Carlo data (M_{top} = 28 GeV/c^2) with an integrated luminosity of 3 pb^{-1}. Only opposite-sign events are shown in this figure. 161
4.24. Electron isolation, $Iso = (E_T^{R<0.7} - E_T^e)/E_T^e$, for $t\bar{t}$ Monte Carlo data (M_{top} = 70 GeV/c^2) with an integrated luminosity of 80 pb^{-1}. Only opposite-sign events are shown in this figure. 162
4.25. Missing transverse momentum for CDF data with an integrated luminosity of 4.4 pb^{-1}. Only opposite-sign events are shown in this figure. 163
4.26. Missing transverse momentum for $t\bar{t}$ Monte Carlo data (M_{top} = 28 GeV/c^2) with an integrated luminosity of 3 pb^{-1}. Only opposite-sign events are shown in this figure. 164
4.27. Missing transverse momentum for $t\bar{t}$ Monte Carlo data (M_{top} = 70 GeV/c^2) with an integrated luminosity of 80 pb^{-1}. Only opposite-sign events are shown in this figure. 165

4.28. Electron transverse energy vs. muon transverse momentum for CDF data with an integrated luminosity of 4.4 pb^{-1}. Only same-sign events are shown in this figure. 166
4.29. Min(E_T^e, P_T^μ) versus the azimuthal separation between electron and muon for CDF data with an integrated luminosity of 4.4 pb^{-1}. Only same-sign events are shown in this figure. 167
4.30. E_T^e vs. P_T^μ for CDF low threshold, $e\mu$ data with an integrated luminosity of 1.8 pb^{-1}. a) Opposite-sign data, and b) same-sign data. 168
4.31. E_T^e vs. P_T^μ for $b\bar{b}$ Monte Carlo data with an integrated luminosity of 0.64 pb^{-1}. a) Opposite-sign data, and b) same-sign data. . . . 169
4.32. Electron variables for CDF low threshold opposite-sign $e\mu$ data. a) Transverse momentum (E_T^e), b) Hadronic to electromagnetic energy ratio (HAD/EM), c) Lateral sharing ($Lshr$), and c) Ratio of calorimeter energy to track momentum (E/P). 170
4.33. Electron variables for CDF low threshold opposite-sign $e\mu$ data. a) Strip chamber χ^2_ϕ, b) strip chamber χ^2_z, c) track-strip matching in ϕ ($R\delta\phi$), d) track-strip matching along z (δz). 171
4.34. Electron variables for $b\bar{b}$ Monte Carlo opposite-sign data. a) Transverse momentum (E_T^e), b) Hadronic to electromagnetic energy ratio (HAD/EM), c) Lateral sharing ($Lshr$), and c) Ratio of calorimeter energy to track momentum (E/P). 172
4.35. Electron variables for $b\bar{b}$ Monte Carlo opposite-sign data. a) Strip chamber χ^2_ϕ, b) strip chamber χ^2_z, c) track-strip matching in ϕ ($R\delta\phi$), d) track-strip matching along z (δz). 173
4.36. Muon variables for CDF low threshold opposite-sign $e\mu$ data. a) Transverse momentum P_T^μ, b) E_{EM}^{tower}, c) E_{HAD}^{tower}, d) matching in azimuth $\delta X_{track-stub}$. 174

4.37. Muon variables for $b\bar{b}$ Monte Carlo opposite-sign data. a) Transverse momentum P_T^μ, b) E_{EM}^{tower}, c) E_{HAD}^{tower}, d) matching in azimuth $\delta X_{track-stub}$. 175
4.38. Missing transverse energy for CDF low threshold, opposite-sign $e\mu$ data with an integrated luminosity of 1.8 pb^{-1}. 176
4.39. Missing transverse energy for $b\bar{b}$ Monte Carlo opposite-sign data with an integrated luminosity of 0.64 pb^{-1}. 177
4.40. Electron isolation, $Iso = (E_T^{R<0.7} - E_T^e)/E_T^e$, for CDF low threshold, opposite-sign $e\mu$ data with an integrated luminosity of 1.8 pb^{-1}. 178
4.41. Electron isolation, $Iso = (E_T^{R<0.7} - E_T^e)/E_T^e$, for $b\bar{b}$ Monte Carlo opposite-sign data with an integrated luminosity of 0.64 pb^{-1}. . . 179
4.42. $\Delta\phi_{e\mu}$ for a) opposite-sign and b) same-sign, for the generated events. The dashed line is for direct $c\bar{c}$; the dotted line for direct $b\bar{b} + c\bar{c}$; and the solid line is the total, including gluon splitting and flavor excitation. 180
4.43. $\Delta\phi_{e\mu}$ for a) opposite-sign and b) same-sign, after reconstruction. The dotted line is for direct $b\bar{b} + c\bar{c}$; and the solid line is the total, including gluon splitting and flavor excitation. 181
4.44. $\Delta\phi_{e\mu}$ for a) opposite-sign and b) same-sign, for CDF low-threshold data. The curves are normalized to $N_{opp} + N_{same}$. 182
4.45. CDF jet fragmentation function, from reference [78]. 183
4.46. The distributions of a)E_T^e vs. P_T^μ, and b) $\Delta\phi_{e\mu}$, for $Z^0 \to \tau\tau \to e\mu + X$ events generated with $P_T^{min} > 15$ GeV/c. 184
4.47. A CTC display of a the $Z^0 \to \tau\tau \to e\mu + X$ candidate event. . . . 185
4.48. A calorimeter display of the $Z^0 \to \tau\tau \to e\mu + X$ candidate event. 186
4.49. The distributions of a)E_T^e vs. P_T^μ, and b) $\Delta\phi_{e\mu}$, for $WW \to e\mu + X$ events generated with $P_T^{min} > 15$ GeV/c. 187

5.1. The 95% CL upper limit on the $t\bar{t}$ production cross section as a function of top quark mass. The shaded band shows the result of a theoretical calculation of the $t\bar{t}$ production cross section [26,28]. 196
5.2. The spectrum for leptons from fourth generation, charge $-\frac{1}{3}$, b' quarks with charged current decays, compared to the spectrum of leptons from top decay. From reference [82]. 197

Chapter 1

INTRODUCTION

In the Standard Model (SM) the constituents of all matter are arranged in three generations of quarks and leptons (Table 1.1). A fourth generation is in principle also possible. Recent experiments at e^+e^- colliders have ruled out the possibility of a fourth light neutrino, implying that a fourth generation is only allowed if its neutrino has a mass in excess of ~ 30 GeV/c^2 [1]. Experimental evidence from measurements of the forward-backward asymmetry in $e^+e^- \rightarrow b\bar{b}$ and from the absence of flavor-changing neutral-currents in bottom quark (b) decays, implies the existence of an isodoublet partner of the b quark to complete the third family. The postulated sixth quark (t, or top) has not yet been observed. Searches for the top quark at e^+e^- and $p\bar{p}$ experiments have placed lower limits on its mass. Phenomenology provides lower limits on M_{top} obtained from fits to SM parameters to account for the observed degree of $B^0\bar{B}^0$ mixing, and upper limits by requiring consistency of SM parameters with the measured W and Z boson masses, and with weak neutral-current data. Some of this evidence will be briefly reviewed further in this chapter.

In the period from June 1988 to May 1989 the Collider Detector at Fermilab (CDF) collected approximately 6 million events produced at the Tevatron proton-antiproton collider at a center of mass energy of $\sqrt{s} = 1.8$ TeV. This is the largest center of mass energy attainable in the world today, and the luminosity of the data collected represents an increase by a factor of 100 over the data collected by CDF during the previous 1987 run. With this data-sample, we have obtained a sensitivity to top quarks with masses in the vicinity of the mass of the W boson. This thesis describes a search for the top quark performed with the CDF detector. The process investigated is the direct production of quark-antiquark pairs, and

the signature employed is the presence of both an electron and a muon with high transverse momenta (P_T) and with opposite electric charges.

The thesis is organized as follows : the remainder of Chapter 1 contains a summary of phenomenological constraints and of the main experimental results from top quark searches. The QCD predictions for heavy quark production in hadron collisions are briefly reviewed, and the signatures for the top quark at the Tevatron are discussed to motivate the methods of our top quark search.

Chapter 2 describes the components of the CDF detector that are relevant for the analysis. A brief description of the accelerator is also given.

Chapter 3 describes the on-line triggers capable of detecting electron-muon events. the variables utilized off-line for the identification of electrons and muons. and studies of the selection criteria on electrons and muons using leptons from Z^0 decays. Also, two data processing streams are introduced in this chapter. First, an expressline or 'Spin' output stream selected leptons with high enough transverse energy to ensure a small number of events to process (during the course of the run, Spin was only about two weeks behind data taking) but low enough to capture an important fraction of the top events which decay into leptons. The Spin sample has the major advantage of having the full luminosity of the CDF 1988-1989 run. Second, a standard 'Production' output stream with reduced lepton thresholds allows a study of the backgrounds. When the analysis of this thesis was performed, the Production output stream had processed roughly half the full luminosity of the Spin, but the low lepton thresholds allowed the collection of a high statistics $e\mu$ sample for comparison with expectations from bottom quark production.

In Chapter 4 the top quark signal region is defined and motivated. The detection efficiency for $t\bar{t} \rightarrow e\mu + X$ in this signal region is derived as a function of top quark mass and decomposed into separate geometric acceptance, transverse momentum acceptance and reconstruction efficiency terms. The Spin $e\mu$ data is shown and compared to Monte Carlo expectations for various top masses. One candidate is found in the data in the signal region, whereas 33 events and 7.5

events are expected in this region from $t\bar{t} \to e\mu + X$ at $M_{top} = 28$ GeV/c^2 and 70 GeV/c^2, respectively. We also show results from the Production $e\mu$ data and compare it to Monte Carlo expectations for $b\bar{b} \to e\mu + X$. We find fair agreement between these data and the Monte Carlo predictions for the rates and for the shapes of distributions of several kinematic variables, including the azimuthal angular separation between the two leptons, missing tranverse energy and lepton isolation.

Given that we observe only one event in the signal region, and that the bulk of the $e\mu$ data is consistent with $b\bar{b}$ production, in Chapter 5 we derive an upper limit on the $t\bar{t}$ cross section as a function of top quark mass M_{top}. Systematic uncertainties are discussed, and the 95% CL upper limit on the expected number of events in the signal region is obtained as a function of M_{top}. This number is used along with the Monte Carlo calculation of the $t\bar{t}$ detection efficiency as a function of M_{top}, the integrated luminosity, and the semileptonic branching ratio to provide the upper limit on the $t\bar{t}$ production cross section, which is converted into a lower limit on M_{top} by using the predicted $t\bar{t}$ cross sections.

Chapter 6 contains the summary and conclusions of the analysis. The possibility of extending the sensitivity for detecting top quarks using the 1988-1989 CDF data is considered. The top quark discovery potential for future collider runs with expected recorded integrated luminosities of 20 pb^{-1} (1991) and 100 pb^{-1} (1993) is discussed.

1.1 STATUS OF SEARCHES FOR THE TOP QUARK

When the analysis of this thesis was carried out, the experimental lower bounds on the mass of the top were $M_{top} > 28$ GeV/c^2 from the absence of $t\bar{t}$ production at the TRISTAN e^+e^- collider [2], and $M_{top} > 41$ GeV/c^2 at the 95% confidence level (CL) from searches at the CERN $p\bar{p}$ collider [3].

Since then, results from the TEVATRON $p\bar{p}$ collider from two independent channels become available. The CDF e+jets analysis excluding top quarks with

mass in the range 40 – 77 GeV/c^2 and the CDF $e\mu$ analysis (this thesis) excluding the range 28 – 72 GeV/c^2 have both been published [5,6]. The e+jets analysis searches for $p\bar{p} \to t\bar{t} \to e\nu X$ in events containing an electron, two or more hadronic jets, and missing transverse energy (E_T^{miss}). The transverse mass variable $M_T^{e\nu} = \sqrt{2E_T^e E_T^{miss}(1 - \cos\Delta\phi_{e\nu})}$, with E_T^e the electron transverse energy and $\Delta\phi_{e\nu}$ the azimuthal separation between the electron and missing transverse energy vectors, is used to distinguish the top signal from the dominant W+jets background. Extended analyses (which will be discussed in Chapter 6) are underway at CDF.

Recently, e^+e^- colliders with center-of-mass energies around the Z^0 mass at SLAC and LEP have become available, and lower bounds of $M_{top} > 44.8$ GeV/c^2 [4] have been reported. Also, a new 95% CL limit of $M_{top} > 69$ GeV/c^2 from a recent higher luminosity run at the CERN $p\bar{p}$ collider has been reported [7] by the UA2 collaboration. The LEP result is based on a search for $Z^0 \to t\bar{t}$, where the signature used is the presence of an isolated charged particle from semileptonic t-decay. The UA2 result is based on a search for $p\bar{p} \to W \to t\bar{b}$ and $p\bar{p} \to t\bar{t}$ in events with an electron, one or more hadronic jets, and missing transverse energy. As in the CDF e+jets analysis, the transverse mass variable is used to distinguish signal from backgrounds.

1.2 PHENOMENOLOGICAL CONSTRAINTS

Forward Backward Asymmetry in $e^+e^- \to b\bar{b}$

The forward-backward asymmetry (A_{FB}) in the process $e^+e^- \to$ quark-antiquark, is defined in terms of the number of quarks produced in the electron (forward) direction N_b^F and the number produced in the positron (backward) direction N_b^B, namely, $A_{FB} = (N_b^F - N_b^B)/(N_b^F + N_b^B)$. The process $e^+e^- \to b\bar{b}$ can proceed through photon annihilation or through Z^0 annihilation, as is shown in figure 1.1. The couplings to the b are also shown in the figure. The asymmetry arises from the interference between the axial-vector coupling of the b-quark to the Z^0 (a_b) and the vector coupling to both γ (Q_b) and Z^0 (v_b), and is proportional

to a_b. The JADE collaboration [8] has made the most accurate measurement of the b-jet asymmetry, which was carried out at an e^+e^- center-of-mass energy of 34.6 GeV. The measured value of $A = (-22.8 \pm 6.0 \pm 2.5)\%$ implies an axial-vector coupling for the bottom quark (assuming $Q_b = -\frac{1}{3}$ for its charge) of $a_b = -0.90 \pm 0.24 \pm 0.10$. A correction factor [9] that takes into account $B^0\bar{B}^0$ mixing (using the measurement from the ARGUS collaboration [10]), brings the JADE measurement to $a_b = -1.15 \pm 0.31 \pm 0.18$. This is in good agreement with the Standard Model expectation of $a_b = -1$ (for a weak isospin of $-\frac{1}{2}$) which implies that the bottom quark is a member of an SU(2) doublet and hence that the top quark exists.

Absence of FCNC decays of the b-quark.

At the time when only u, d, s quarks were known, Glashow, Iliopoulos and Maiani pointed out that the existence of a charm quark (in a same doublet with the s quark) would explain the experimentally observed extreme suppression of flavor-changing neutral-current (FCNC) $s \to d$ transitions. The cancellation of such flavor-changing transitions occurs in general if all left-handed quark states appear in doublets and is known as the GIM mechanism (after the authors). In the same way, models with a b but no t should have FCNCs visible in b decays. Kane and Peskin have shown [11] that in models in which the b quark is a weak SU(2) singlet, the neutral current decays in semileptonic b decays should occur at a rate such that $\Gamma(B \to l^+l^-X)/\Gamma(B \to l^+\nu X) \geq 0.12$, which gives a branching ratio of at least 1.3×10^{-3} for $b \to l^+l^-X$. Figure 1.2 shows charged-current and neutral-current diagrams contributing to semileptonic b decay. The CLEO collaboration has searched for $\mu^+\mu^-X$ and e^-e^-X final states in a sample of $\Upsilon(4S)$ decays [12]. Expected sources of dileptons are semileptonic decays of both the B and the $\bar{B}$ from $\Upsilon(4S) \to B\bar{B}$, cascade decays, $B \to wX \to l^+l^-X$, semileptonic decays of the D and the $\bar{D}$ from $c\bar{c}$ production in the continuum under the $\Upsilon(4S)$, and misidentified hadrons. The rates of all these sources can be reliably calculated, and any excess of opposite-sign dileptons beyond the expected rate is attributed

to FCNCs. The analysis sets a 90 % CL limit of $\frac{1}{2}[B(b \to \mu^-\mu^-X) - B(b \to e^-e^-X)] < 3.1 \times 10^{-3}$, well below the Kane-Peskin limit, and rules out models lacking a top quark.

$B^0\bar{B}^0$ mixing.

$B^0\bar{B}^0$ mixing was first observed in $p\bar{p}$ collisions by the UA1 collaboration [13]. It has also been observed in e^-e^- collisions by the ARGUS [10] and CLEO [14] collaborations.

Through mixing, a B^0 meson can transform into its anti-particle, the $\bar{B}^0$, before decaying. The second quark in the neutral B meson can be a d-quark ($B^0_d = \bar{b}d$) or an s-quark ($B^0_s = \bar{b}s$). $B^0_d\bar{B}^0_d$ and $B^0_s\bar{B}^0_s$ mixing proceed through 'box diagrams' illustrated in figure 1.3. $B^0\bar{B}^0$ pairs can be produced in e^-e^- and $p\bar{p}$ experiments, and the signature for mixing is an excess of same-sign dileptons from the semileptonic decays of both B mesons of a B^0B^0 or $\bar{B}^0\bar{B}^0$ final state. The ARGUS and CLEO measurements were based on a studies of $B^0_d\bar{B}^0_d$ pairs produced in $\Upsilon(4S)$ decays. At the $\Upsilon(4S)$, $B^0_s\bar{B}^0_s$ pair production is kinematically forbidden. The ratio $r = [N(B^0B^0) + N(\bar{B}^0\bar{B}^0)]/N(B^0\bar{B}^0)$, was measured by ARGUS to be $r_d = 0.21 \pm 0.08$.

In a three-generation standard model, mixing is described by a parameter x which is related to experiment by $r = x^2/(x^2+2)$. The parameter x_d has an explicit M^2_{top} dependance [15] which has been used together with the ARGUS measurement to set a lower limit of $M_{top} \gtrsim 50$ GeV/c^2 [10,16,17].

Radiative Corrections.

The standard model predictions for the Z and W mass and their interdepence, confronted with the measurements of M_W and M_Z and with weak-neutral-current data, have implications on the top quark mass which have been discussed by various authors, including [18,19,20,21].

The standard model prediction for the W and Z masses is [18]:

$$M_W^2 = \frac{A^2}{(1-\Delta r)\sin^2\theta_W} \; . \tag{1.1}$$

where the weak mixing angle θ_W is defined by

$$\sin^2\theta_W \equiv 1 - (\frac{M_W}{M_Z})^2 \; . \tag{1.2}$$

The constant $A = \sqrt{\pi\alpha/\sqrt{2}G_\mu}$ depends on the precisely determined fine-structure constant α and muon decay constant G_μ and has the value $A = 37.2805 \pm 0.0003$ GeV/c^2. Δr denotes the effect of one-loop radiative corrections [19] of the kind illustrated in figure 1.4. Δr is a function of the top quark mass and the Higgs mass M_H, and as is shown in figure 1.5 the strongest dependance is on M_{top}. It also depends on the mass of other fermions such as the charm and bottom quarks, but these are constrained from low energy phenomenology.

Some of the most important constraints on M_{top} are summarized in figure 1.6 [21]. Since the M_H dependance of the radiative corrections is small, $M_H = 100$ GeV/c^2 was chosen for simplicity. The $\pm 1\sigma$ uncertainty bands on $\sin^2\theta_W$ are indicated as a function of M_{top} for several determinations:

- M_Z

  By combining eqs. 1.1 and 1.2, $\sin^2\theta_W$ can be determined as a function of Δr and M_Z (with no M_W dependance). The measured value of M_Z can then be used to give the dashed lines in figure 1.6.

- M_W/M_Z

  The definition of $\sin^2\theta_W$ of equation 1.2 can be used together with the measured value of M_W/M_Z to derive the dotted lines in figure 1.6.

- νN

  Data from deep-inelastic neutrino-nucleon scattering (νN) [22,23] has lead to determinations of of $\sin^2\theta_W$ shown with dash-dotted lines in figure 1.6.

As seen in figure 1.6, the combination of M_Z with νN neutral-current data gives an upper limit of ~ 200 GeV/c^2 on M_{top}, and the combination of M_Z with the M_W/M_Z determination yields an upper limit of ~ 250 GeV/c^2. When all data are combined in a global fit, an upper limit on M_{top} of ~ 210 GeV/c^2 is obtained [21]. The SLAC measurement of $M_Z = 91.17 \pm 0.18$ GeV/c^2 [24] and the CDF measurement of $M_W = 80.0 \pm 0.2 \pm 0.5(\pm 0.3)$ [25] were used as input. Today, more precise measurements of M_W and M_Z are available, but the upper limit on M_{top} is not changed importantly.

1.3 HADRONIC PRODUCTION OF HEAVY QUARKS

In the Quantum Chromodynamics (QCD) parton model, the scattering cross section of two hadrons into a pair of heavy quarks ($A + B \to Q + \bar{Q} + X$) is given by:

$$\sigma(s) = \sum_{ij}\int dx_1 dx_2 \hat{\sigma}_{ij}(x_1 x_2 s, m^2, \mu^2) F_i^A(x_1,\mu) F_j^B(x_2,\mu) \; , \tag{1.3}$$

where the structure functions F_i^A are the probabilities of finding a parton i in hadron A with momentum fraction between x_1 and $x_1 - dx_1$, m is the heavy quark mass, and $\sqrt{s}$ is center of mass energy of the $A - B$ system. μ is an arbitrary scale related to the energy scale of the interaction. The partonic cross sections $\hat{\sigma}_{ij}$, for the process $ij \to Q\bar{Q}X$ are calculable as an expansion of the strong coupling α_S [26]. In the lowest order (α_S^2), the processes contributing are those of gluon-gluon fusion and quark-antiquark annihilation:

$$\begin{aligned} g + g &\to Q + \bar{Q} \\ q + \bar{q} &\to Q + \bar{Q} \end{aligned} \tag{1.4}$$

The Feynman diagrams for these processes are shown in figure 1.7. Two important kinematic consequences of the leading order processes are , (1) the quark and antiquark are produced back-to-back in the parton-parton center of mass frame, and remain back-to-back in the plane transverse to the colliding beams; and (2) the heavy quarks are emitted with an average transverse momentum of about the quark mass m_Q.

The idea that higher order processes could have an important role in heavy quark production is suggested by considering the fragmentation (or splitting) of a final state gluon from $gg \to gg$, into a pair of heavy quarks. The splitting $g \to Q\bar{Q}$ occurs only a small fraction, of order $\sim \alpha_S(m^2)$, of the time. However, given the large cross section of $gg \to gg$, it can be a competitive quark production process. This process ($gg \to gQ\bar{Q}$) and other $2 \to 3$ processes of order α_S^3, as well as the α_S^3 part of the $2 \to 2$ processes of 1.4 have been calculated by Nason, Dawson and Ellis [26]. The following parton subprocesses were included in the calculation up to order α_S^3 :

$$
\begin{array}{ll}
q + \bar{q} \to Q + \bar{Q} & \alpha_S^2, \alpha_S^3 \\
g + g \to Q + \bar{Q} & \alpha_S^2, \alpha_S^3 \\
q + \bar{q} \to Q + \bar{Q} + g & \alpha_S^3 \\
g + g \to Q + \bar{Q} + g & \alpha_S^3 \\
g + q \to Q + \bar{Q} + q & \alpha_S^3 \\
g + \bar{q} \to Q + \bar{Q} + \bar{q} & \alpha_S^3
\end{array}
\tag{1.5}
$$

The theoretical heavy flavor cross sections are dependant on the different input quantities : parton structure functions, choice of renormalization and factorization scale μ, the choice of running coupling α_S (or equivalently, the choice of the QCD parameter Λ, since α_S is a function of μ/Λ), and the mass of the heavy quark. Figure 1.9 [27] shows the μ-dependance of the $t\bar{t}X$ cross section for the leading order and next-to leading order calculation. The sensitivity to the scale μ is reduced with the inclusion of the $O(\alpha_S^3)$ corrections, making the theoretical prediction more reliable. Altarelli *et al.* [28] have studied the total cross sections for top, bottom, and charm production using the results of Nason *et al.* [26], together with a recent set of structure functions, DFLM [29], also obtained with next-to-leading accuracy. Their results for $p\bar{p} \to t\bar{t}X$ at $\sqrt{s} = 1.8$ TeV are listed in Table 1.2. They quote a 'central value' cross section evaluated at $\mu = m$ and $\Lambda_5 = 170$ MeV (5 active flavors), and an 'indicative error', typically within $\sim 30\%$, derived by varying μ and Λ_5 in the ranges $\frac{1}{2}m \leq \mu \leq 2m$ and 90 MeV $\leq \Lambda_5 \leq 250$

MeV. Figure 1.10 shows these cross sections for $p\bar{p}$ collisions at $\sqrt{s} = 1.8$ TeV and $\sqrt{s} = 0.63$ TeV.

In the case of the bottom quark, the theoretical prediction for the cross section has large uncertainties. The scale dependance of the $b\bar{b}$ cross section is shown in figure 1.11 for the leading order and next-to leading order calculations. In contrast to the case of the top quark, the inclusion of the higher order corrections subtantially increases the cross section, and also increases the sensitivity to the scale μ. The smaller mass of the bottom quark causes the coupling constant to be larger and the higher order contributions become more important.

1.4 FRAGMENTATION AND DECAY OF HEAVY QUARKS

After a heavy quark is produced, it 'fragments' or 'hadronizes' into a hadron containing its flavor, and some softer, light-flavored hadrons. An example of the fragmentation of a top quark is shown in figure 1.12.

The fragmentation function D_Q^H of a heavy quark Q into a Q-flavored hadron H describes the probability that the hadron carries away a fraction of the quark's momentum between $z = P_H/P_Q$ and $z + dz$. A softer fragmentation (i.e. the hadron carries away less of the quark's momentum) will result in more accompanying hadrons with higher energies. Heavy quark fragmentation is modeled with the Peterson parametrization [30]:

$$D_Q^H = \frac{N}{z[1 - (1/z) - \epsilon_Q/(1-z)]^2} \tag{1.6}$$

where N is a normalization constant and the Peterson parameter ϵ is proportional to $1/M_Q^2$. The Peterson parametrization adequately describes existing c and b quark fragmentation data, as is seen in figure 1.13, and is increasingly harder for $Q = c, b, t$; as is shown in figure 1.14 [31].

In the spectator approximation, the heavy quark contained in the hadron is assumed to decay independently of the other constituents, since the energy released by the quark is much bigger than the typical quark binding energies.

If the top is sufficiently heavy ($\gtrsim$ 150 GeV/c^2) it will not form a hadron

before decaying, since it will have a width $\Gamma \gtrsim 1$ GeV (or equivalently, a lifetime $\lesssim 10^{-24}$s), and will decay very fast (in comparison to typical hadronic scales). The width Γ of the top decay is shown in figure 1.15 as a function of the top mass [32].

The top quark decays into a W^- boson (charged current decay) and a bottom quark. This decay, $t \to Wb$, is illustrated in figure 1.16. The W , which can be real or virtual depending on whether or not $M_{top} > M_W - M_{bottom}$, will then decay into leptons ($e\nu$, $\mu\nu$, or $\tau\nu$) or into a pair of quarks ($u\bar{d}$ or $c\bar{s}$).

The decays into leptons are of great interest. The top semileptonic branching ratio is given in a simple aproximation by counting modes of W^- decay. Assuming equal probabilities for the decay of the W into $e\bar{\nu}_e$, $\mu\bar{\nu}_\mu$, $\tau\bar{\nu}_\tau$, and to each of the three colors of $u\bar{d}$ and $c\bar{s}$, the semileptonic branching ratio for a given lepton species is:

$$Br(W \to l\bar{\nu}_l) \cong \frac{1}{9} \tag{1.7}$$

The semileptonic decay spectra of heavy quarks, $Q \to ql\bar{\nu}_l$ can be treated in a similar fashion as the muon decay $\mu^- \to \nu_\mu e^- \bar{\nu}_e$. Figure 1.17 shows the fractional energy spectra ($x_i = 2E_i/m_Q$) for $b \to ce\nu$ and $c \to se\nu$. Note that the electron is more energetic than the neutrino in b-decay, and the inverse is true for c-decay; this is a consequence of helicity conservation [31]. A calculation of the charged-lepton and b-quark spectra from semileptonic t-decays, including the W width Γ_W, is shown in figures 1.18 and 1.19 [33]. In the region of M_{top} near and above the M_W, the inclusion of a non-zero W width becomes important to obtain realistic spectra.

An important characteristic of top semileptonic decays is the lepton isolation. The products of a top decay will have a large invariant mass, and therefore will be distributed over a larger solid angle than a lighter quark of the same energy. This means that the top-decay lepton will be well separated from the acompanying bottom jet and there will be only moderate amounts of extra energy in the immediate neighborhood of the lepton. Being isolated, leptons from top decay are easy to detect and to distinguish from leptons from the decay of lighter bottom

and charm quarks, where the decay products are much more collimated, giving non-isolated leptons.

1.5 SIGNATURES FOR THE TOP QUARK AT THE TEVATRON

There are two ways of producing top quarks at a $p\bar{p}$ collider:

- $p\bar{p} \to t\bar{t}$
- $p\bar{p} \to W \to t\bar{b}$.

The production cross sections for these two processes are shown in figure 1.10 as a function of M_{top}. The second process is kinematically allowed only if $M_{top} < M_W - M_{bottom}$. At the Tevatron, hadronic pair production of top quarks ($t\bar{t}$) dominates over the decay $W \to t\bar{b}$ except in the neighborhood of $M_t = 60$ GeV/c^2 where they are comparable. On the contrary, at the CERN collider the main contributing process is $W \to t\bar{b}$.

Assuming a semileptonic branching ratio of $\frac{1}{9}$ per lepton, both top quarks decay entirely hadronically 44% of the time. However, the resulting multijet signature is extremely difficult to distinguish from QCD multijet backgrounds which have very large production cross sections [34]. A tremendous enhancement in the signal to noise ratio is obtained by requiring at least one electron or muon in the final state. Figure 1.20 shows a list of final states and their branching ratios.

The case in which one top quark decays semileptonically and the other hadronically accounts for 15 % of the $t\bar{t}$ rate for a given lepton species. This signature, lepton + jets, has a favorable rate. However, it has a significant background from the leptonic decay of W bosons produced in association with jets.

By considering the dilepton final states ($e\mu$, ee, $\mu\mu$) at the cost of more moderate branching fractions (2.5%, 1.2%, 1.2%), the previously mentioned backgrounds cease to be a problem. The ee and $\mu\mu$ channels, besides having lower rate than the $e\mu$ channel, have significant lepton pair backgrounds from Drell-Yan and Z^0 decays. We have therefore chosen to explore the $e\mu$ channel.

The requirement of both an electron and a muon at high transverse momenta with opposite electric charge provides a very clean $t\bar{t}$ signature. The major physics background for the top $e\mu$ channel comes from $b\bar{b}$ production and from $Z^0 \rightarrow \tau\tau$ giving an electron and a muon in the final state. These backgrounds have low rate and distinct topologies and are discussed in Chapter 4. The double semileptonic decay of the $t\bar{t}$ pair (one top quark to $e\nu b$ and the other to $\mu\nu b$, with the assumed branching ratio of $\frac{2}{81}$) contributes over 80 % of the signal. The rest of the signal comes from sequential decays of a daughter b or c quark or τ lepton and is also considered. We do not further consider the process $W \rightarrow t\bar{b}$ process since, as mentioned earlier, it has lower cross section than $t\bar{t}$, and furthermore, the (soft) lepton from the $\bar{b}$ decay is of the same sign as the lepton from the t decay, and thus we are only neglecting the minute contribution of opposite-sign lepton pairs from sequential decays.

In extensions of the SM, the decay of the top into charged Higgs bosons, $t \rightarrow Hb$, could have an important rate if $M_H < M_{top}$ [31]. The preferred decay of the charged Higgs in most models is $H \rightarrow \tau\nu$ or $c\bar{s}$. The case $t \rightarrow \tau\nu b$ could be recognized by its τ-missing E_T signature. Leptonic decays of two τs in a $t\bar{t}$ event could give $e\mu$ final states, but most leptons would have small transverse momenta and would be difficult to separate from backgrounds. We do not further consider this non-standard decay mode.

	Quarks				Leptons			
		Name	Charge	Mass [MeV/c^2]		Name	Charge	Mass [MeV/c^2]
1st Generation	u	up	$+\frac{2}{3}$	350	e	electron	-1	0.511
	d	down	$-\frac{1}{3}$	350	ν_e	e-neutrino	0	$< 5 \times 10^{-6}$
2nd Generation	c	charm	$+\frac{2}{3}$	1800	μ	muon	-1	105.7
	s	strange	$-\frac{1}{3}$	550	ν_μ	μ-neutrino	0	< 0.50
3rd Generation	t	top ?	$+\frac{2}{3}$	?	τ	tau	-1	1784
	b	bottom	$-\frac{1}{3}$	4500	ν_τ	τ-neutrino ?	0	< 164

Table 1.1: The three generations of quarks and leptons. The top quark and the tau-neutrino have not been observed. Quark masses are indicative only. Other masses were taken from reference [35].

Mass [GeV/c^2]	σ [nb]
20	228^{+55}_{-60}
40	$9.63^{+1.7}_{-2.5}$
60	$1.27^{+0.19}_{-0.35}$
80	$0.285^{+0.037}_{-0.077}$
100	$(0.873^{+0.109}_{-0.230}) \times 10^{-1}$
120	$(0.331^{+0.034}_{-0.086}) \times 10^{-1}$
140	$(0.144^{+0.013}_{-0.037}) \times 10^{-1}$
160	$(0.691^{+0.047}_{-0.173}) \times 10^{-2}$
180	$(0.352^{-0.019}_{-0.086}) \times 10^{-2}$
200	$(0.187^{+0.008}_{-0.045}) \times 10^{-2}$

Table 1.2: Heavy quark production cross section in $p\bar{p}$ collisions at 1.8 TeV. From reference [28].

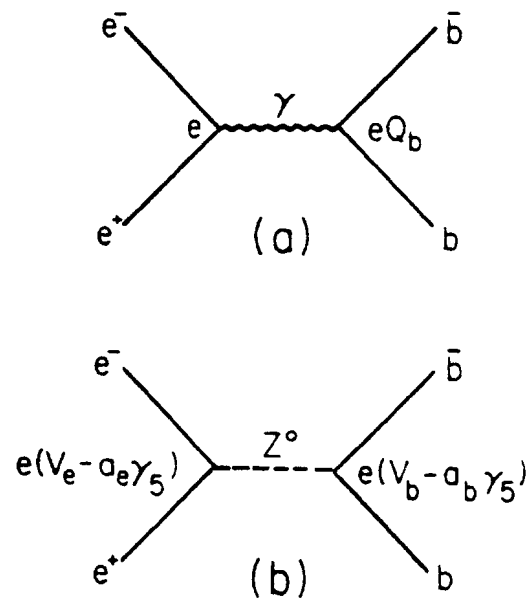

Figure 1.1: Feynman diagrams for the process $e^+e^- \to b\bar{b}$.

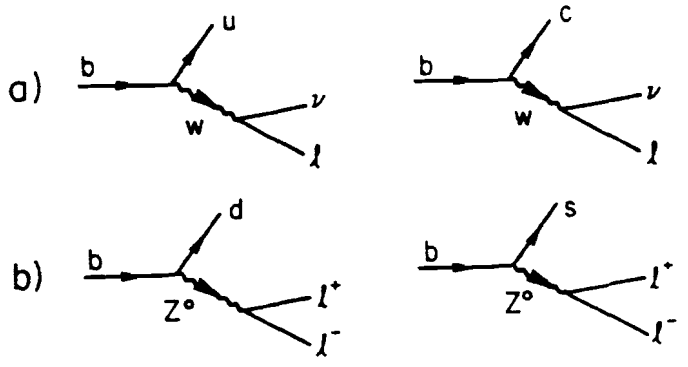

Figure 1.2: Contributions to semileptonic b decay from a)charged current decay and b) neutral current decay.

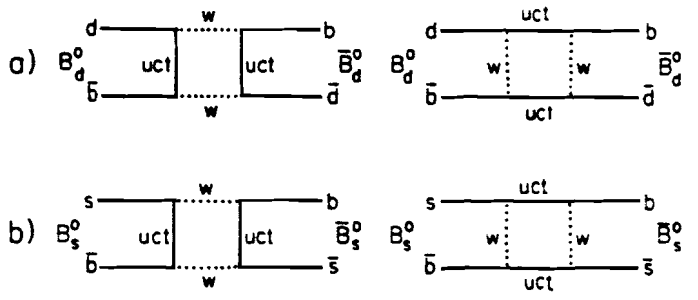

Figure 1.3: Box diagrams for a) $B_d^0\bar{B}_d^0$ and b) $B_s^0\bar{B}_s^0$ mixing.

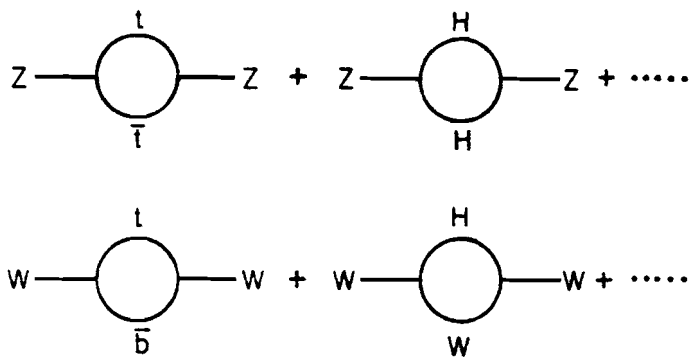

Figure 1.4: Diagrams for one-loop radiative corrections.

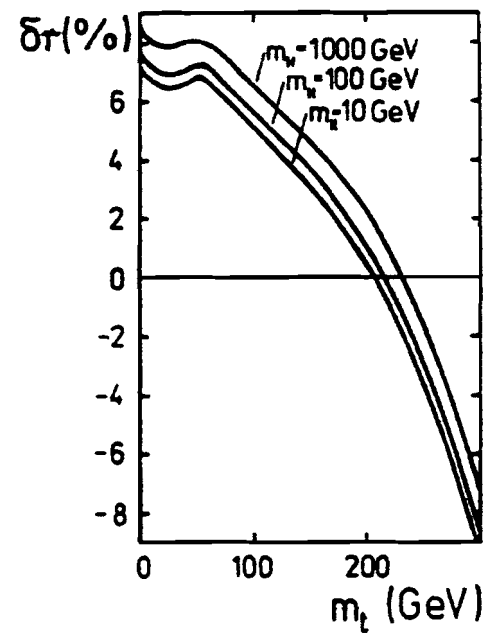

Figure 1.5: The electroweak correction factor Δr as a function of M_{top}. From reference [19].

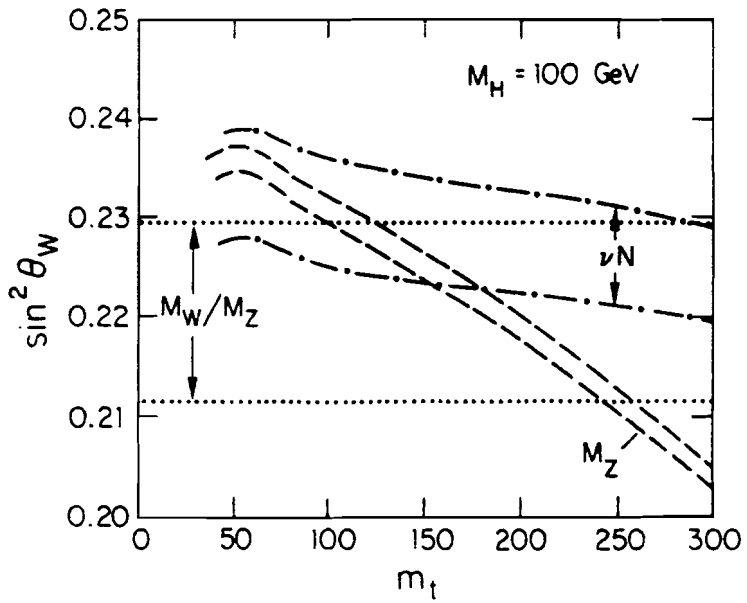

Figure 1.6: The $\pm 1\sigma$ uncertainties in $\sin^2\theta_W$ by various determinations. See the text for an explanation. From reference [21].

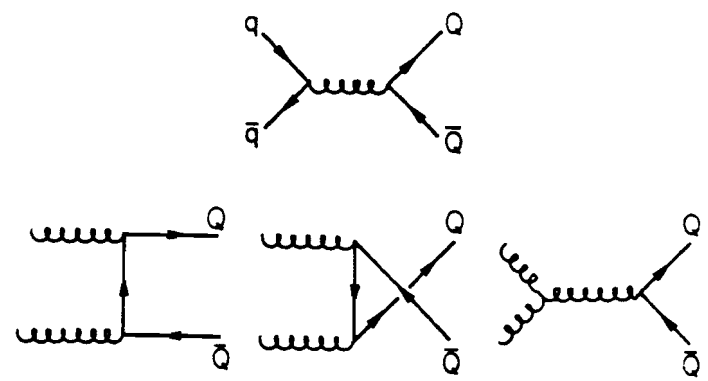

Figure 1.7: Lowest order Feynman diagrams for heavy quark production.

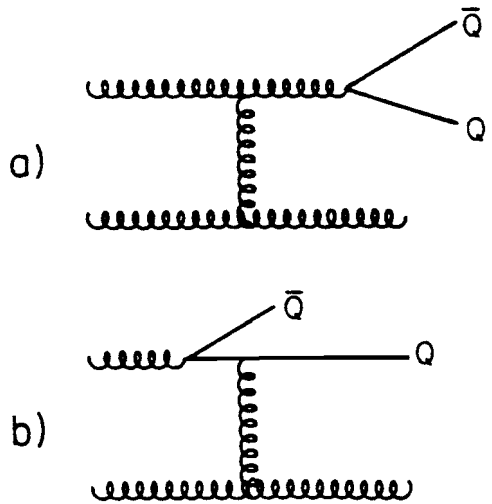

Figure 1.8: Feynman diagrams for a) gluon splitting and b) flavor excitation.

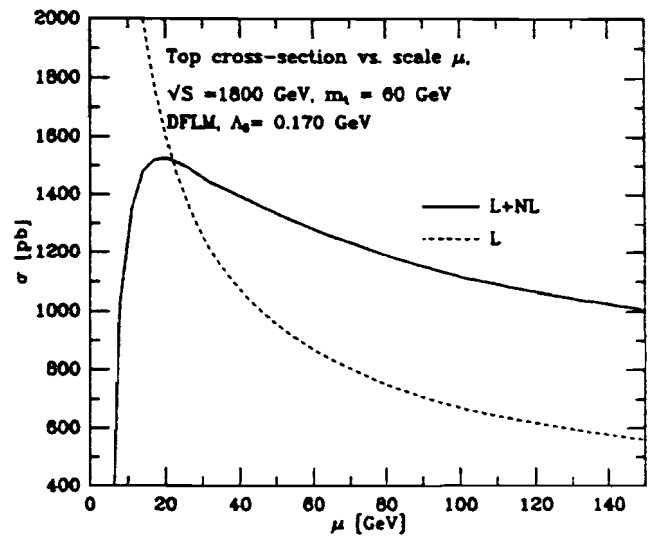

Figure 1.9: The top quark cross section vs. μ at 1.8 TeV. From reference [27].

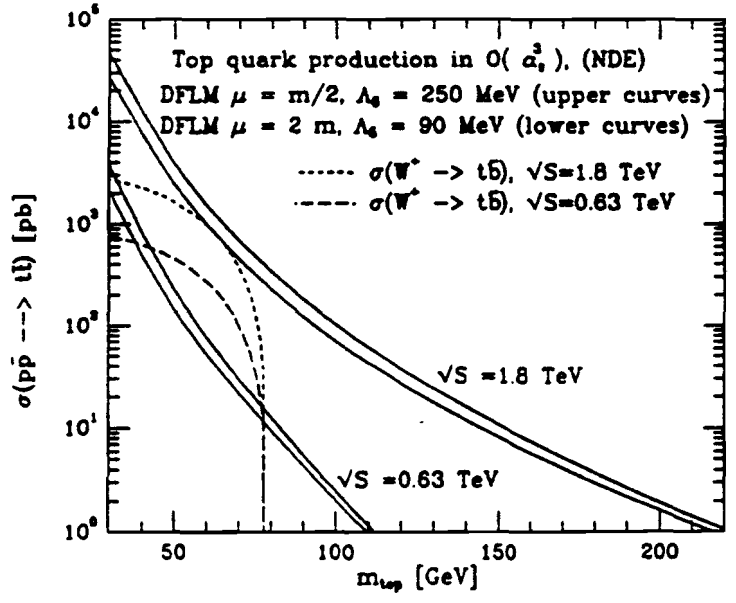

Figure 1.10: The $t\bar{t}$ predicted cross section by Altarelli et. al [28], based on the next-to-leading order calculation by Nason, Dawson, and Ellis [26].

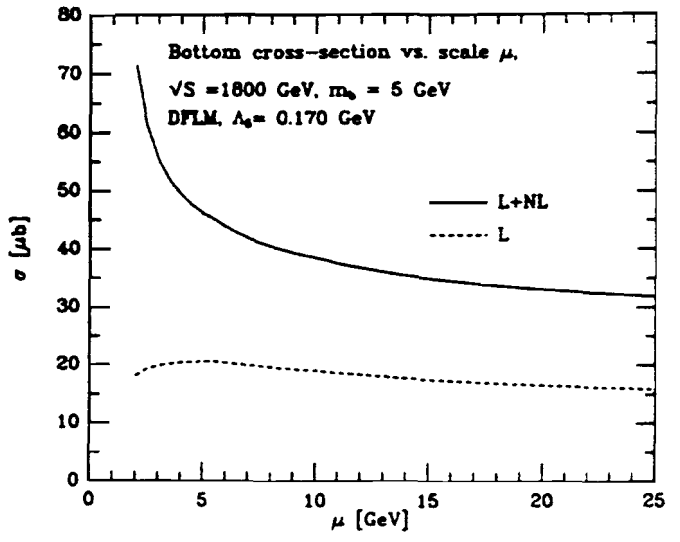

Figure 1.11: The bottom quark cross section vs. μ at 1.8 TeV. From reference [27].

```
                                          Pt    ETA
TOP                                      11.8  -1.83
 -> Td++                                  8.7  -2.16
 .   -> Td+                               8.7  -2.15
 .   .   -> Numu                         22.5  -0.64
 .   .   -> Mu+                          36.9  -0.57
 .   .   -> bottom                        8.2   0.06
 .   .   .   -> Bd*0                     7.4   0.07
 .   .   .   .   -> Bd0                  7.3   0.07
 .   .   .   .   .   -> D+               5.4   0.31
 .   .   .   .   .   .   -> E+           2.7   0.19
 .   .   .   .   .   .   -> Nue          0.5   0.75
 .   .   .   .   .   .   -> KObar        2.4   0.31
 .   .   .   .   .   .   .   -> KOL      2.4   0.31
 .   .   .   .   .   -> Pi-              1.6  -0.10
 .   .   .   .   .   -> PiO              0.9  -1.02
 .   .   .   .   .   .   -> gamma        0.7  -0.94
 .   .   .   .   .   .   -> gamma        0.2  -1.34
 .   .   .   .   -> gamma                0.1  -0.34
 .   -> gamma                            0.0  -0.22
 -> K-                                   0.1  -3.46
 -> Pi-                                  0.1  -2.03
```

Figure 1.12: An example of top quark fragmentation.

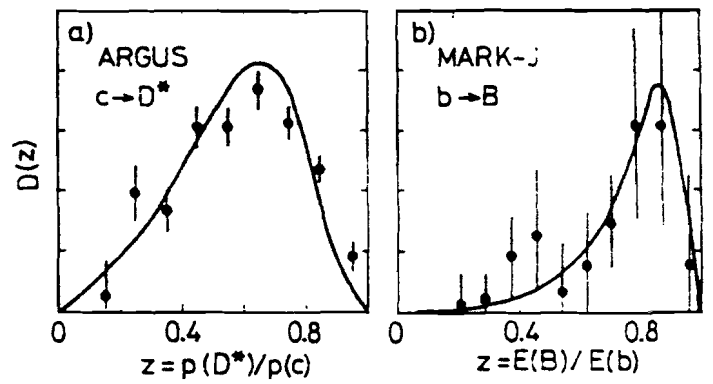

Figure 1.13: The fragmentation functions for $c \to D^*$ and $b \to B$ from the Argus and Mark-J experiments, compared to Peterson model for $\epsilon = 0.18$ and $\epsilon = 0.018$ respectively. From reference [31].

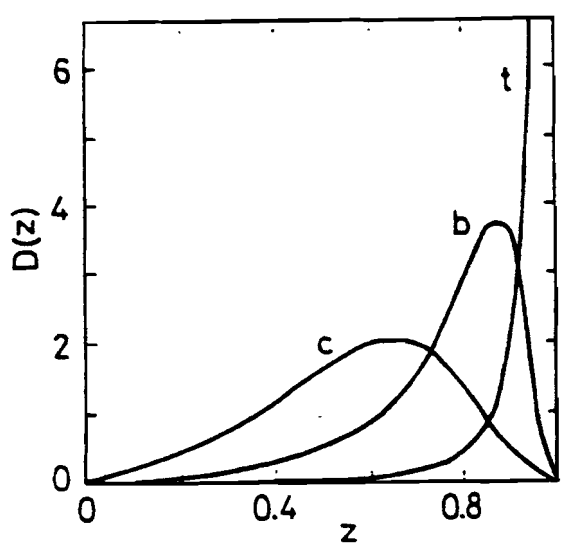

Figure 1.14: Comparison of the $Q = c, b, t$ fragmentation functions in the Peterson model, assuming $\epsilon = 0.40/m_Q^2$ with $m_c = 1.5, m_b = 4.7$ and $m_t = 40$ GeV/c^2. From reference [31].

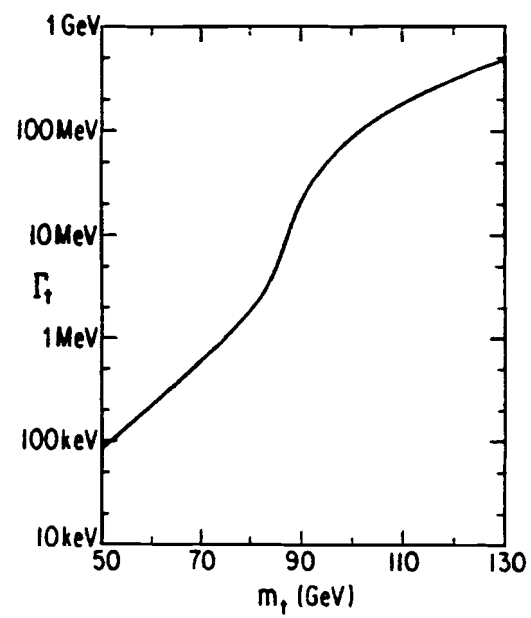

Figure 1.15: Decay width Γ_{top} for the top quark as a function of its mass. At low mass $\Gamma_{top} \sim M_{top}^5$, at large mass $\Gamma_{top} \sim M_{top}^3$. From reference [32].

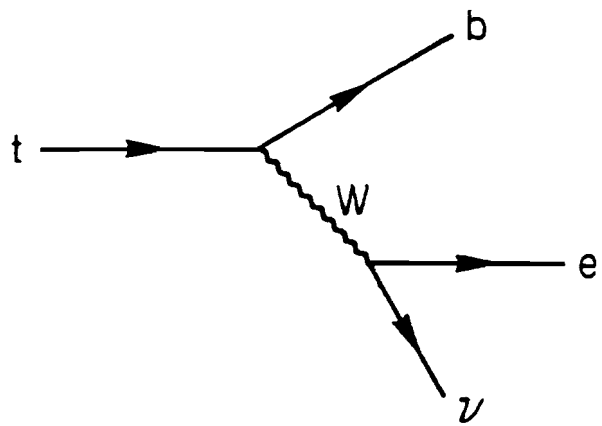

Figure 1.16: The weak charged current decay of the top quark.

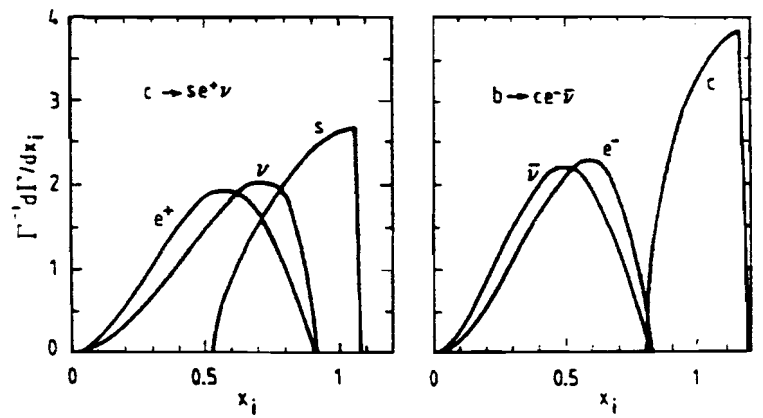

Figure 1.17: The fractional energy spectra $x_i = 2E_i/m_Q$ of decay leptons and quarks for b and c semileptonic decays. From reference [31].

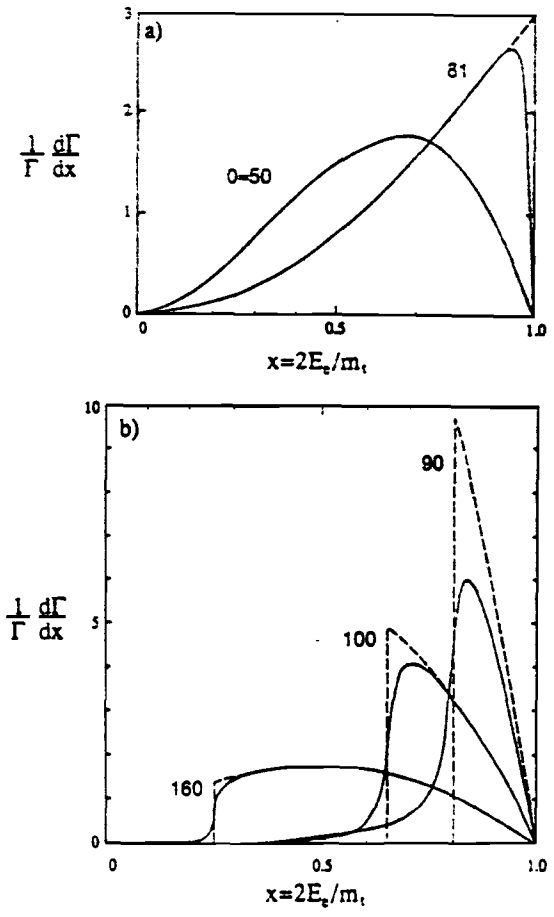

Figure 1.18: The charged lepton spectrum in $t \to bl\nu$ for different top masses. The dashed lines correspond to the approximation of zero W width. From reference [33].

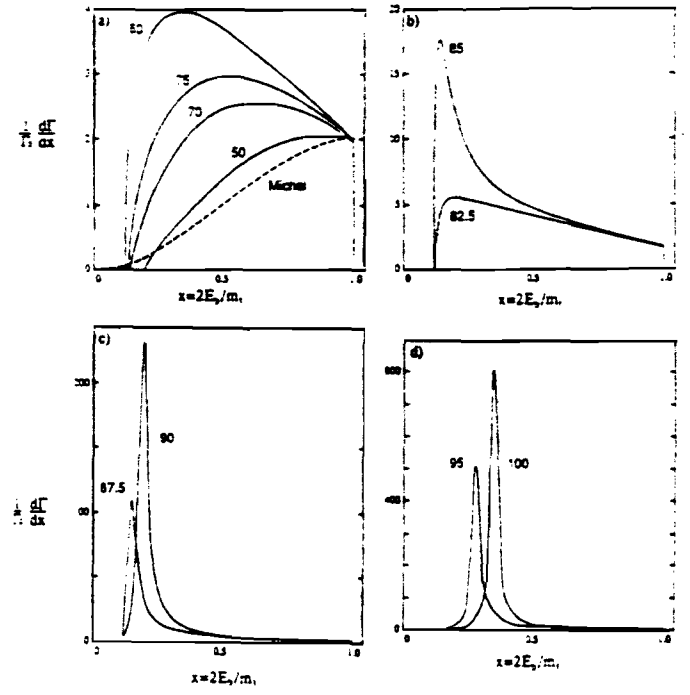

Figure 1.19: The bottom quark spectrum in $t \to bl\nu$ for different top masses. From reference [33].

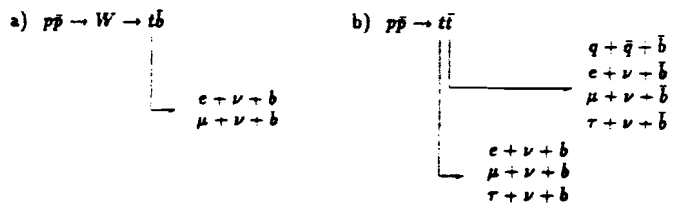

$e + \nu + 2$ jets	$(\frac{1}{9})$
$\mu + \nu + 2$ jets	$(\frac{1}{9})$

$e + \nu +$ 4 jets	$(\frac{12}{81})$
$\mu + \nu +$ 4 jets	$(\frac{12}{81})$
$e + e + \nu s + 4$ jets	$(\frac{1}{81})$
$e + \mu + \nu s + 4$ jets	$(\frac{2}{81})$
$\mu + \mu + \nu s + 4$ jets	$(\frac{1}{81})$
$e + \tau + \nu s + 4$ jets	$(\frac{2}{81})$
$\mu + \tau + \nu s + 4$ jets	$(\frac{2}{81})$

Figure 1.20: Parton final states and event topologies for a) W decay and b) top pair production. Only final states containing at least one electron or muon from the top decay are shown. The branching ratios are indicated in parentheses.

Chapter 2

EXPERIMENT SETUP

2.1 THE TEVATRON

The Tevatron [36,37,38] is a two-kilometer diameter proton-antiproton accelerator, located in the Fermi National Accelerator Laboratory in Batavia, Illinois. It is the world's highest energy accelerator system and the first large-scale superconducting synchroton. In the recent 1988-1989 collider run, the Tevatron operated at a beam energy of 900 GeV, that is, a $p\bar{p}$ center-of-mass energy of 1.8 TeV. Typical starting luminosities were $\mathcal{L} \sim 2 \times 10^{30}$ cm^{-2}s^{-1}, and the beam lifetimes were in the range 12-24 hours. An integrated luminosity of $\int \mathcal{L} dt = 9.7$ pb^{-1} was delivered over the 10-month run. The CDF detector recorded 4.7 pb^{-1} of data to tape. It is to be noted that the initial goal for the run was to record 1 pb^{-1}, and the extraordinary performance of the accelerator exceeded all expectations.

Figure 2.1 shows the Fermilab accelerator complex. The Tevatron ring of superconducting magnets is located beneath the original Fermilab accelerator known as the Main Ring, in the same tunnel. The Main Ring is a 400 GeV proton accelerator made with conventional magnets. In collider operation, the Main Ring serves for injecting 150 GeV protons and antiprotons into the Tevatron for further acceleration. It also provides a 120 GeV proton beam which is targeted for producing the antiprotons for the collider.

The accelerator chain leading to protons in the Main Ring consists of a 200 MeV Linac feeding an 8 Gev Booster Accelerator which injects the protons into the Main Ring. Delivering antiprotons to the Main Ring for their subsequent injection to the Tevatron is much more complicated. The ensemble of beamlines and rings show in figure 2.2 is referred to as the Antiproton Source. Batches

of Protons from the Booster are sent to the Main Ring, accelerated to 120 GeV, and dumped to an antiproton production target. The phase space density of the resulting 8 GeV antiprotons is increased by a factor of ~ 10 in two concentric triangular accelerators, the Debuncher (outer) and the Accumulator (inner), before they are sent to the Main Ring. The stacking rate of antiptotons in the Accumulator is 2×10^{10} $\bar{p}$/hour.

When a suitable stack of $\sim 4 \times 10^{11}$ antiprotons has been achieved, a portion is extracted in 13 'buckets' which are injected in the Main Ring, where they are accelerated to 150 GeV and then coalesced into a single bunch which is injected to the Tevatron ring. The whole cycle is repeated until 6 bunches of antiprotons are left circulating inside the Tevatron (at 150 GeV) in opposite direction with other 6 bunches of protons previously injected. With 12 bunches in the Tevatron (6 proton and 6 antiproton), a process of adjusting the interaction points (cogging) takes place so that the crossings are centered in B0, the place along the ring where the CDF detector is located. Then, the Tevatron is ramped to the full energy, and when the store at 900 GeV becomes stable, a system of quadrupole magnets (the low-beta quads) is energized to focus or squeeze the beams to achieve a high $p\bar{p}$ interaction rate.

2.2 THE CDF DETECTOR

The Collider Detector at Fermilab (CDF) [39] was built to study the collisions of protons with antiprotons at the Fermilab Tevatron Collider. Perspective and cutaway views of the CDF are shown in figures 2.3 and 2.4. The approximate dimensions of the detector are 26 m (length) $\times$ 9 m (height) $\times$ 8 m (width), it weighs $\sim$ 5000 tons and has $\sim$ 70000 channels of electronic readout.

Particles emerging from the interaction point will encounter in sequence a vertex time projection chamber (VTPC) which provides tracking information for vertex reconstruction: a central tracking chamber (CTC) imbedded in a magnetic field for measuring charged particle momenta; electromagnetic and hadronic calorimeters for measuring particle energies; and muon detectors. In this section

we describe some features of the detector important to the analysis presented in this thesis.

The CDF coordinate system is shown in figure 2.3. It is a right handed coordinate system with the positive Z axis pointing along the proton direction (east), the positive Y axis pointing upwards, and the positive X axis pointing outwards from the beam circle. Cylindrical coordinates (R, θ, ϕ), with R being the perpendicular distance to the beamline, ϕ the azimuthal angle, and θ the polar angle with respect to the Z axis, are also shown in figure 2.3. The pseudorapidity, defined as $\eta = -\ln(\tan(\theta/2))$, is often used instead of the polar angle θ.

2.2.1 Tracking

Vertex Time Projection Chamber

The Vertex Time Projection Chamber (VTPC) [40], shown in figure 2.5, consists of 8 time projection chamber modules which extend 1.4 m along the beam , on each side of the center of the detector. The most important function of the VTPC is to provide the necessary tracking information for Z-vertex determination. The event Z-vertex at the Tevatron has a Gaussian distribution with a σ of 35 cm, well covered by the VTPC. The VTPC surrounds a 5 cm diameter beryllium beam pipe and is itself surrounded by the central tracking chamber (CTC). The active volume of the VTPC extends in the radial direction from R=7 cm to R=21 cm, covering the region $|\eta| < 3.25$ (or $3.5° < \theta < 176.5$).

Each of the modules is divided into two 15 cm drift regions by a center high voltage grid. The drift regions are divided into 8 octants. Electrons drifting away from the center grid will reach the endcap octant which has 24 parallel sense wires strung perpendicular to the radial direction in the R-ϕ plane. There are 3072 sense wires (8 modules $\times$ 16 octants/module $\times$ 24 wires per octant). The times of arrival of the electrons to the wires are read out with FASTBUS TDCs and allow track reconstruction in the R-Z plane. By finding the convergence point of all the tracks in the event, the event Z-vertex is reconstructed with a typical resolution of $\sim$ 0.3 cm. Each octant endcap also has 24 pads (at total of 3072 for

Search for the top... FAB1759

E- ?

THESIS

CDF Collab.

1. Quarks.
2. Proton-antiproton interactions.

the whole VTPC) arranged in three rows which are read out by FASTBUS FADCs and provide ϕ information. The track ϕ is determined by fitting a Gaussian to the measured charge distribution on a pad row. The resolution in the ϕ determination is of $\sim 0.5°$. The pad data together with R-Z wire reconstruction information provide complete three-dimensional tracking which is most useful in the region $1.0 < |\eta| < 2.0$ (or $15° < \theta < 30°$) to complement the limited CTC information, and in the region $2.0 < |\eta| < 3.25$ (or $3.5° < \theta < 15°$) where the VTPC gives the only tracking available.

Central Tracking Chamber

The Central Tracking Chamber (CTC) [41] is a cylindrical drift chamber ,with inner radius of 0.28 m and outer radius of 1.38 m, which extends 1.60 m along the beam-line on each side of the center of the detector. It is located outside of the VTPC and inside a superconducting solenoidal magnet that provides a uniform 1.4 Tesla magnetic field parallel to the beam direction (see figure 2.4). The CTC covers the region $|\eta| < 2.0$ (or $15° < \theta < 165°$).

The most important function of the CTC is to provide a measurement of the momentum of charged particles to be used both at the trigger level and in the off-line analysis.

The chamber has 84 layers of sense wires which are grouped into 9 superlayers. Five of the superlayers, which consist of 12 sense layers of wires strung parallel to the beam-line, are called axial superlayers, and provide information for track reconstruction in R-ϕ. The other four superlayers are called stereo superlayers and are interleaved with the five axial superlayers. The stereo superlayers provide tracking information in the R-Z plane, they have 6 layers of wires each, with their wires strung with an angle to the beam line that alternates from $+3°$ to $-3°$ from one stereo superlayer to another. The superlayers are didived into cells which are rotated by 45° with respect to the radial direction (see figure 2.6). The electric field is by construction perpendicular to the direction of the cell, and the 45° cell tilt was chosen in so that direction of the drifting electrons in the gas (which

are subjected to the Lorentz force of the crossed electric and magnetic fields) is approximately perpendicular to the radial direction. There are 660 cells in the chamber, with the number of cells per superlayer increasing from 30 (innermost superlayer) to 120 (outermost superlayer). The axial cells have 12 sense wires and the stereo cells have 6 sense wires, totaling 6156 sense wires for the chamber. Each of the wires is read out with FASTBUS multiple hit TDCs.

The momentum resolution of the CTC for tracks in the region $|\eta| < 1.0$ (or $40° < \theta < 140°$) is $\Delta P_T/P_T^2 = 0.0017(\text{ GeV}/c)^{-1}$. This resolution can be improved by imposing the requirement that the tracks emanate from the beam-line. The beam position may be displaced from the origin by a few hundred microns, and its position is determined for each store by studying the distribution of the track impact parameter (distance of closest aproach of the track to the Z axis) as a function of the ϕ for all tracks. The resolution of the central tracking chamber with a beam-constrained fit is $\Delta P_T/P_T^2 = 0.0011(\text{ GeV}/c)^{-1}$. The tracking resolution degrades beyond $|\eta| = 1.0$, that is, for tracks which do not cross all the superlayers. At $\eta = 1.7$ (or $\theta = 20°$) , for instance, the resolution for the beam-constrained case is $\Delta P_T/P_T^2 = 0.004(\text{ GeV}/c)^{-1}$.

2.2.2 Calorimetry

The calorimeters cover the region $|\eta| < 4.2$ (or down to $\sim 2°$ relative to the beam axis) and are organized into systems covering different regions in η : central electromagnetic (EM) and hadronic (HAD) calorimeters, endwall HAD calorimeter, plug EM and HAD calorimeters, and forward EM and HAD calorimeters. The CDF calorimeters are subdivided into 'towers' or cells in $\eta - \phi$ space which project back to the interaction region. Each tower contains an electromagnetic compartment and a hadronic compartment. The coverage and $\eta - \phi$ segmentation are shown in figure 2.7 for the hadron calorimeters. The electromagnetic calorimeters have a slightly different sharing of the rapidity coverage. The central and endwall calorimeters consist of alternating layers of plastic scintillator and absorber. For the plug and forward regions (gas calorimetry), proportional chambers are used

instead of scintillator. For absorber, the hadron calorimeters use steel, and the EM calorimeters use lead. Table 2.1 summarizes the properties of the calorimeters by system. We now describe some of the features of the central and endwall calorimeters which are more relevant for the analysis of this thesis.

Central Electromagnetic Calorimeter

The central calorimeter is divided into 4 'arches'. Each arch consists of 12 15° wedges stacked to form an upright semi-circle. Two arches touch each other side-by-side and face the other set of two arches at $\eta = 0$, and the assemblage covers the the pseudo-rapidity region up to $\eta = \pm 1.1$ and the full $\phi = 2\pi$ azimuth. The central electromagnetic calorimeter (CEM)[42] is a lead-scintillator sampling calorimeter occupying the bottom part of each of the 48 15° central calorimeter wedges.

There are 31 layers of 5 mm thick scintillator, interleaved with 30 layers of $\frac{1}{8}$ inch lead giving a total of ~ 18 radiation lengths (X_0), including $\sim 1X_0$ from the solenoid magnet coil. Each wedge like the one shown in figure 2.8 contains 10 towers (denoted 0-9, with tower 0 being the closest to $\eta = 0$) of $\Delta\eta \sim 0.1$ each. Light from the scintillator in each tower is collected on wavelength shifters and sent through lightguides into two phototubes.

The energy resolution of the CEM for electrons is $\Delta E/E \sim 0.14/\sqrt{E}$. The energy scale was determined at the test beam, and Cs^{137} sources are used to track the energy response to $\sim 1\%$. A more sophisticated *in situ* self-calibration scheme using the E/P (calorimeter energy-to-track momentum) distribution of an inclusive electron sample was used to determine the Z^0 mass with an uncertainty due to the calorimeter energy scale of $\sim 0.2\%$ [43].

Strip Chambers

The central electromagnetic calorimeter is instrumented with a proportional wire chamber, known as strip chamber (CES)[42,44]. The strip chamber is located at a depth of 5.9 X_0 (including the solenoidal coil). The shower maximum in

radiation lengths for electrons is given by $t_{max} = 6.2 + \ln(E/10)$ [44], so the strip chamber is located near shower maximum for a large range of energies. The main purpose of the chamber is to determine the position of electron and photon showers and to allow separation of multiple showers in a single tower. Each chamber covers all ten towers of a calorimeter wedge and provides pulse height readout in two orthogonal views: anode wires strung along the beam direction give the ϕ information and cathode strips that run in the ϕ direction give the η information. The chamber is divided in two sections at 53° from the beam axis (or $\eta = 0.70$) : the 90° side and the 45° side. There are 32 anode wire logical cells, each 14.5 mm in width, read out on each of the halves. There are 69 16.7 mm wide cathode strip channels on the 90° half and 59 20.1 mm wide strip channels on the 45° side. An electron is typically well contained within five cells in either view. The position relolution from test-beam measurements is ~ 2 mm for 40 GeV test-beam electrons and behaves as $(1/\sqrt{pulseheight})$. A χ^2 variable useful in discriminating against multiple showers is described in Chapter 3.

Central and Endwall Hadronic Calorimeters

The central hadron calorimeter [45] has the same $\eta - \phi$ segmentation as the central electromagnetic calorimeter, but it only reaches until tower 8. The endwall modules extend the coverage of the central hadron calorimeter out to $\eta = 1.3$; hadronic towers 6, 7 and 8 are shared between the central and endwall calorimeters (see figure 2.9). Each central hadron calorimeter wedge has 32 2.5 cm steel layers interleaved with 1 cm layers of scintillator. The endwall hadron calorimeter modules have 15 5 cm layers of steel interleaved with 1 cm layers of scintillator. The depth in absorption lengths is 4.7 λ and 4.5 λ for the central and enwall calorimeters, respectively. The energy resolution of the calorimeters, measured at the testbeam for 50 GeV pions, is 11% and 14% for the central and endwall, respectively.

2.2.3 Muon Detectors

CDF has two systems to detect muons which have penetrated the calorimeters: (1) a forward-backward muon spectrometer [46] composed of large magnetized steel toroids with drift chamber planes and triggering scintillation counters, covering the region between 3° and 16° relative to the beam axis, and (2) a central muon system covering the region $|\eta| < 0.63$. We will describe the second system, which was used for our analysis.

Central Muon System

The central muon detector [47,48,49] is placed at a radial distance of 3.47 m from the beam-line, outside of the central hadron calorimeter, covering the region of $|\eta| < 0.63$ (or down to 56° with respect to the beam axis). Muons are identified by their penetration of the 4.9 absorption lengths of the central calorimeter; the muon detector measures their positions and provides a level-one trigger (momentum measurement). The geometry of the muon detector is shown in figure 2.10. Each central calorimeter wedge fits a muon detector wedge 2.26 m long and subtending 12.6° in ϕ (this leaves 2.4° gaps between muon wedges). The muon detector wedges are subdivided into three drift chamber modules of 4.2° each, giving a total of 144 modules (48 wedges × 3 modules/wedge) in the detector.

Figure 2.11 shows the cross section of a muon drift chamber. The chambers have 4 layers in the radial direction, and each layer has 4 cells. Each cell contains a wire which is strung along the length of the chamber. Sense wires from alternate cells within the same layer are connected on one end of the wedge and are read out independently on the other side making possible a Z determination by charge division.

When a particle traverses the chamber, it hits four sense wires (see figure 2.11). Wires of the two outer layers are offset by 2 mm from the wires of the two inner layers. By determining which pair of sense wires was hit first, the track ambiguity in ϕ can be resolved. The angle α between the track and the sense wires can be measured by comparing the times of arrival of the drift electrons to sense wires in

alternating layers. The relationship between this angle and the track transverse momentum is given approximately by $\alpha = \frac{eL^2B}{2DP_T} = 130$ mR$/P_T$, where e is the electron charge, $B = 1.4$ T is the magnitude of the magnetic field, L is the radius of the solenoid, and D is the radial distance to the muon chambers. Therefore, the muon chambers provide a measurement of the muon transverse momentum. Multiple scattering in the calorimeter steel will deflect the muons by 85 mR$/P_T$ and dominates the momentum resolution which is $\Delta P/P = \Delta\alpha/\alpha = 65\%$.

2.2.4 Trigger

The objective of the CDF trigger system [50] is to reduce the event rate from the $p\bar{p}$ inelastic collision rate of ~ 60 KHz (at $\mathcal{L} = 10^{30}$ cm^{-2}s^{-1}), to a rate of ~ 1 Hz (output to magnetic tape) which must contain the events necessary for studying known or expected physics (such as QCD jets, W/Z bosons, bottom and top quark, etc.) as well as possible unexpected physics. Thus, the trigger was designed to make decisions based on the topology of the transverse energy in the event (total transverse energy, missing transverse energy), and on the identification of leptons (electrons, muons, and taus), photons, and jets. The trigger has 4 levels of decision, denoted levels 0 through 3. The Level-0 trigger uses scintillation counters for detecting inelastic $p\bar{p}$ collisions. Level-1 and Level-2 are a system of FASTBUS-based microcoded processors; full readout of the detector components is done after the Level-2 decision. The Level-3 trigger consists of a 'farm' of VME-based processors running offline-like algorithms to improve background rejection.

Level-0

At Level-0, hits in both the East and West beam-beam counters are required to coincide, inside a 15 ns window centered in the beam crossing time. The beam-beam counters (BBC) [51] are two planes of scintillation counters located perpendicular to the beam-line, at a distance of 591 cm from the interaction region (one to the east, and one to the west). Each plane consists of 16 time-of-flight counters which are arranged as shown in figure 2.12. The BBC cover the region

$3.24 < |\eta| < 5.90$ (or from 0.32° to 4.47° with respect to the beam-line). The BBC provide a measurement of the integrated luminosity for the experiment which is used for both on-line luminosity monitoring and for physics analyses [52]. The presence of a beam-beam counter 'minimum bias' trigger (with a rate of 44 KHz at $\mathcal{L} = 10^{30}$ cm^{-2}s^{-1}) is a prerequisite for subsequent levels of triggering.

Level-1

At Level-1, a decision is made in the 3.5 μs between beam crossings based on information that includes the total transverse energy in the event (separate totals for EM and hadron are available), the presence of stiff tracks in the CTC, and the existence of muon candidates in the central muon chambers. The output rate of Level-1 into Level-2 is $\sim$ 1-2 KHz.

Prompt analog signals from the calorimeters are available at Level-1. The analog signals are summed in FASTBUS cards at the trigger end (about 200 ft away from the detector) into logical trigger towers of $\Delta\eta = 0.2$ and $\Delta\phi = 0.15°$. The coarser calorimeter segmentation reduces the number of towers from about 5000 to a more manageable 1000. The towers above a programmable threshold are added and the separate EM and EM+hadron totals are compared to the thresholds (also programmable).

The tracking information available at Level-1 is provided by the hardware Central Fast Tracker (CFT) [53], which uses partial information from the axial superlayers of the CTC to quickly find tracks in 2-dimensions (R-ϕ) with a momentum resolution of $\Delta P_T/P_T^2 = 0.035(\text{ GeV}/c)^{-1}$. On the average, it takes the CFT 2.5 μs to search for all high momentum tracks in an event. The operation of the CFT is based on the fact that any stiff CTC track will cross at least one sense wire of each superlayer within 3.5 mm. For each beam crossing, a pattern of 'prompt hits' is identified by the application of an 80 ns coincidence gate on the fast-out wire data. Momentum determination is achieved by comparing the wire patterns with look-up-tables stored in memory. The CFT has 8 programmable thresholds between 2.5 and 15 GeV.

The central muon Level-1 trigger will occur if the difference in drift times between hits in alternate layers of a muon track, is smaller than a programmable threshold. As seen in Section 2.2.3, this is equivalent to imposing a cut on the curvature, or transverse momentum, of the track.

Level-2

The output rate of Level-1 of 1-2 KHz is reduced by the Level-2 to $\sim$ 3 Hz. Only then, after the Level-2 decision, the time consuming process of reading-out all the detector components ($\sim$ 1 ms) is enabled. The Level-2 trigger decision is made by a set of processors which receive information passed to them from the rest of the Level-2 hardware in the form of 'cluster lists'. The cluster lists include a calorimeter cluster list and a 'golden muon' list.

The calorimeter cluster information originates from special FASTBUS hardware (the Cluster Finder) that uses the trigger tower information to produce a list of clusters with their EM and total E_T, cluster width, position in the detector, and the momenta tracks associated in ϕ. The golden muon list includes the muon position and transverse momenta and is generated by another piece of hardware (the Muon Matchbox), which demands that a Level-1 muon trigger ('brass muon') is matched in ϕ with a stiff track found by the CFT. The Level-2 Processors take the lists and calculate physical quantities on which to base the triggering decision. For example, 'electrons' can be selected based on the the ratio of HAD to total energy, cluster width, and presence of an associated high P_T track. 'Muons' are selected by imposing a cut on the track momentum, and an option to limit the amount of energy in the associated calorimeter cell is also possible. Other triggers include Tau , Photon , Dilepton , Jet , Sum Et, and Missing Et triggers. The entire Level-2 decision takes approximately 10 μs, and the output rate into Level-3 is $\sim$ 3 Hz.

Level-3

After an event passes the Level-2 trigger, the data from the detector are digitized and read by scanner modules. The data from the scanners are then read by the Event Builder (a set of FASTBUS modules), which formats them into the standard CDF data format and pushes the event into Level-3. Level-3 [54,55] is an array or farm of VME based parallel micro-processors developed by Fermilab's Advanced Computer Program (ACP). Currently Level-3 consists of 58 ACP nodes executing filter algorithms written in FORTRAN. The algorithms are very similar to those used in the off-line analysis and take advantage of better clustering and tracking (as compared to Level-2) for sharpening thresholds, better particle identification and removal of various kinds of noise. Existing Level-3 filters include Missing E_T, Central Muon, Central Photon, Diphoton, and Forward Muon filters. The Level-3 filtering rejects $\sim$ 50% of the events, and has an output rate to tape of 1-2 Hz.

	Central		Endwall	Endplug		Forward	
	EM	Hadron	Hadron	EM	Hadron	EM	Hadron
$\lvert\eta\rvert$ coverage	0–1.1	0–0.9	0.7–1.3	1.1–2.4	1.3–2.4	2.2–4.2	2.3–4.2
Tower size, $\Delta\eta \times \Delta\phi$	$\sim 0.1 \times 15°$	$\sim 0.1 \times 15°$	$\sim 0.1 \times 15°$	$0.09 \times 5°$	$0.09 \times 5°$	$0.1 \times 5°$	$0.1 \times 5°$
Longitudinal samples in tower	1 [a]	1	1	3	1	2	1
Active medium	polystyrene scintillator	acrylic scintillator	acrylic scintillator	Proportional tube chambers with cathode pad readout		Proportional tube chambers with cathode pad readout	
Scintillator thickness or proportional tube size	0.5 cm	1.0 cm	1.0 cm	0.7×0.7 cm^2	1.4×0.8 cm^2	1.0×0.7 cm^2	1.5×1.0 cm^2
Number of layers	31	32	15	34	20	30	27
Absorber	Pb	Fe	Fe	Pb	Fe	94% Pb, 6% Sb	Fe
Absorber thickness [cm]	0.32	2.5	5.1	0.27	5.1	0.48	5.1
Typical phototube or wire high voltage [V]	~ 1400	~ 1500	~ 1100	~ 1700	~ 2120	~ 1900	~ 2200
Typical phototube or wire gain	1.2×10^5	6×10^5	10^6	2×10^5	2×10^6	5×10^5	10^6
Typical tower signal [pC/GeV]	~ 4	~ 4	~ 4	~ 1.25	~ 1.3	~ 2	~ 0.7
Energy (σ/E) resolution at 50 GeV [%]	2	11	14	4	20	4	20
Typical position resolution at 50 GeV [cm^2]	0.2×0.2 [b]	10×5	10×5	0.2×0.2	2×2	0.2×0.2	3×3
Characteristic width of azimuthal boundary region [cm]	3.5	4.1	3.8, 8.9 alternating	0.9	0.8	0.7 3.2 [b]	1.3 3.2 [b]

[a] An embedded proportional tube chamber at shower maximum gives some additional information. The quoted position resolution is measured with this chamber.

[b] The first number is for the vertical boundary, the second for the horizontal

Table 2.1: Summary of Calorimeter Characteristics

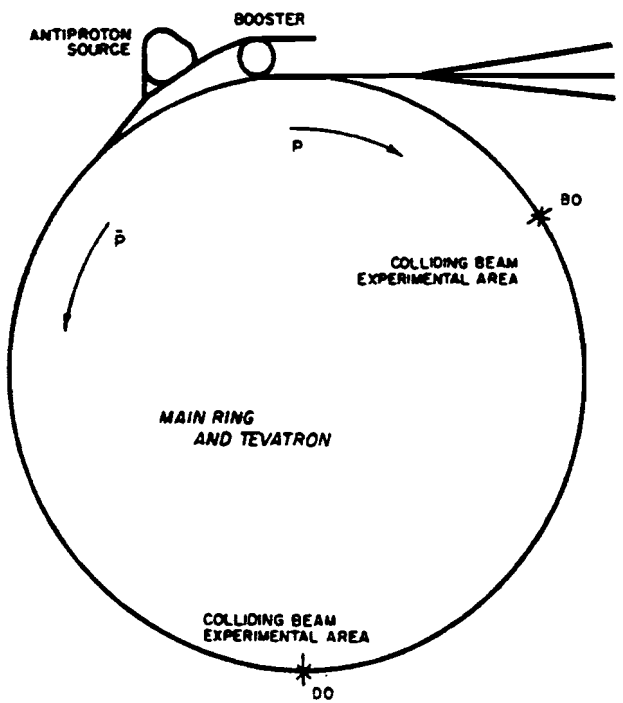

Figure 2.1: The Fermilab accelerator complex.

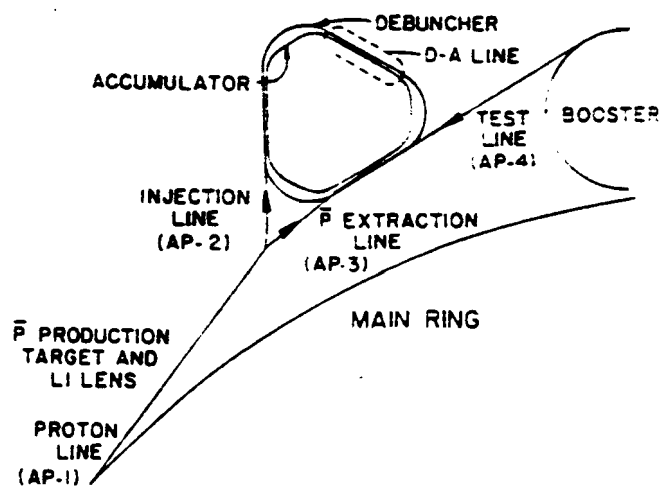

Figure 2.2: The Antiproton Source.

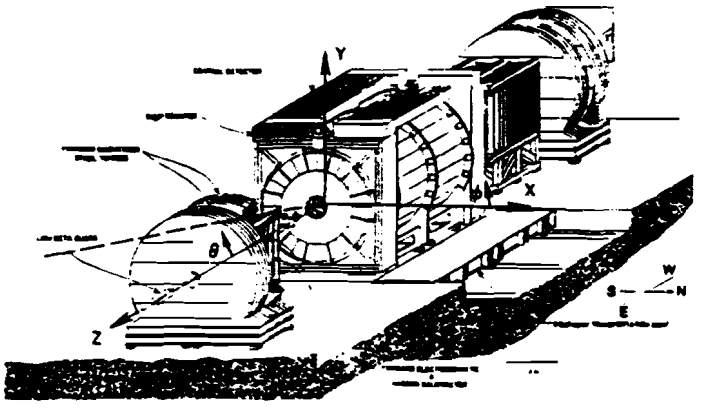

Figure 2.3: A squematic perspective view of the CDF detector.

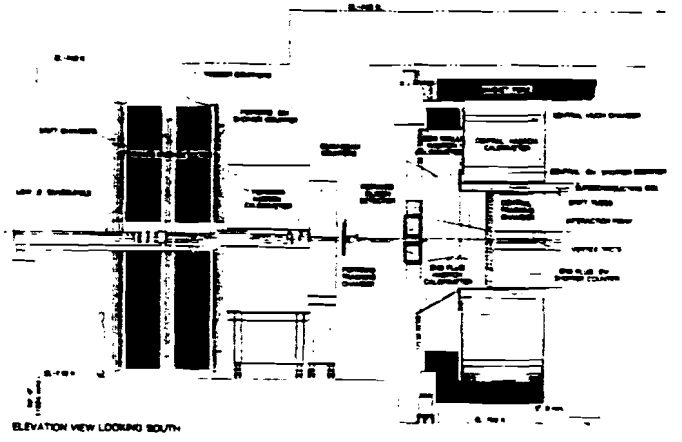

Figure 2.4: A cut-away view of the forward half of the CDF. The detector is forward-backward symmetric about the interaction point.

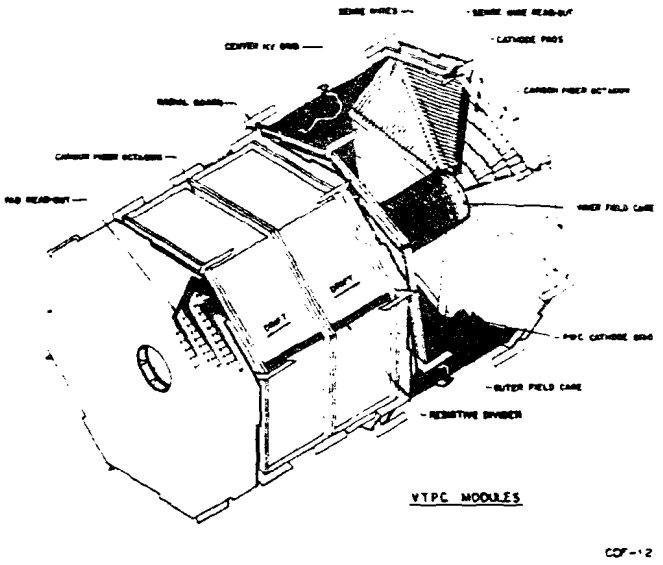

Figure 2.5: Schematic view of two of the VTPC modules.

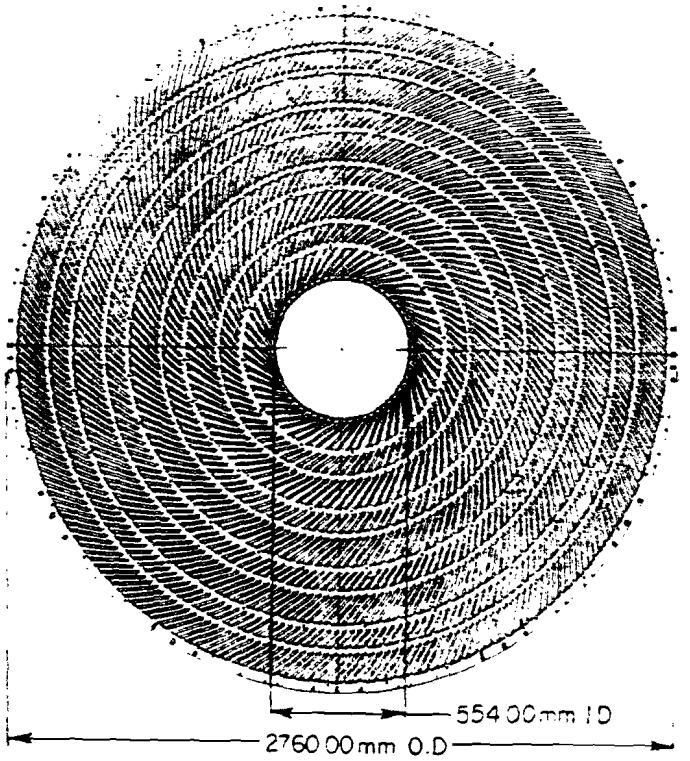

Figure 2.6: End view of the Central Tracking Chamber showing the disposition of the superlayers and cells within the superlayers.

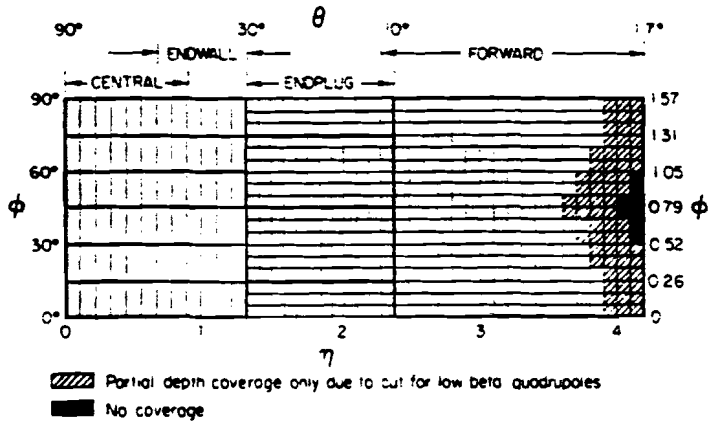

Figure 2.7: A 90° section of hadron calorimeter towers. Module or calorimeter system boundaries are indicated with heavy lines. The ϕ coverage of the EM calorimeters is complete out to $|\eta| = 4.2$.

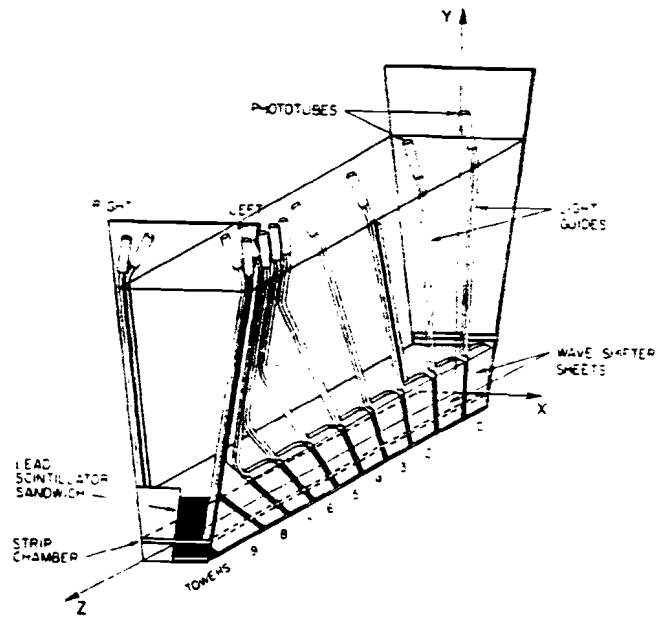

Figure 2.8: A central calorimeter wedge, showing the light-gathering system.

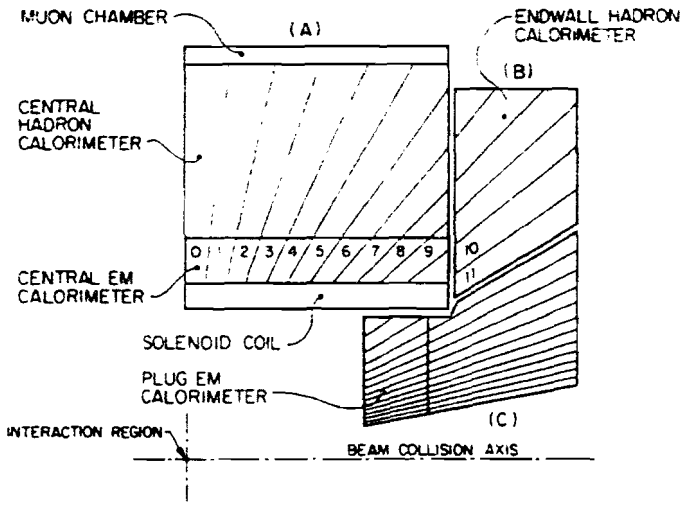

Figure 2.9: Quadrant of the calorimeter where A, B, C show the central, endwall and plug respectively.

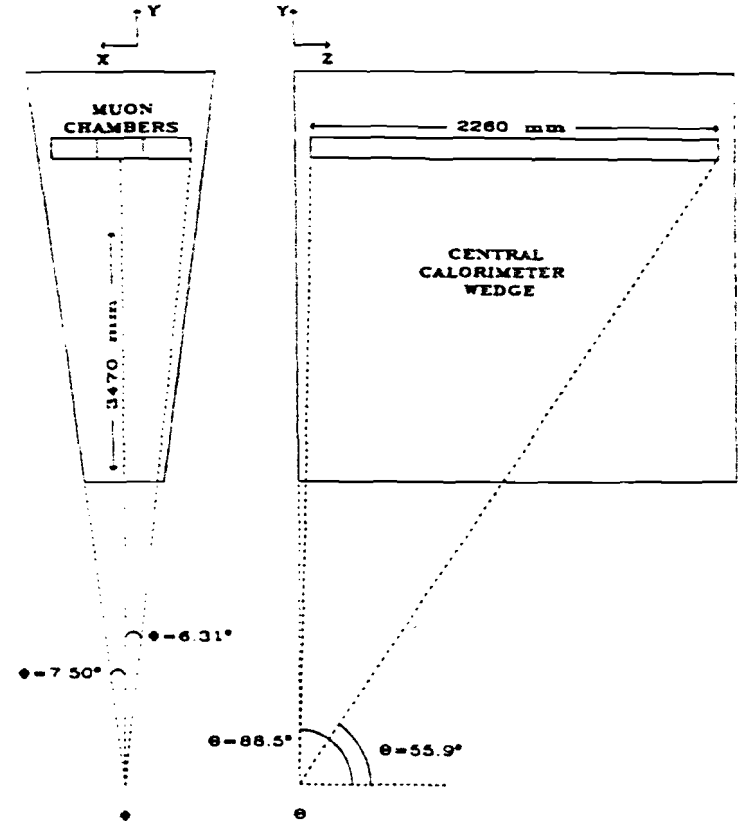

Figure 2.10: Central muon chamber location with respect to a central calorimeter wedge.

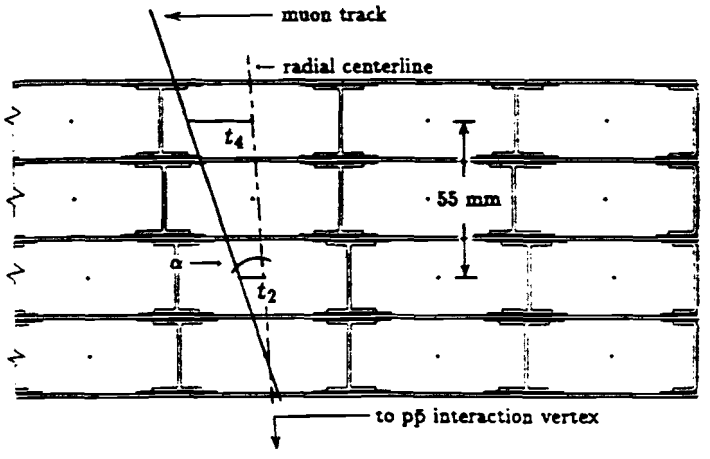

Figure 2.11: Cross section of a central muon chamber.

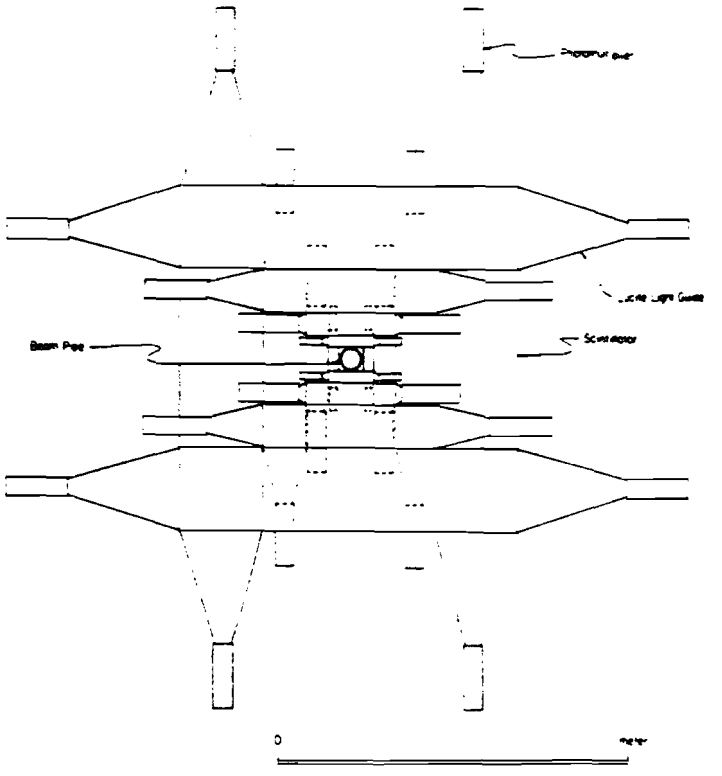

Figure 2.12: One plane of beam-beam counters viewed from the beam-line.

Chapter 3

DATA ANALYSIS I : EVENT SELECTION

3.1 TRIGGERING

The CDF trigger system makes a selection based many physics quantities or objects such as total transverse energy, missing transverse energy, jets, photons, electrons, muons, taus, dileptons, etc. Reference [56] describes the triggers used in the 1988-1989 CDF Run. Three of the triggers are capable of detecting Electron-Muon events. There are an inclusive electron trigger with a nominal threshold of $E_T^e > 12$ GeV, an inclusive muon trigger with nominal threshold of $P_T^\mu > 9$ GeV, and an electron-muon trigger with threshold $(E_T^e, P_T^\mu) > (5$ GeV, 5 GeV/$c)$.

Since events for the top search are required to contain a high E_T electron accompanied by a muon which may or not enter the muon chambers (and therefore the muon will not always fire the trigger), the most relevant trigger is the ELECTRON_12 trigger. We find that this trigger is highly efficient for the events in the top quark signal region.

Given the high efficiency of the ELECTRON_12 trigger, the value for this analysis of the MUON_9 and ELECTRON_5_MUON_5 triggers is that they provide a sample of low P_T events with sufficient statistics to show consistency between the $e\mu$ data and expectations from $b\bar{b}$ production.

3.1.1 Inclusive Electron Trigger

The electron trigger requirements are:

(1) A CEM trigger tower with $E_T^{EM} > 6$ GeV is reqired at the Level-1 trigger.

(2) At Level-2, a cluster with $E_T^{EM} > 12$ GeV and with $HAD/EM < 0.125$ is required with a CFT track with $P_T > 6$ GeV/c pointing at it.

(3) At the Level-3 trigger the thresholds are sharpened and other cuts are applied [57]. The same electron clustering algorithm used in the off-line (with finer calorimeter segmentation than the Level-2 clustering) is used, and events are required to have a cluster with transverse EM energy $E_T^{EM} > 12$ GeV and with a ratio of electromagnetic to hadronic energy $HAD/EM < 0.125$. A fast track reconstruction with momentum resolution $\Delta P_T/P_T^2 = 0.007($ GeV/$c)^{-1}$ is used, and a track with transverse momentum above 6 GeV/c is required. There are no further cuts on candidates with $E_T^{EM} > 20$ GeV; for candidates in the region 12 GeV $< E_T^{EM} <$ 20 GeV a lateral sharing cut of $Lshr < 0.5$ ($Lshr$ is defined later in this chapter) is applied.

The turn-on efficiency of the ELECTRON_12 trigger has been measured using data collected by a lower threshold (7 GeV) electron trigger [58,59]. The fraction of clusters (selected for having satisfied the 7 GeV electron trigger plus some electron quality cuts) which also pass the 12 GeV trigger is determined as a function of cluster E_T. The result is shown in figure 3.1, and it is seen that the 12 GeV Electron trigger reaches full efficiency at about 15 GeV. More precisely, this efficiency has been determined [59] to be (98.0 ± 0.5) % for electrons with $E_T^e > 15$ GeV inside the fiducial region of the CEM calorimeter. Consistency checks of the previous measurement were possible by checking whether the ELECTRON_12 trigger was satisfied for electrons in data collected with a missing E_T trigger (with a treshold of 25 GeV), and in data from Photon triggers (with thresholds of 10 GeV and 23 GeV).

3.1.2 Inclusive Muon Trigger

(1) At Level-1, the difference in drift times in at least one out of two pairs of alternate layers must be below a threshold defined to be 50% efficient for 5 GeV/c muons. The Level-1 threshold was lowered to 3 GeV/c for $\sim$ the second half of the 88-89 Run [60].

(2) At Level-2 a CFT track with transverse momentum above 9.2 GeV/c (90% efficiency point) is required.

(3) A Level-3 track with transverse momentum above 11 GeV/c is required to match the muon chamber hits within ± 10 cm in ϕ.

The muon trigger efficiency has been studied in references [58,61,62]. The turn-on shape of the trigger is studied by looking at muon candidates in data collected with other triggers and it is found to be consistent with expectations from multiple scattering. The efficiency for muons with $P_T > 15$ GeV/c, determined from cosmic-ray data gathered during special running periods and from muons in events passing other triggers, is found to be $(90.0 \pm 0.2)\%$[61,62]. The best hypothesis as to why the efficiency is not higher at such high P_T is that sometimes the muon will cause a δ-ray to be emitted and the anomalous drift times will confuse the triggering condition.

3.1.3 Electron-Muon Trigger

The definitions of electron and muon for this trigger are similar to the inclusive triggers already described, with different thresholds.

(1) At Level-1, at least one trigger tower with $E_T^{EM} > 3$ GeV is required. The inclusive muon Level-1 trigger is also required.

(2) At Level-2 a cluster with $E_T^{EM} > 5$ GeV and with $HAD/EM < 0.125$ is required with a CFT track with $P_T > 4.8$ GeV/c pointing at it. In addition, the muon stub trigger must be matched in ϕ with CFT track above 4.8 GeV/c (or 3 GeV/c for the ~ the second half of the 88-89 Run).

(3) At Level-3, two tracks above 3 GeV/c are required.

The efficiency of the electron-muon trigger was studied [58] for a small data sample taken before the Level-1 muon threshold was lowered to 3 GeV/c. A more complete study is still needed , but we will mention the technique employed and the result that indicates good efficiency for the $e\mu$ trigger. The electron and muon

parts were studied separately. Electrons above 5 GeV passing standard electron identification cuts were selected from a sample of muon triggers. Since a muon trigger was already present, the determination of the efficiency of the electron part of trigger (as a function of E_T^e) was possible by checking whether the $e\mu$ was satisfied. Similarly, the muon part was tested by selecting muons from a sample of electron triggers. Since an electron trigger was already present, the efficiency of the muon part of the trigger (as a function of P_T^μ) was determined by checking the status of the $e\mu$ trigger. It was concluded that the electron-muon trigger is ~ 75% efficient near the ($E_T^e = 5$ GeV, $P_T^\mu = 5$ GeV/c) threshold.

3.2 DATA PROCESSING

Two data processing streams were used for the analysis of this thesis.

Spin

An expressline or 'Spin Cycle' [63] selected electrons and muons with thresholds set high enough to ensure a small number of events for processing, but low enough to capture an important fraction of the 'most interesting' events, including top, possible exotics, and W and Z boson events. Initial selection was based on Level-2 and Level-3 quantities and fast (lower resolution) tracking algorithms, with a small CPU consumption (20 seconds of Vax-780 CPU per event). Once the number of events was significantly reduced, the full reconstruction program (240 seconds of Vax-780 CPU per event) was applied. During the course of the run, Spin was only about two weeks behind data taking and was crucial in allowing fast access to the data for physics analyses and for checking the behavior of the detector. At the time we carried out this analysis,the Spin sample had the advantage of having the full luminosity of the CDF 1988-1989 run.

Spin itself had several output streams. For the top search and for $Z^0 \to e^+e^-$ studies, we used an inclusive electron output stream (TOS03). This stream kept electrons with $E_T^e > 12$ GeV with looser electron quality cuts than used in our analysis. For $Z^0 \to \mu^+\mu^-$ studies we used the muon category of an 'electroweak

physics' output stream (EWS03). Here, all muons with $P_T^\mu > 15$ GeV/c were selected with looser muon quality cuts than used in our analysis.

Production

A standard reconstruction and filtering program, 'Production' [64,65], was applied on all the raw data at a naturally slower pace than Spin. When the analysis of this thesis was finished, roughly half the full luminosity was available from Production, but the lower lepton thresholds allowed the collection of a high statistics $e\mu$ sample for comparison whith expectations from botton quark production. An inclusive muon output stream (MUU00) with a $P_T^\mu > 4$ GeV/c cut (on events passing the electron-muon trigger), and with looser muon quality cuts than used in our analysis, was used to further select events for our $b\bar{b}$ study.

3.3 ELECTRON SELECTION

In this section we define the variables used off-line to identify electrons [66] and give the cut values used. We also present a measurement of the efficiency of the selection criteria on electrons from Z^0 decay.

3.3.1 Electron Selection Criteria

Efficient identification of electrons with minimal isolation requirements is achieved by exploiting the fine granularity of the central calorimeter, the excellent spatial and momentum resolution of the central tracking chamber, and the capabilities of the strip chambers to determine both the position and shape of EM showers in the φ and z views.

Electromagnetic clusters with an associated track are considered for the electron selection. Electron showers are small relative to the tower dimensions and typically deposit most of their energy in a single calorimeter cell. For electrons suffuciently far from wedge edges (~ 2 cm) to guarantee full calorimeter response, the shower will not cross wedge boundaries. Hence, calorimeter clusters for electron (and photon) identification are defined with up to three towers adjacent in

η.

Fiducial Region

Fiducial cuts are applied on the CEM clusters to avoid cracks between calorimeter modules and to ensure proper energy measurement :

(1) The cluster tower with the largest energy deposition (seed) must be one of towers 0-8 of the CEM.

(2) The extrapolated track position at the strip chamber radius ($R_{CES} = 184$ cm) must be at least 2.5 cm away from the boundaries between central calorimeter wedges (15° boundaries).

(3) The strip chamber shower position must at least be 9 cm away from the $Z = 0$ plane (90° crack).

Electron Identification Variables

The following variables are used to identify electrons:

(1) The ratio between the hadronic and EM energy in the cluster: HAD/EM. An almost pure sample of electrons from $W \to e\nu$ was selected by requiring sufficiently high electron transverse energy and missing transverse momentum, namely, $E_T^e > 30$ GeV and $E_T^{miss} > 30$ GeV. Figure 3.3 shows the hadronic fraction distribution for the W electrons and for 50 GeV test-beam electrons and charged pions. There is fair agreement between the W and test-beam electrons for this distribution, and it is seen that the hadronic fraction can be used to select electrons with high efficiency and with good pion rejection.

(2) A measurement of the lateral shower profile of the three-tower cluster : $Lshr$. The lateral shower profile is defined as

$$Lshr = \sum_k \frac{M_k - P_k}{\sqrt{(0.14\sqrt{E})^2 + (\Delta P_k)^2}}, \tag{3.1}$$

where the index k of the summation labels the towers adjacent to the seed. M_k is the measured energy in tower k. P_k is the energy expected in tower k. For determining P_k, the direction of the electron candidate is calculated by using the event vertex Z_{vertex} and the position Z_{strip} of the shower in the strip chambers. Then, an energy-dependent shower profile (with both lateral and longitudinal shower development) obtained from test-beam measurements [57] is used to predict the energy sharing in the adjacent towers. The normalization of the denominator contains the term ΔP_k which is the error in P_k induced by a 1 cm change in the shower position and the term $0.14\sqrt{E}$ which reflects the statistical fluctuations inherent in the energy measurement of EM showers. The electron energy corresponds to the sum of tower EM energies : $E = \sum M_k$.

(3) The ratio of the calorimeter cluster energy to the track momentum : E/P.

(4) The distance between the extrapolated track position and the strip chamber shower position in the ϕ and z views : $R\delta\phi$ and δz.

(5) The shape of the strip chamber shower profile in both views is compared to test-beam electrons with χ^2 variables : χ^2_z and χ^2_ϕ [67]. The χ^2 is defined as

$$\chi^2 = K(E_{CEM}) \cdot \sum_{i=1}^{n} \frac{(q_i^{obs} - q_i^{pred})^2}{(\sigma_i)^2} , \qquad (3.2)$$

where the sum extends over n=11 channels, corresponding to about 15 cm. The q_i^{obs} are the measured channel pulse heights normalized to the total charge in the 11 channels. The q_i^{pred} are the predicted normalized channel depositions based on parametrizations of test-beam strip-chamber data. This χ^2 is minimized using the shower center as a free parameter. The shower position is thus obtained and the minimum χ^2 can be used to test a single electron (or photon) hypothesis. Fluctuations in the single channel pulseheight are taken as $\sigma_i = 0.026 + 0.096 \cdot q_i^{obs}$. An overall energy-dependent normalization $K(E_{CEM})$ is introduced to obtain an energy-independent χ^2. The CES energy resolution is only about 20 % and 30 % for 50 GeV and 10 GeV electrons respectively so it is better to use the energy measured in the CEM for the normalization. Shower fluctuations scale as $1/\sqrt{E}$, but the normalization must take a different form due to non linear response of the CES. The non-linearity arises because the CES is located at a fixed depth ($\sim 5.9 X_0$) in the calorimeter and its sampling of shower energy depends on the electron energy. An energy normalization that compensates for this non linear response $K(E_{CEM}) = 1.792 \cdot 2.11^{Ln(E_{CEM})}$ where the factor 1.792 was chosen so that $K(E_{CEM} = 10GeV) = 10.0$. A typical electron shower has a width of ~ 2 cm and is fully contained in the 11 channel cluster. The χ^2 is useful to discriminate against cases in which more than one particle hits the calorimeter cell containing a shower. Photons from $\pi^0 \rightarrow \gamma\gamma$ decay have an opening distance at the strip chamber depth of $R_{CES} = 184$ cm that relates to the π^0 transverse momentum aproximately as $d \approx \frac{50}{P_T}$ cm. For π^0's above ~ 7 GeV, the two photons will be contained in the cluster. The presence of two photons will be easily identified by a large value of χ^2 for π^0's of up to ~ 20 GeV, above this energy, the closeness of the photons makes it more difficult to separate the two showers. The χ^2 is also useful to discriminate against charged pions. Figure 3.4 shows the distribution of the average strip chamber χ^2 for the W electrons and for test-beam electrons and charged pions, and it is seen that this variable can be used efficiently to select electrons whith high rejection power against charged pions.

Table 3.1 contains the values of the cuts for the variables used for selecting electrons in this analysis. Figures 3.6 to 3.12 show distributions of these variables for electrons from $Z^0 \rightarrow e^+e^-$. Note that we do not base the selection on the amount of extra energy surrounding the electron, that is, we do not make any explicit isolation cuts. The selection cuts imply nevertheless, minimal isolation requirements within the three-tower cell occupied by the electron. Consider for instance the standard cut on the energy sharing variable of $Lshr < 0.2$. The imposition of this cut on a 50 GeV electron hitting the center of a tower, for

which the expected energy in each adjacent tower is ~ 250 MeV, means that no more than 1.4 GeV of excess energy is allowed in the sum of the adjacent towers. Our electron selection allows identifying electrons very near jets (or other particle activity), so long as no extra particles overlap with the electron in its three-tower cell.

Conversion Electrons

After the fiducial and electron selection cuts are applied, electrons from photon conversions and Dalitz decays of π^0's ($\pi^0 \to e^+e^-\gamma$) are removed using an algorithm described in detail in reference [68,69]. We loosely refer to both photon conversions and Dalitz decays as 'conversions'. Photons may convert in the the inner or outer walls of the VTPC and in the inner wall of the CTC, and the e^+e- pair is detected in the CTC. For conversions in or beyond the outer wall of the VTPC, the pair will not be preceded by a VTPC track. Electron candidates without a matching VTPC track or with a second nearby oppositely charged CTC track forming a low e^+e^- effective mass are rejected as photon conversion candidates. The low-mass pair cut also rejects electrons from Dalitz decays. It is considered there is no matching VTPC track if V_{eff}, the ratio of the number of found VTPC hits to the number of expected VTPC hits along the road connecting the event vertex to the electron cluster, is less than 0.2. The cut on effective mass is $M_{e^+e^-} < 0.5$ GeV/c^2. The radius of conversion R_c is taken to be the distance from the origin to the point where the tracks are tangent. Figure 3.2 shows the distribution of R_c for the events tagged as conversions by the effective mass cut. Two clear peaks are present, distinguishing pairs from Dalitz decays and conversions at the VTPC inner wall (at 2.5 cm) from conversion at the outer wall of the VTPC or inner wall of the CTC (at ~ 28 cm).

The VTPC has high track finding efficiency, indicating that electrons without a matching VTPC track provide a very pure sample of outer wall photon conversions. Such a sample is used to determine the number of conversions not identified by the $M_{e^+e^-}$ cut, either because the second CTC track is too soft to be found,

or because the pair mass is outside the cut value. For an inclusive electron sample with $E_T^e > 15$ GeV, it was estimated with this method that the conversion removal algorithm is $\sim 88\%$ efficient and that $\sim 5\%$ of unidentified conversions remain in the sample after the cuts are applied [68,69,70]. An over-efficiency, or fraction of 'good' electrons mistakenly tagged as conversions by the algorithm, of $\sim 5\%$ was estimated by studying like-sign low-mass pairs [68,69,70].

3.3.2 Electron Selection Efficiency

The Method

The efficiency of the electron selection criteria is measured for high P_T electrons by using a sample of $Z^0 \to e^+e^-$. The method consists of selecting a sample of dielectrons in which at least one electron passes the selection criteria. Then, for events with dielectron invariant mass inside a window centered near the Z^0 peak, we look at the second electron and check whether or not it passes the cuts. Let N be the number of events inside the mass window with at least one tight electron, and N^{all}_{pass} the number of events with both electrons passing the tight cuts. The number of 'uncut' or 'unbiased' electrons is $N + N^{all}_{pass}$, since each of the N^{all}_{pass} events contributes two electrons. The efficiency of a given cut i is given by

$$\epsilon^i = \frac{N^i_{pass} - N^{all}_{pass}}{N + N^{all}_{pass}}, \tag{3.3}$$

where N^i_{pass} is the number of events in which both electrons pass the cut i. The statistical error on this efficiency, given by binomial statistics, is

$$\Delta\epsilon^i = \sqrt{\frac{\epsilon^i(1-\epsilon^i)}{N + N^{all}_{pass}}}. \tag{3.4}$$

The overall efficiency and its statistical error are obtained by setting $i = all$ in the above formulas.

The $Z^0 \to e^+e^-$ Sample

We selected $Z^0 \to e^+e^-$ candidates by requiring one tight central electron and a second loose central electron with the following requirements.

(1) One tight central electron.

- The candidate must be inside the CEM fiducial region and pass the electron identification cuts listed in Table 3.1.
- $E_T^e > 20$ GeV

(2) A second loose central electron:

- A CEM cluster with $HAD/EM < 0.125$, and inside the CEM fiducial region.
- $E_T^e > 20$ GeV
- $P_T^e > 10$ GeV/c

(3) An isolation cut requiring that that the transverse energy in the towers within a cone of $R \equiv \sqrt{(\Delta\phi)^2 + (\Delta\eta)^2} = 0.7$, excluding the electron energy, be less than 12 GeV, is applied to both electron candidates. This cut is intended to reject remnant backgrounds from QCD dijet and W + jet events, and does not reject a significant number of Z^0 events, as shall be shown later.

This selection results in a sample of 135 opposite-sign dielectron events. The dielectron invariant mass for these events is shown in figure 3.5 and peaks near the Z^0 mass. The invariant mass is calculated as

$$M_{e^+e^-} = \sqrt{2E_T^{e^+}E_T^{e^-}(\cosh\Delta\eta^{e^+e^-} - \cos\Delta\phi^{e^+e^-})}\,, \qquad (3.5)$$

where $\Delta\eta^{e^+e^-}$ and $\Delta\phi^{e^+e^-}$ are the e^+e^- difference in pseudo-rapidity and in azimuthal angle, respectively, determined using the tracking information. We have not applied calorimeter energy corrections in making this plot. For the CDF measurement of the Z^0 mass [43], corrections for the absolute energy scale of the calorimeter of ~ 1 % and for the tower-to-tower variations in response of ~ 2 % were applied. There are no same-sign events with $M_{ee} > 65$ GeV/c^2 in the sample, indicating that the dielectron sample under the Z^0 peak is very clean, and hence it is ideal for the efficiency study.

Results

We use the events in the mass interval 80-105 GeV/c^2 to perform the efficiency measurement. In this window there are 114 events having at least one electron passing the selection cuts. In 72 of the 114 events, the second electron also passes the selection cuts. This gives an unbiased sample of 186 electrons.

Figures 3.6 to 3.11 show the distributions of the various electron identification variables for the electron sample. figures 3.6, 3.14 and 3.15 show the distributions of EM/HAD, the extra energy in a cone of R=0.7 surrounding the electron, and P_T^e, which were used to select the second electron in the events. It is seen from these distributions that the cuts applied on the second electron are not a significant bias. The results of the efficiency study are summarized in Table 3.2. In this table, N_{pass} is the number of times the second electron passes a given cut, and N_{fail} is the number of times the second electron fails a given cut exclusively. The efficiency of the selection for electrons going into the fiducial region of the calorimeter is

$$\epsilon^e_{iso} = (77 \pm 3)\% \,, \qquad (3.6)$$

where the subindex iso is placed to emphasize that this result was obtained from Z^0 decay electrons which are isolated. The single cuts causing the largest inefficiencies are the χ^2_ϕ cut and the E/P cut. Figure 3.13 shows a scatter plot of χ^2_ϕ versus E/P, and it can be seen that events having large E/P are likely to have large χ^2_ϕ as well. This is consistent with photon bremsstrahlung : the electron emits a photon that separates in azimuth from the bending electron causing a distortion in the strip chamber energy profile in the azimuthal view . At the same time, if the photon is hard enough it will cause a discrepancy between the calorimeter energy and the track momentum.

3.4 MUON SELECTION

In this section we define the variables used to identify muons and give the cut values used. We also present a measurement of the efficiency of the selection

criteria on muons from Z^0 decay.

3.4.1 Muon Selection Criteria

The fine granularity of the CDF calorimeters and the excellent spatial and momentum resolution of the CTC are used to find muons by requiring that the tower to which a track extrapolates has energy deposition consistent with that of a minimum ionizing particle. High P_T muons can be efficiently found in CDF in the rapidity range $|\eta| < 1.2$, that is, in the region covered by the central and endwall calorimeters and by the central tracking chamber. If the track goes into the region $|\eta| < 0.63$ which is instrumented with muon chambers, then a match in azimuth between the CTC track and the muon chamber segment can be used to reject backgrounds. The presence of a muon chamber segment is also useful for online-triggering of muons. If the muon track has no associated muon segment, then it can still be accepted by requiring a loose isolation cut. The isolation cut is necessary to replace the background rejection power inherent in demanding a muon chamber segment. Candidates with and without a muon chamber track are known as CMUOs (central muon objects) and CMIOs (central minimum ionizing objects), respectively.

Fiducial Region

The same fiducial cuts defined for electrons are applied on CMIOs to avoid cracks between calorimeter modules. No explicit fiducial cuts are applied on CMUOs, since the muon chamber geometry is such that tracks going through cracks are avoided naturally. The geometric regions covered by CMUOs and CMIOs are illustrated in figures 3.25 to 3.27 which are scatter plots of η versus ϕ modulo 15° for CMUOs and CMIOs from $Z^0 \to \mu^+\mu^-$ decays. Figures 3.26 and 3.27 show the CMIOs before and after the fiducial cuts. The CMIO region fully contains the CMUO region except for rare cases. If the event vertex is far from $Z = 0$, then a track may be near $Z = 0$ at $R = R_{CES}$ (therefore failing the CMIO fiducial cuts) and nevertheless be further away than 9 cm from $Z = 0$ at $R = R_{CMU}$ and

hit a muon chamber. Another rare exception may occur for a low momentum track that passes near a 15° crack at $R = R_{CES}$ (and fails the CMIO cuts) but is bending into the muon chambers due to the magnetic field. In figure 3.27, the event with ($|\eta| \sim 0.3, \phi \sim 6°$) represents a small inefficiency of the muon chambers: the track goes through the chambers but has no associated stub, and was therefore picked up as a CMIO. The other 2 events near $\eta = 0$ legitimately miss the muon chambers.

Muon Identification Variables

The following requirements are used to select muons:

(1) Minimum ionization requirement. The calorimeter tower to which the CTC track points is required to contain less than 2 GeV of energy in the EM compartment, less than 6 GeV of energy in the hadronic compartment, but more than 0.1 GeV in the sum of the two compartments. Figures 3.19 and 3.20 show the E_{EM}^{tower} and E_{HAD}^{tower} distributions for 57 GeV/c test-beam muons [49]. The average energy depositions are of 0.3 GeV and 2 GeV in EM and hadronic energy respectively. Figure 3.21 [48] shows the distribution for the sum $E_{EM}^{tower} + E_{HAD}^{tower}$ deposited by test-beam 57 GeV/c charged pions. The small minimum ionizing peak corresponds to a mix of charged pions which 'punch through' the calorimeter and muons untagged by the test-beam counter. By using the tagging efficiency of the counter to subtract the muon contamination from the events under the minimum ionizing peak, it was inferred that the non-interactive pion punchthrough probability is (0.7 ± 0.1) %.

(2) For CMUO candidates azimuthal separation at the muon chamber radius between the extrapolated CTC track and the muon chamber track must be of $\delta X_{track-stub} < 10$ cm. This represents a 10(3)σ cut on 15(5) GeV/c muons, since multiple scattering deflects muons exiting the calorimeter by ~ 15 cm/P_T (that is, 85 mR/P_T × the effective length of the calorimeter of 181 cm).

(3) For CMIO candidates the transverse energy in the towers within a cone of $R \equiv \sqrt{(\Delta\phi)^2 + (\Delta\eta)^2} = 0.4$, excluding the muon energy is required to be less than 5 GeV.

(4) Track quality cuts. The CTC track must have an impact parameter (distance to the beamline in the transverse plane) $d_0 < 0.5$ cm and a distance to the primary vertex along the beamline of $|Z_{track} - Z_{vertex}| < 5$ cm. These cuts are placed to reject ocassional tracks which appear isolated due to stereo misreconstruction but which are really coming from the core of a high multiplicity jet. The track quality cuts have an efficiency of (99.6 ± 0.1) % on 'good' tracks. This was determined from a sample of $W \rightarrow e\nu$ events selected by requiring electrons with $E_T^e > 25$ GeV passing the cuts of Table 3.1 and $E_T^{miss} > 25$ GeV. The distributions of the impact parameter and of the of the track-to-vertex distance along the beamline are shown in figures 3.17 and 3.18.

Table 3.2 contains the values of the cuts for the variables used for selecting muons in this analysis.

3.4.2 Muon Selection Efficiency

Similarly to the electron case, the efficiency of the muon selection criteria can be measured for high P_T muons using a sample of $Z^0 \rightarrow \mu^+\mu^-$. The method for obtaining an unbiased lepton sample has been described in section 3.3 for electrons, and is totally analogous in this case.

The $Z^0 \rightarrow \mu^+\mu^-$ sample is selected by requiring one tight muon (CMUO) and a second loose muon (CMUO or CMIO). Events in which both muons are CMIOs are not triggered on (unless the Z^0 has very high P_T and the event comes in with the jet or missing E_T triggers) and are not studied. The following criteria were used to select the $Z^0 \rightarrow \mu^+\mu^-$ sample.

(1) One tight CMUO.

- $P_T^\mu > 20$ GeV/c

- The candidate must satisfy the selection cuts of Table 3.2.

(2) A second loose CMUO or CMIO.

- $P_T^\mu > 20$ GeV/c with track quality requirements.
- Fiducial cuts must be satisfied for CMIO candidates.

(3) An isolation cut requiring that there be no jet with $E_T^{jet} > 15$ GeV centered within a cone of $R \equiv \sqrt{(\Delta\phi)^2 + (\Delta\eta)^2} = 0.4$ about the muon candidates. This isolation cut is intended to remove punch-through backgrounds from QCD dijet and W + jet events.

(4) Cosmic ray backgrounds are removed with a back-to-back cut. Events are tagged as cosmic rays and rejected if $|\eta^{\mu_1} - \eta^{\mu_2}| < 0.1$ and $\phi^{\mu_1} - \phi^{\mu_2} - 180°| < 1.5°$. In addition, a few remaining cosmic rays were removed by scanning (the events had not been recognized as back-to-back because the cosmic ray was not going through the primary vertex and there was a stereo misreconstruction).

A sample of 126 dimuon events comes from this selection. There are no same-sign events in this sample. Figure 3.22 shows the dimuon invariant mass distribution for the sample. Figures 3.23 and 3.24 show the dimuon invariant mass distributions for the CMUO-CMUO and CMUO-CMIO events separately. Events with invariant mass above 70 GeV/c^2 are used for the efficiency study.

There are 49 CMUO-CMUO and 69 CMUO-CMIO events with $M_{\mu^+\mu^-} > 70$ GeV/c^2. In 47 out of the 49 CMUO-CMUO events, the second muon also passes the cuts, so an unbiased sample of 96 CMUOs is available for the efficiency study (since events with the second CMUO passing the cuts contribute 2 muons to the sample). The CMIO sample has 69 events. Figures 3.28 to 3.35 show the distributions of each of the muon identification variables for CMUOs and CMIOs.

The results of the efficiency study are shown in Table 3.2. The CMUO efficiency is (97.9 ± 1.5) % and the CMIO efficiency is (95.7 ± 2.5) %. Since these efficiencies agree within statistical errors, and the source of inefficiency is common and comes from cutting the tail of the Landau distribution for the tower

energy deposition, we take the average and quote a single muon efficiency. After taking the average we also include the efficiency due to the track quality cuts. The resulting muon selection efficiency for muons with either an associated muon track or going into the calorimeter fiducial region is

$$\epsilon^{\mu}_{iso} = (97 \pm 2)\% \tag{3.7}$$

where the subindex *iso* is placed to emphasize that this result was obtained from Z^0 decay muons which are isolated.

3.5 CONCLUSIONS

We have shown how electrons and muons are selected and have proven that triggering and selection efficiencies at high P_T are well understood.

Cut	N_{pass}	N_{fail}	Efficiency (%)
$EM/HAD < 0.05$	108	3	96.8 ± 1.3
$Lshr < 0.2$	110	1	97.8 ± 1.1
$E/P < 1.5$	100	4	92.5 ± 1.9
$R\delta\phi < 1.5$ cm	112	0	98.9 ± 0.8
$\delta z < 3.0$ cm	113	0	99.5 ± 0.5
$\chi^2_\phi < 10$	88	12	86.0 ± 2.5
$\chi^2_z < 10$	104	6	94.6 ± 1.7
All Cuts	72	-	77.4 ± 3.1

Table 3.1: Electron selection cuts and their efficiencies for electrons from $Z^0 \rightarrow e^+e^-$ going into the fiducial region of the calorimeter.

Cut	CMUO Eff. (%)	CMIO Eff. (%)
$E_{EM}^{tower} < 2$ GeV	99.0 ± 1.0	100
$E_{HAD}^{tower} < 6$ GeV	99.0 ± 1.0	95.7 ± 2.5
$E_{EM}^{tower} + E_{HAD}^{tower} > 0.1$ GeV	100	100
$\delta X_{track-stub} < 10$ cm	100	-
$E_T^{R<0.4} - E_T^{tower} < 5$ GeV	-	100
Total	97.9 ± 1.5	95.7 ± 2.5

Table 3.2: Muon selection cuts and their efficiencies from $Z^0 \rightarrow \mu^+\mu^-$ for CMUOs (muons with an associated muon chamber track) and for CMIOs (muons with no associated track going into the fiducial region of the calorimeter).

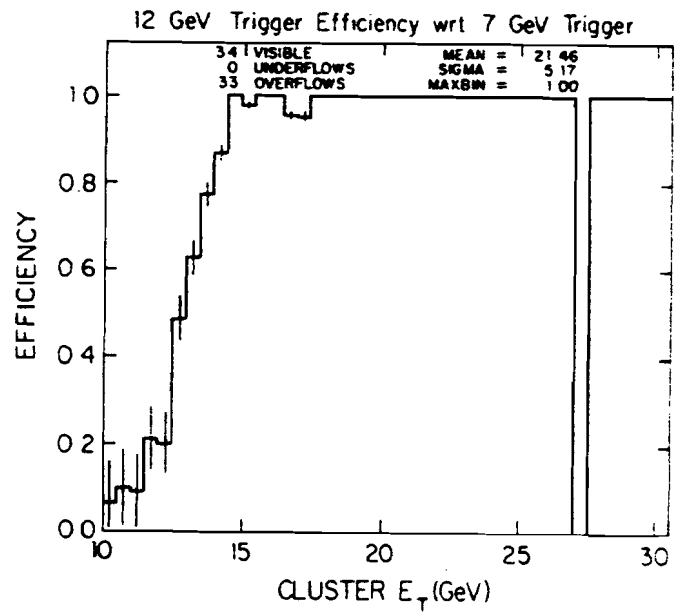

Figure 3.1: The 12 GeV Electron trigger efficiency from 7 GeV Electron trigger data. From reference [59].

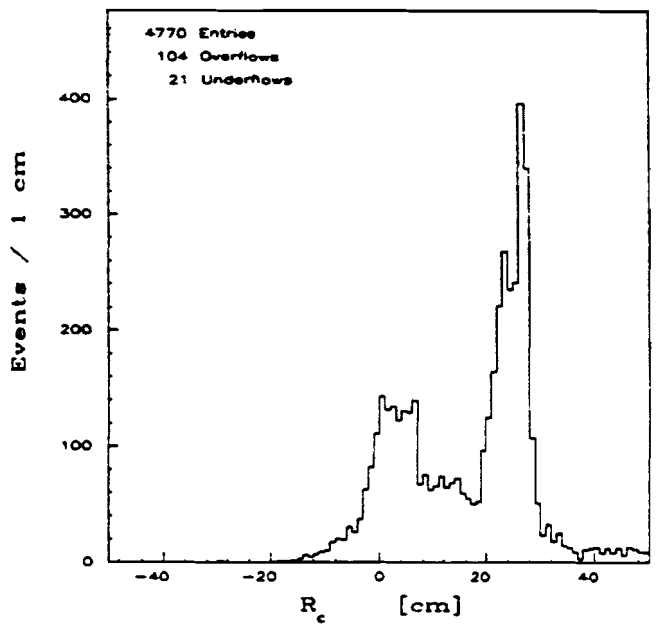

Figure 3.2: The radius of conversion R_e for low mass pairs. Two clear peaks are present, distinguishing pairs from Dalitz decays and conversions at the VTPC inner wall (at 2.5 cm) from pairs from conversions at the outer VTPC wall and inner wall of the CTC (at ~ 28 cm).

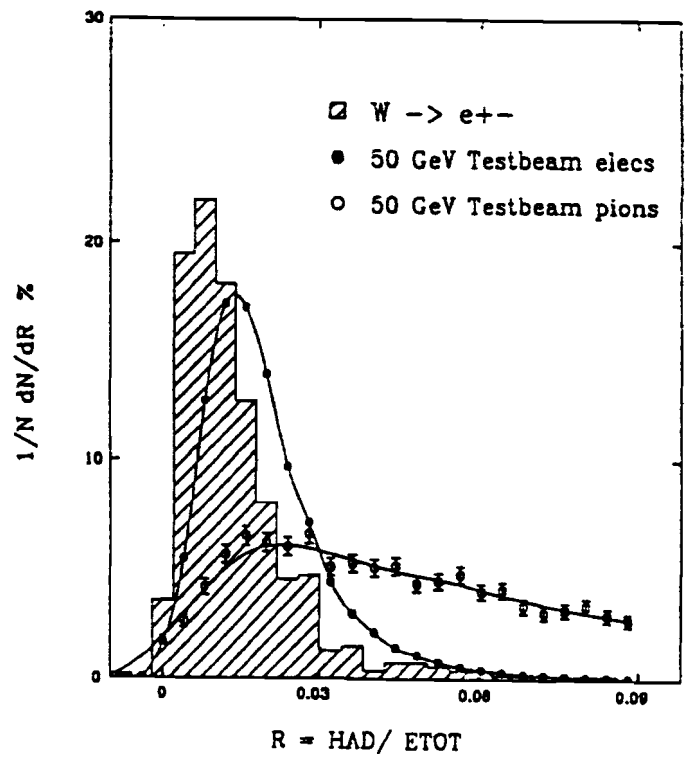

Figure 3.3: The $HAD/(EM - HAD)$ distribution for 50 GeV test-beam electron and charged pion showers and for electrons from $W \rightarrow e\nu$ decays. From reference [66].

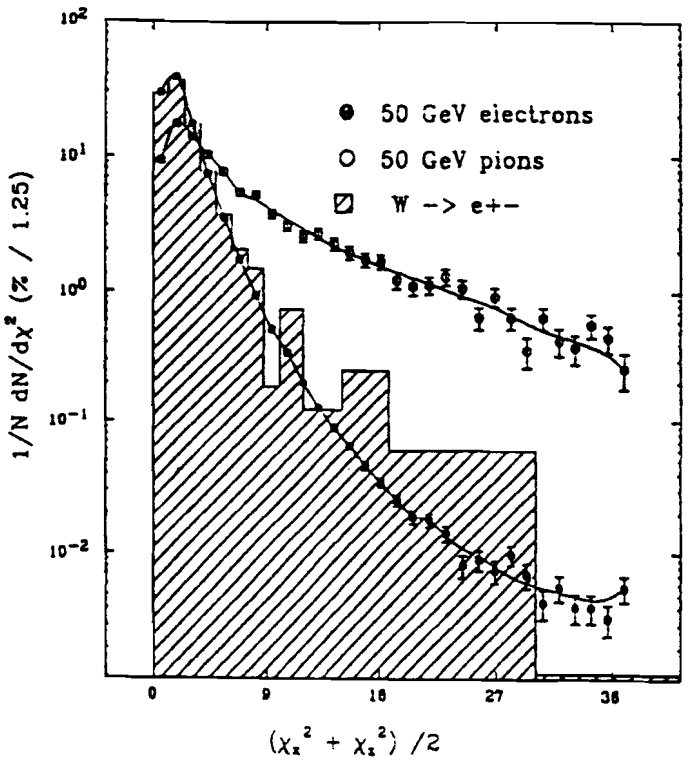

Figure 3.4: The strip chamber χ^2 distribution for 50 GeV test-beam electron and charged pion showers and for electrons from $W \rightarrow e\nu$ decays From reference [66].

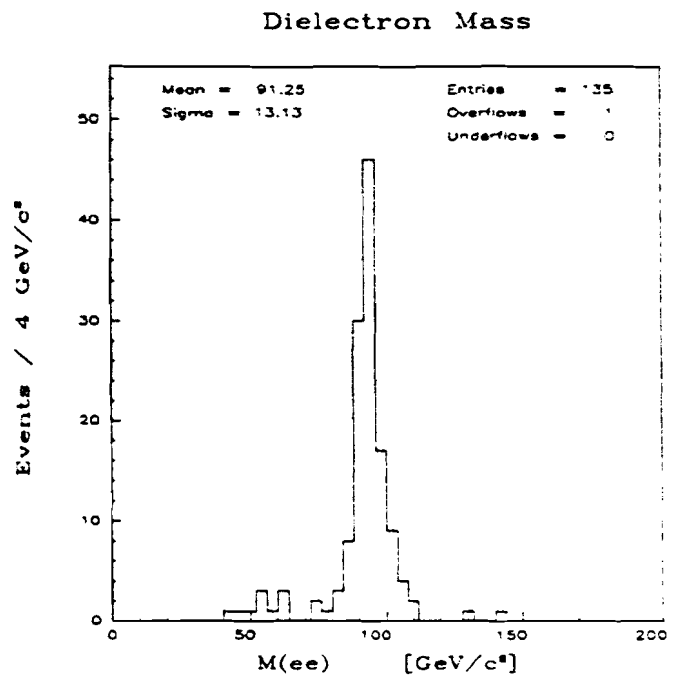

Figure 3.5: The invariant mass ($M_{e^+e^-}$) for the dielectron sample.

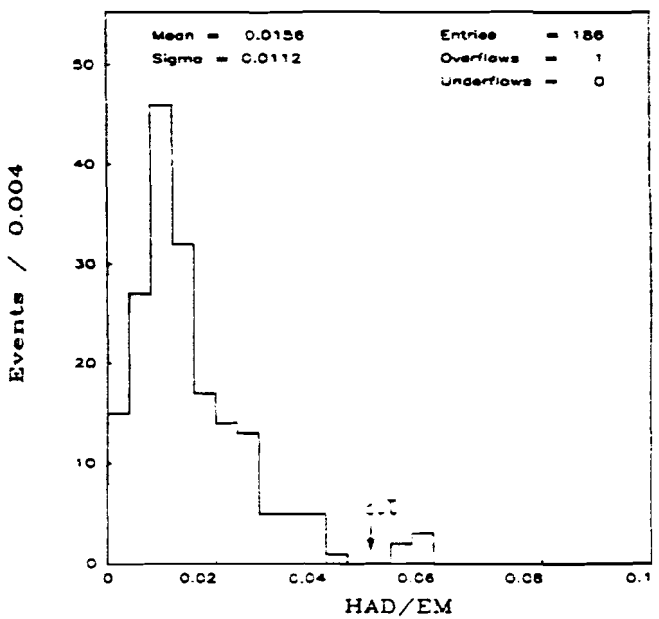

Figure 3.6: The HAD/EM distribution for the $Z^0 \to e^+e^-$ sample.

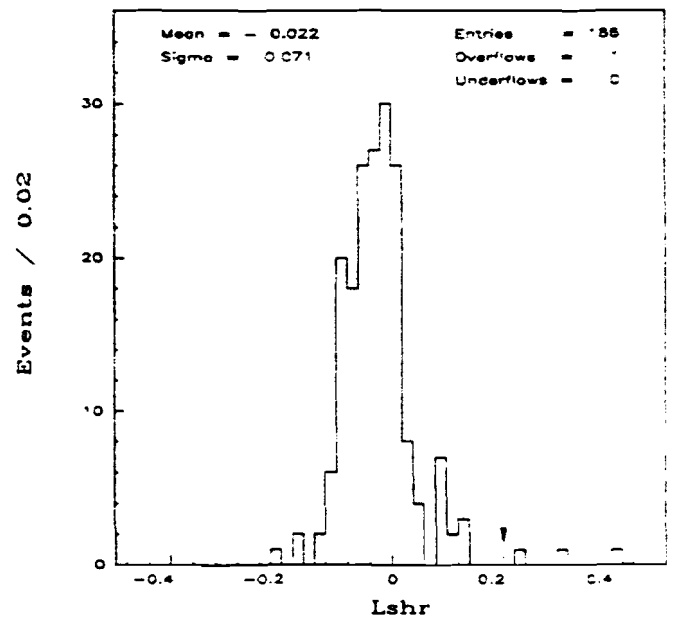

Figure 3.7: The Lateral Sharing ($Lshr$) distribution for the $Z^0 \to e^+e^-$ sample.

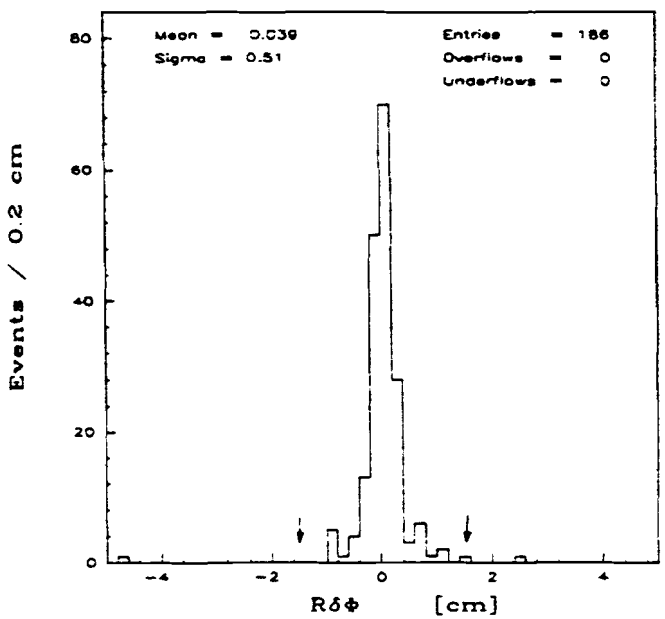

Figure 3.8: The track to strip matching in azimuth ($R\delta\phi$) for the $Z^0 \rightarrow e^+e^-$ sample.

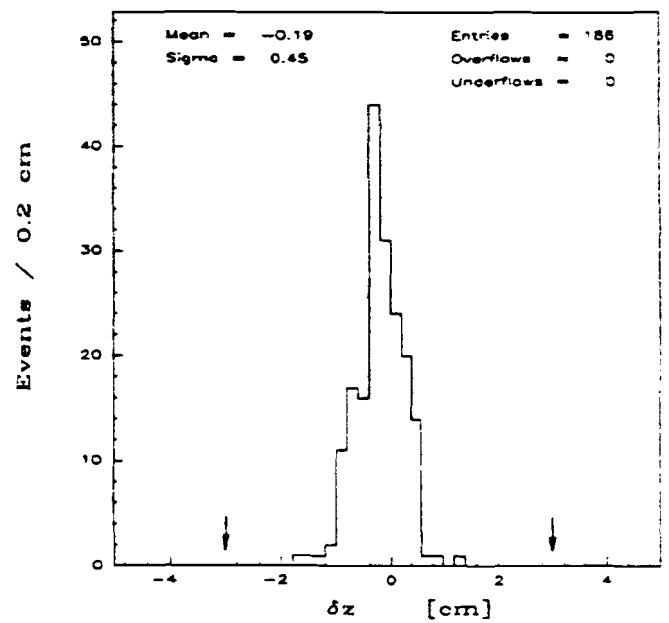

Figure 3.9: The track to strip matching along the beam direction (δz) for the $Z^0 \rightarrow e^+e^-$ sample.

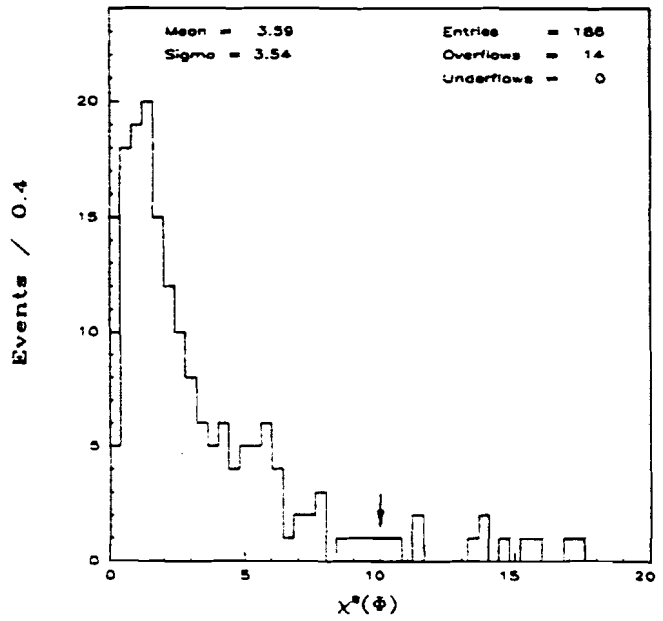

Figure 3.10: The strip chamber χ^2 distribution in the azimuthal view (χ^2_ϕ) for the $Z^0 \to e^+e^-$ sample.

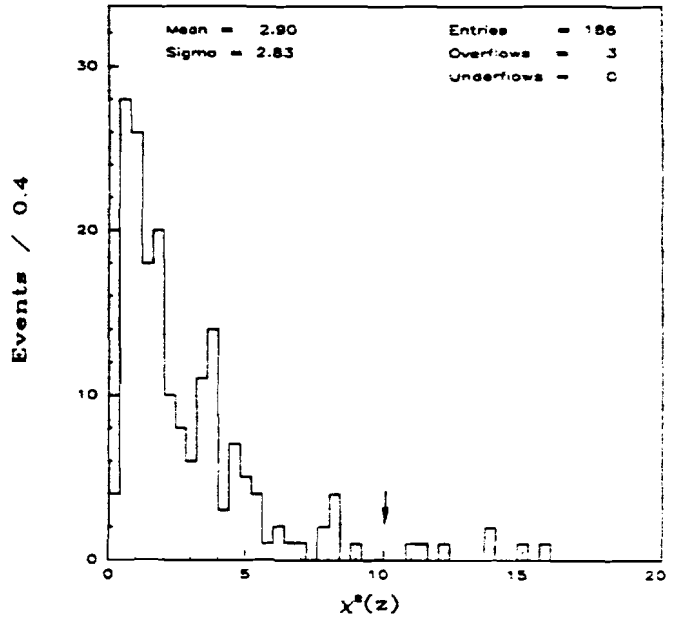

Figure 3.11: The strip chamber χ^2 distribution in the beam direction (χ^2_z) for the $Z^0 \to e^+e^-$ sample.

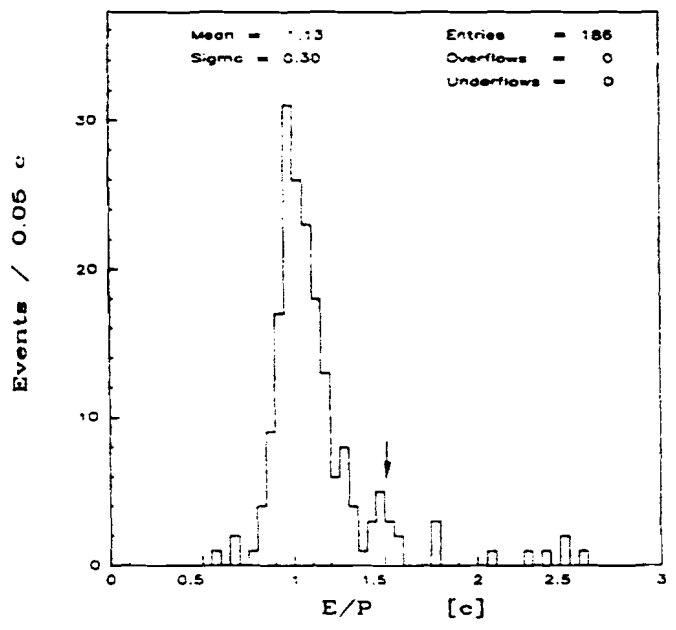

Figure 3.12: The E/P distribution for the $Z^0 \to e^+e^-$ sample.

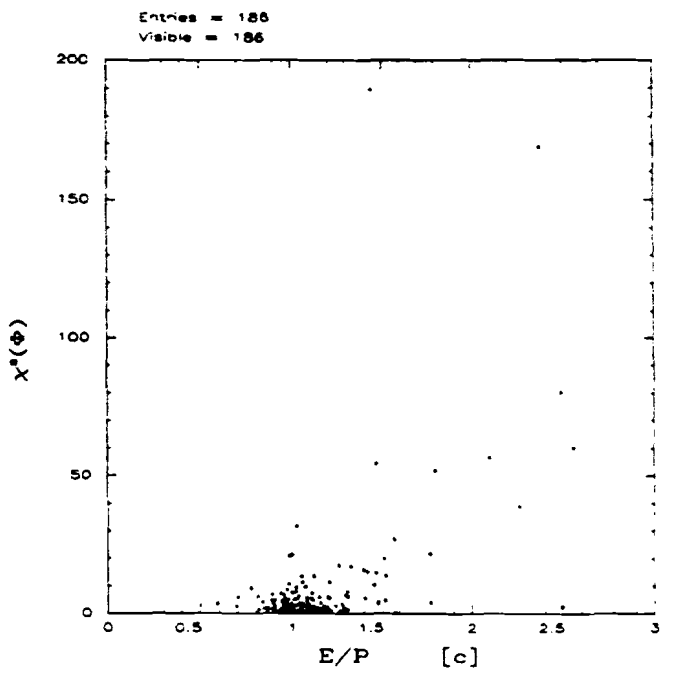

Figure 3.13: The strip chamber χ^2 in the azimuthal view (χ^2_ϕ) versus E/P for the $Z^0 \to e^+e^-$ sample.

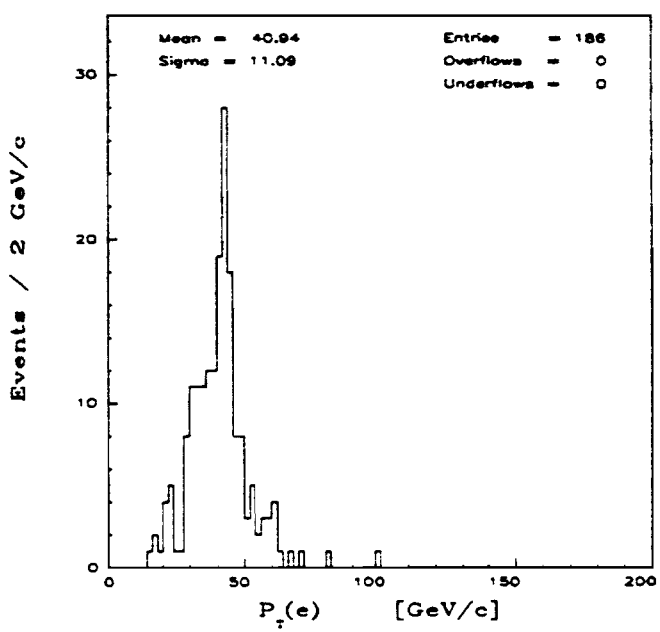

Figure 3.14: The electron track momentum distribution, P_T^e, for the $Z^0 \rightarrow e^+e^-$ sample

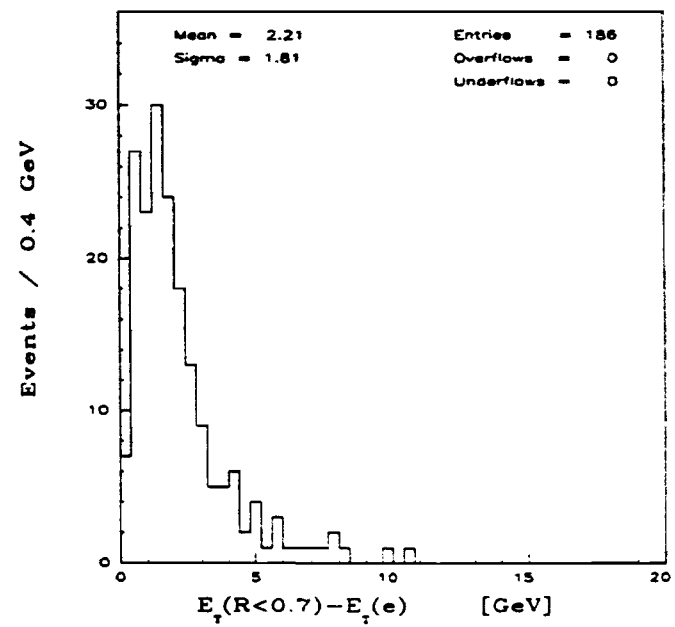

Figure 3.15: The distribution of the transverse energy inside a cone of R=0.7 about the electron, excluding the electron energy , for the $Z^0 \rightarrow e^+e^-$ sample.

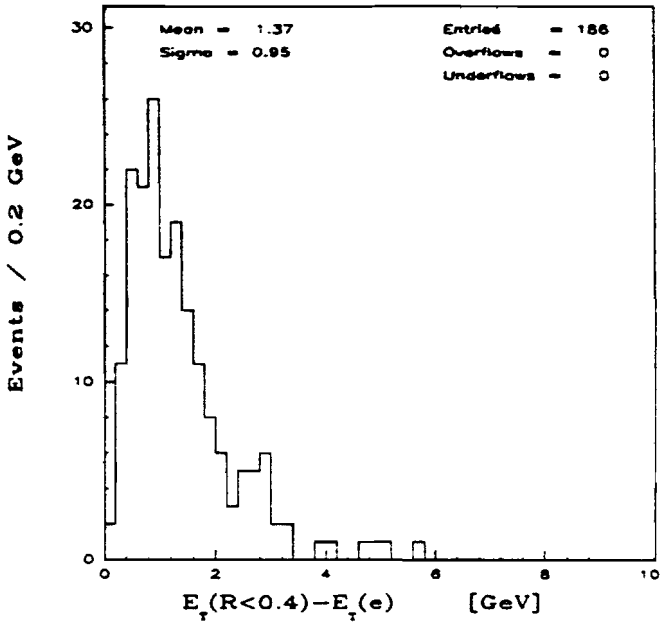

Figure 3.16: The distribution of the transverse energy inside a cone of R=0.4 about the electron, excluding the electron energy, for the $Z^0 \rightarrow e^+e^-$ sample

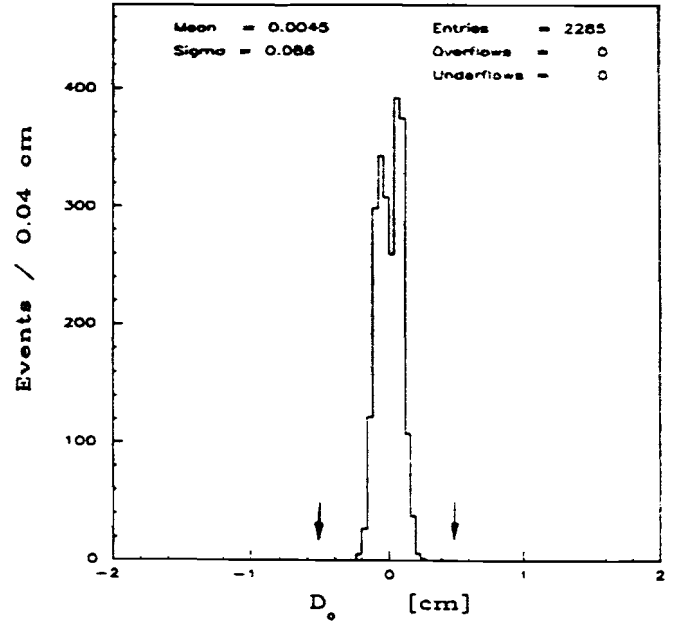

Figure 3.17: The impact parameter (d_0) for electron tracks from a $W \rightarrow e\nu$ sample selected by requiring $E_T^e > 25$ GeV and $E_T^{miss} > 25$ GeV.

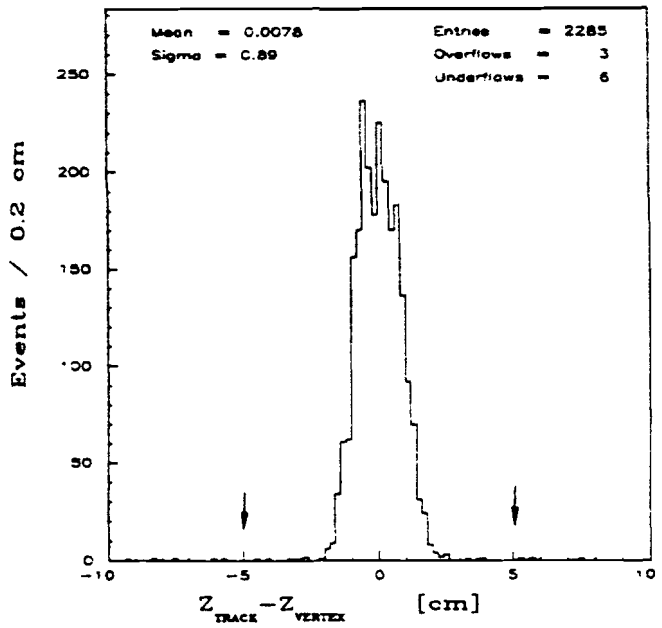

Figure 3.18: The track-to-vertex distance along the bealmine ($Z_{track} - Z_{vertex}$) for tracks from the $W \rightarrow e\nu$ sample.

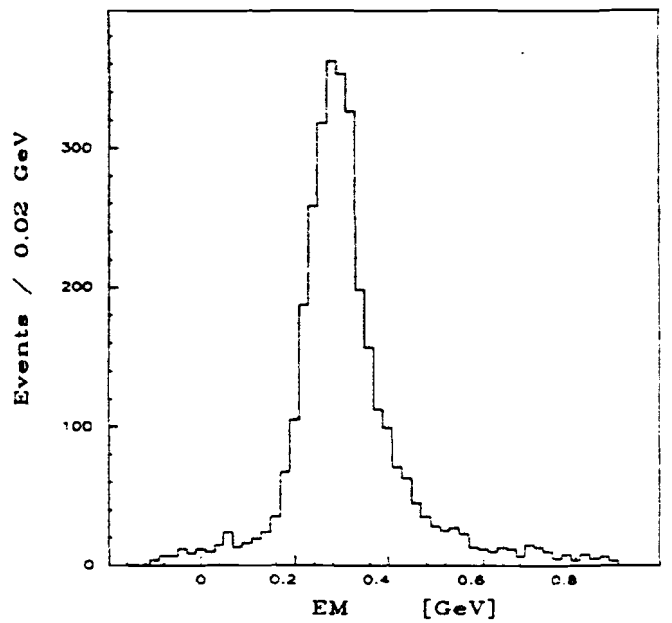

Figure 3.19: Test-beam measurement of the CEM energy deposition (E_{EM}^{tower}) for 57 GeV/c muons. From reference [49].

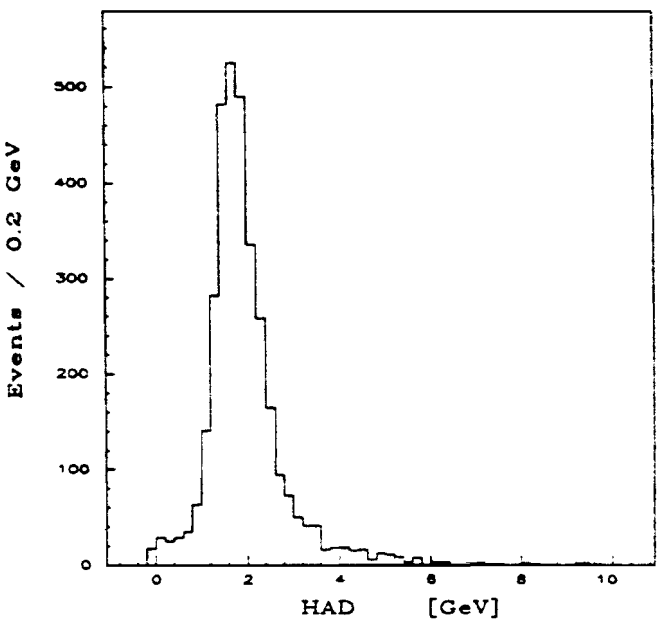

Figure 3.20: Test-beam measurement of the CHA energy deposition (E_{HAD}^{tower}) for 57 GeV/c muons. From reference [49].

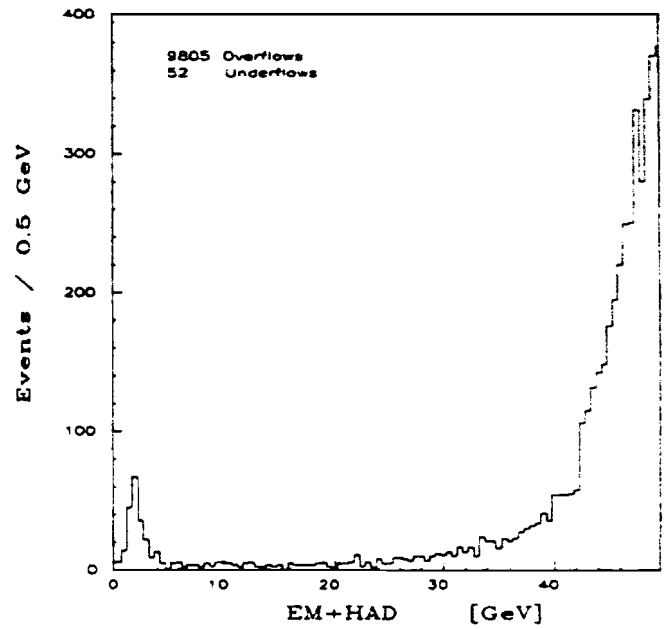

Figure 3.21: Test-beam measurement of $E_{EM}^{tower} - E_{HAD}^{tower}$ for 57 GeV/c π^-'s. The small peak corresponds to minimum ionizing pions and some untagged muons. From reference [48].

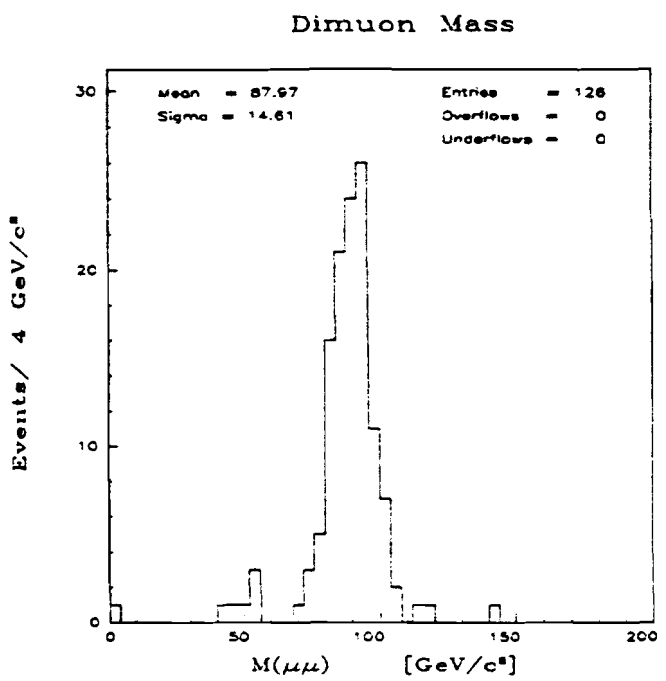

Figure 3.22: The invariant mass ($M_{\mu^+\mu^-}$) distribution for the dimuon sample.

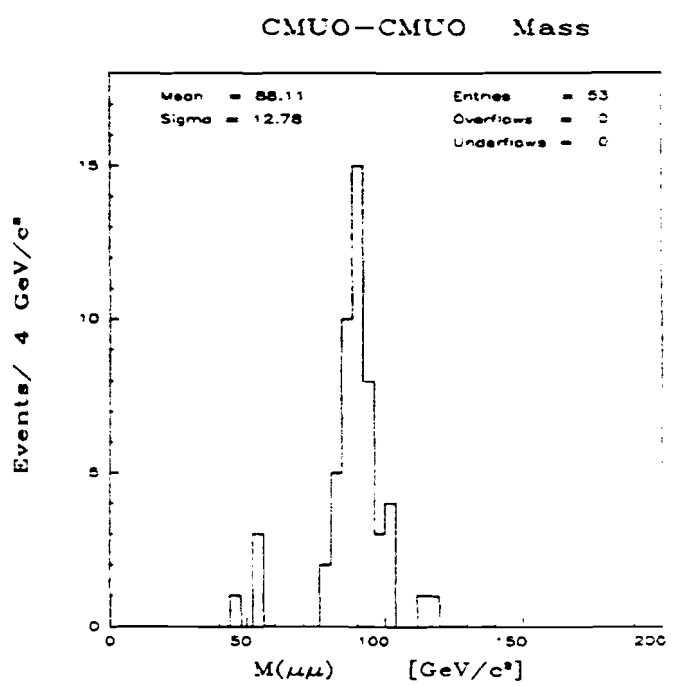

Figure 3.23: The invariant mass ($M_{\mu^+\mu^-}$) distribution for CMUO-CMUO events.

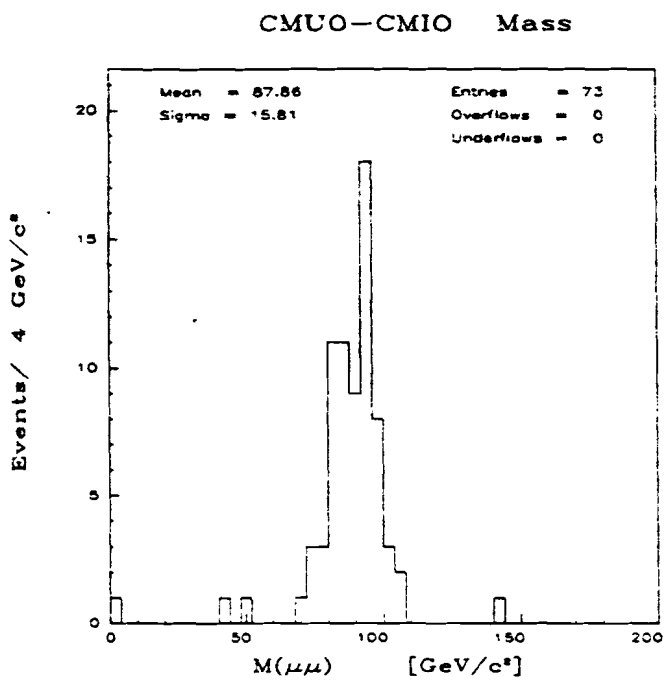

Figure 3.24: The invariant mass ($M_{\mu^+\mu^-}$) distribution for CMUO-CMIO events.

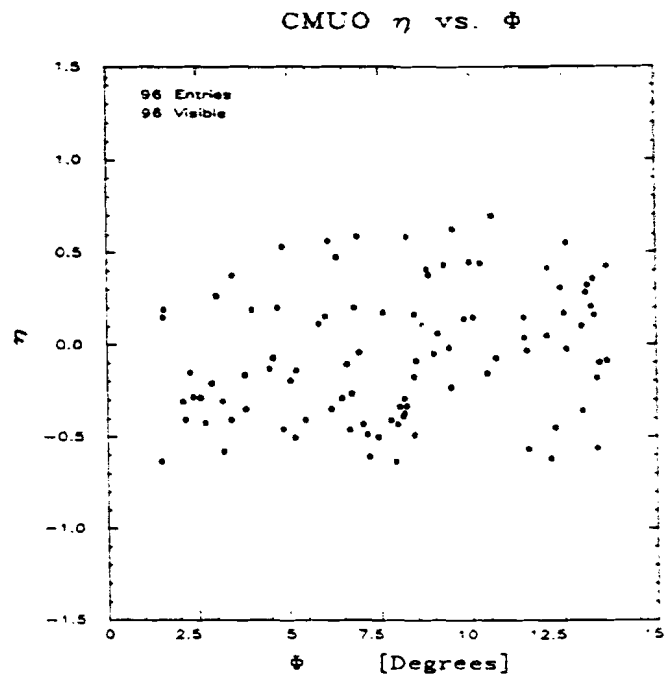

Figure 3.25: Plot of η versus ϕ (modulo 15°) for CMUOs from $Z \to \mu^+\mu^-$. The central muon chamber coverage of $|\eta| < 0.6$ is apparent, as well as the gaps between modules at 0° and 15°

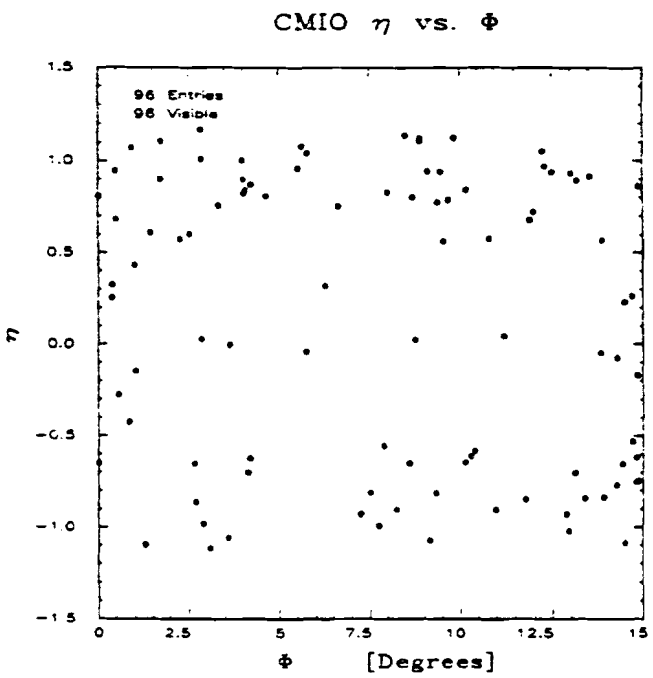

Figure 3.26: Plot of η versus ϕ (modulo 15°) for CMIOs from $Z \rightarrow \mu^+\mu-$ before calorimeter fiducial cuts. The CMIO coverage within $|\eta| < 1.2$ is complementary to the muon chamber coverage illustrated in the previous figure.

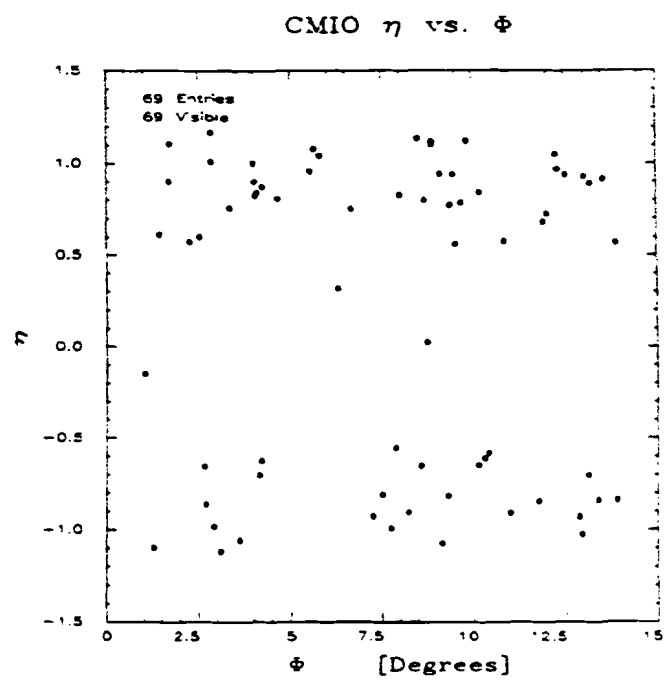

Figure 3.27: Plot of η versus ϕ (modulo 15°) for CMIOs from $Z \rightarrow \mu^+\mu-$ after calorimeter fiducial cuts are applied.

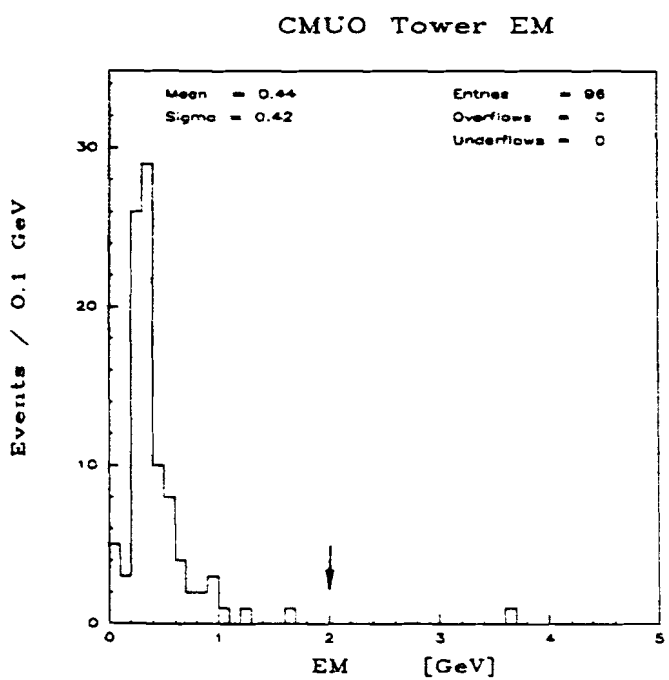

Figure 3.28: The distribution of E_{EM}^{tower} for CMUOs from $Z \rightarrow \mu^+\mu-$.

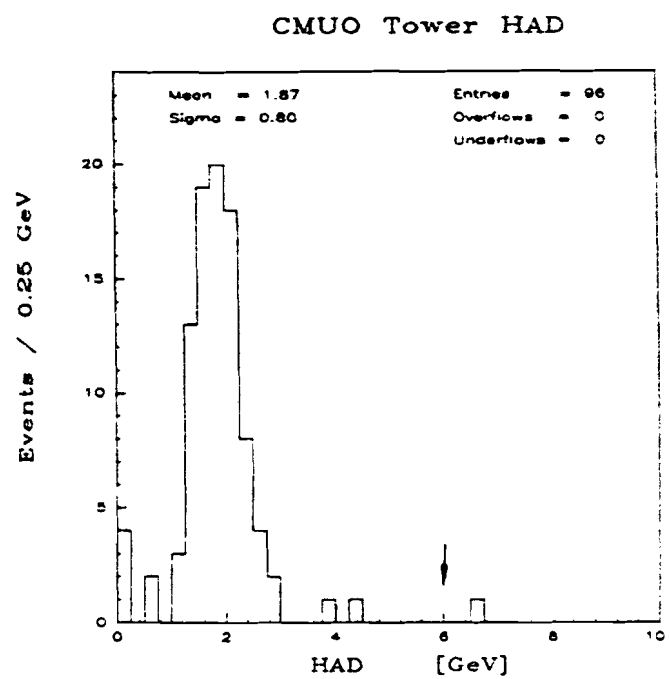

Figure 3.29: The distribution of E_{HAD}^{tower} for CMUOs from $Z \rightarrow \mu^+\mu-$.

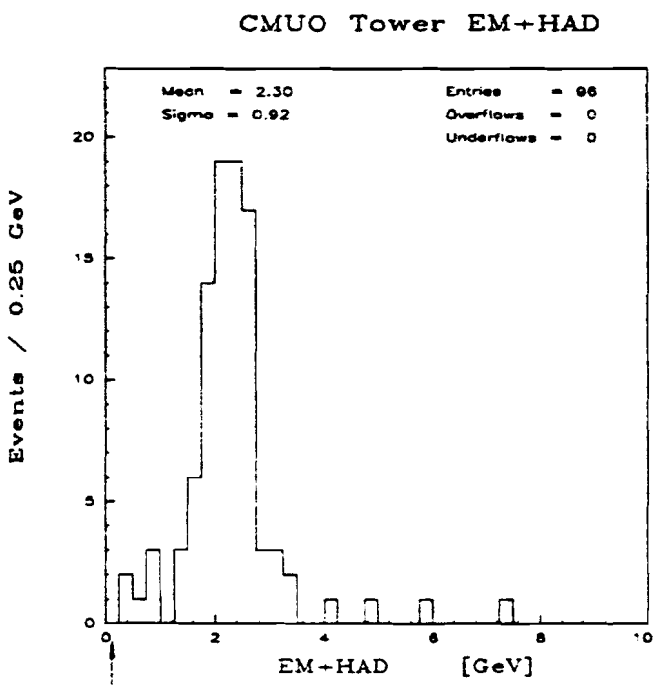

Figure 3.30: The distribution of $E_{EM}^{tower} + E_{HAD}^{tower}$ for CMUOs from $Z \rightarrow \mu^+\mu-$.

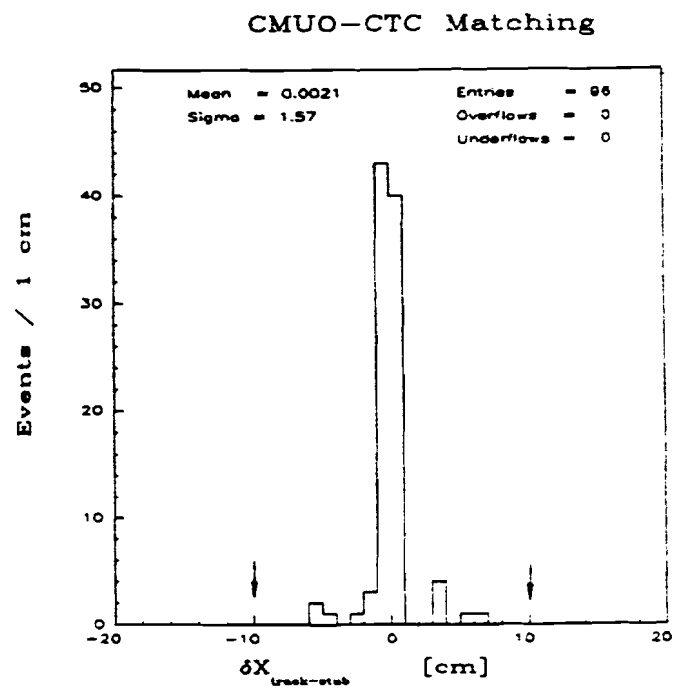

Figure 3.31: The distribution of the azimuthal distance at the muon chamber radius between the extrapolated track and the muon chamber track ($\delta X_{track-stub}$) for CMUOs from $Z \rightarrow \mu^+\mu-$.

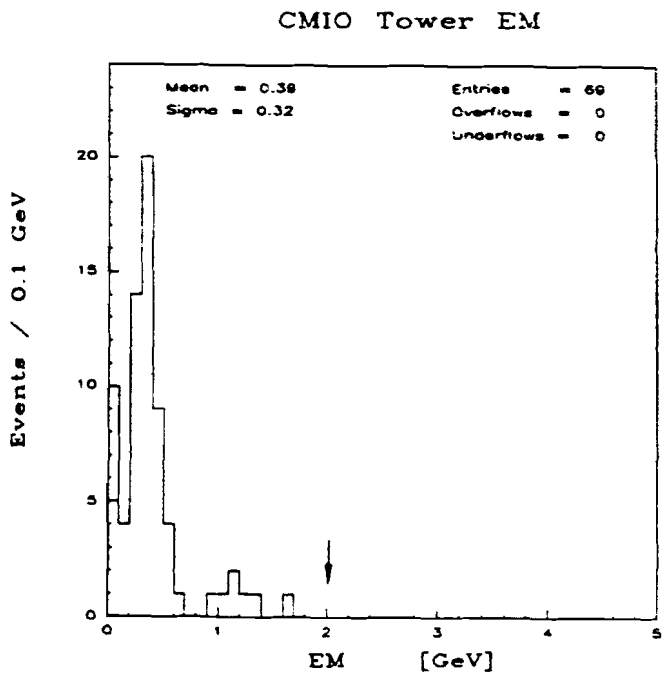

Figure 3.32: The distribution of E_{EM}^{tower} for CMIOs from $Z \rightarrow \mu^+\mu-$.

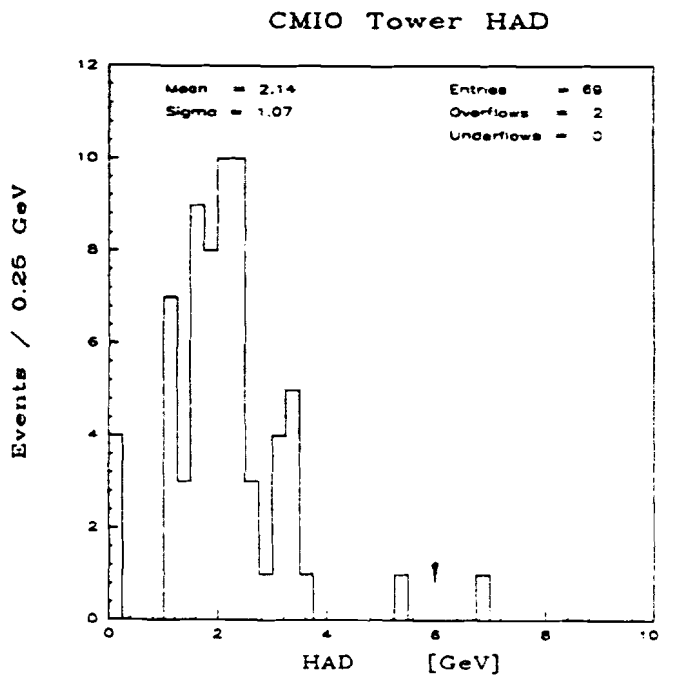

Figure 3.33: The distribution of E_{HAD}^{tower} for CMIOs from $Z \rightarrow \mu^+\mu-$.

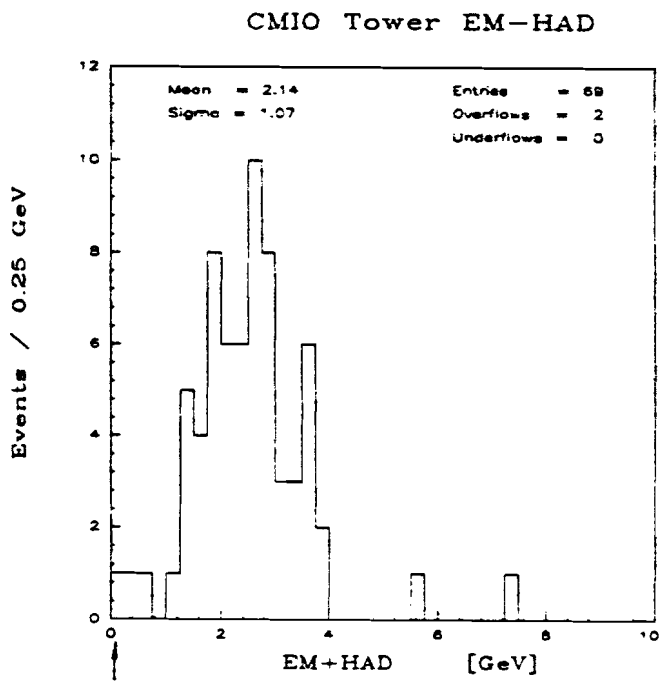

Figure 3.34: The distribution of $E_{EM}^{tower} - E_{HAD}^{tower}$ for CMIOs from $Z \rightarrow \mu^+\mu-$.

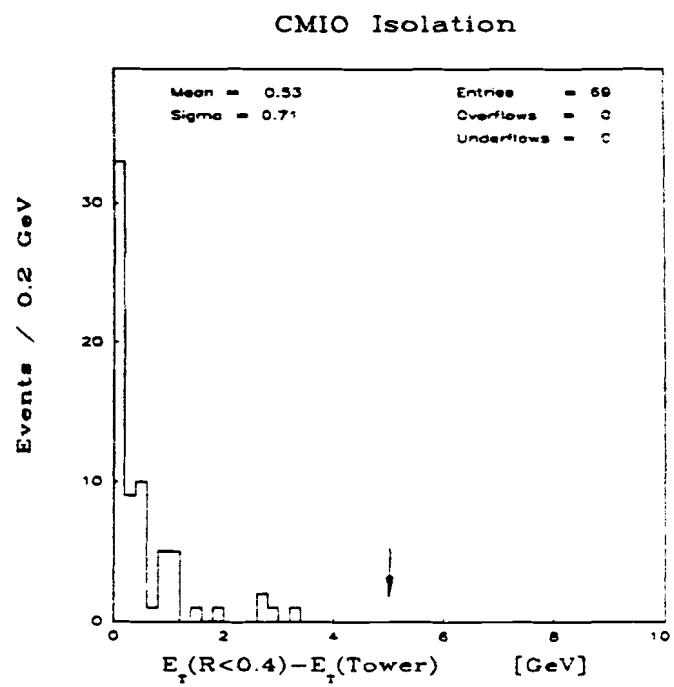

Figure 3.35: The distribution of the transverse energy in the towers within a cone of R=0.4 , excluding the muon energy ($E_T^{R<0.4} - E_T^{tower}$) for CMIOs from $Z \rightarrow \mu^+\mu-$.

Chapter 4

DATA ANALYSIS II : COMPARISON WITH MONTE CARLO

4.1 MONTE CARLO DATA SAMPLES

We have used the ISAJET [71] Monte Carlo program to generate samples of $t\bar{t}$ events (with M_{top}=28, 40, 60, 70, 80, and 90 GeV/c^2), and have then passed the generated data through CDFSIM [72], a full detector simulation program , for comparison with the data and for the determination of acceptances and efficiencies. For special studies to check the top production model in ISAJET, we compared with the PAPAGENO [73] Monte Carlo.

Dilepton backgrounds from QCD production and decay of heavy flavors were simulated with ISALEP [74], the special version of ISAJET that allows generation of bottom and charm pairs produced by higher order diagrams, including flavor excitation and gluon splitting. Since bottom pairs are the dominant source of leptons, we loosely refer to the heavy flavor background as $b\bar{b}$.

Briefly, ISAJET generates events in 4 steps :

(1) Two partons (one from the proton and the other from the anti-proton) are picked with momenta given by a set of structure functions, we used the default parametrization of EHLQ (set I) [75]. The partons are then hard-scattered, according to the elementary QCD cross sections of the process being considered , to obtain the final state partons.

(2) QCD radiative corrections (gluon bremsstrahlung) are added to the initial and final states.

(3) Partons are fragmented into hadrons, and particles are allowed to decay.

(4) Hadrons from the spectator system (beam jets) are added.

The simulation program CDFSIM tracks the particles of the event, one at a time, through the different components of the detector, until they stop by decaying, converting, showering in the calorimetry or exit the detector volume. The result of the simulation program (raw data format) is passed through the same reconstruction program used for real data, and the output (track parameter data-banks, jet banks, lepton candidate banks, etc..) are analyzed in the same way as the real reconstructed data.

4.2 DEFINITION OF THE $t\bar{t} \to e\mu + X$ SIGNAL REGION

The aim in defining a signal region is to choose a portion of phase space with good acceptance for the process of interest and which at the same time is not heavily populated by known backgrounds.

We will distinguish our $t\bar{t}$ signal from the dominant $b\bar{b}$ background by exploiting the marked difference in the lepton spectra. In Figures 4.1 to 4.3 we show the lepton P_T distributions (with a cut of $P_T^l > 5$ GeV/c) for $t\bar{t}$ at M_{top} = 70 GeV/c^2 and 28 GeV/c^2 and for $b\bar{b}$. The parent quark P_T spectra are also shown in these figures, and it is seen that the average top-quark transverse momentum is $\sim M_{top}$. For the $b\bar{b}$ the mean quark P_T is also of the order of the quark mass, which cannot be appreciated in the figure because we generated bottom quarks with $P_T^{bottom} >$ 10 GeV/c and we are sampling the tail of a rapidly falling spectrum. In special runs, we lowered the b-quark momentum threshold and found that 90% of the leptons with $P_T^l > 5$ GeV/c, originate from b quarks with $P_T^{bottom} > 10$ GeV/c, so this cut has a good efficiency for dileptons. The harder parent quark spectra, together with the harder lepton spectrum in the quark rest frame (Chapter 1), gives rise to larger lepton P_T as the mass of the heavy quark increases.

Figures 4.4 to 4.6 show the distribution of $t\bar{t}$ events and $b\bar{b}$ events in the $P_T^\mu - E_T^e$ plane, emphasizing again that the t quark decays generate leptons with large transverse momentum, while the leptons from b quark decay are concentrated at much lower P_T. The top $e\mu$ signal can be well separated from the $b\bar{b} \to e\mu + X$

background by requiring that both E_T^e and P_T^μ be above a common (sufficiently high) transverse momentum threshold. Figure 4.7 shows the expected number of events with $E_T^e > P_T^{min}$ and $P_T^\mu > P_T^{min}$ as a function of the threshold P_T^{min} for simulated $t\bar{t}$ and $b\bar{b}$ (including the higher order contributions) events. It is therefore convenient to select the following signal region :

$$\text{Signal Region} : \begin{cases} E_T^e & > 15 \text{ GeV} \\ P_T^\mu & > 15 \text{ GeV}/c \,. \end{cases} \tag{4.1}$$

It is seen from Figure 4.7 that for the luminosity of the Spin data sample of 4.4 pb^{-1}, 33 events and 7.5 events are expected in the signal region for $M_{top} = 28$ GeV/c^2 and $M_{top} = 70$ GeV/c^2 respectively.

For the $b\bar{b}$ case, the spectrum is steeply falling, and ~ 1 event is expected in the signal region . It must be held in mind that there is large uncertainty in the $b\bar{b}$ cross section (see Chapter 1), but the point is that the signal region threshold is effectively cutting away most of the $b\bar{b}$ background, and due to the sharpness of the spectrum, any surviving events would be near threshold. There are also other variables such as lepton isolation, missing transverse energy and dilepton azimuthal separation, which can be used (but were not needed) to further reject $b\bar{b}$ backgrounds.

4.3 EFFICIENCIES FOR $t\bar{t} \to e\mu + X$

In this section we will determine the efficiencies that relate the observed cross section for $e\mu$ events in the signal region to the total $t\bar{t}$ production cross section :

$$\sigma_{obs}^{e\mu} = \sigma_{t\bar{t}} \cdot Br \cdot \epsilon_{Total}^{e\mu} \tag{4.2}$$

In this expression, the total $e\mu$ detection efficiency $\epsilon_{Total}^{e\mu}$, is normalized to the double semi-leptonic branching ratio $Br = \frac{2}{81}$. We will break up $\epsilon_{Total}^{e\mu}$ into various parts accounting for the geometrical acceptance, the acceptance to the signal region P_T cuts, and the lepton reconstruction efficiencies.

4.3.1 Geometrical and P_T cuts

We define the acceptance due to geometrical and P_T cuts ($\epsilon_{Geom,P_T}^{e\mu}$) as the fraction of $t\bar{t} \to e\mu + X$ events (normalized to the double semi-leptonic branching ratio of $\frac{2}{81}$) with opposite-sign e and μ going into the fiducial volume of the detector and passing the signal region transverse momentum threshold of 15 GeV.

It is to be noted that this definition in principle allows efficiencies larger than 1.0. The double semi-leptonic decay of a $t\bar{t}$ pair (one top quark to $e\nu b$ and the other to $\mu\nu b$) with an assumed branching ratio of $\frac{2}{81}$, contributes most of the signal, but the remaining contributions from sequential decays of a daughter b or c quark or τ lepton are also considered. Hence, the 'effective branching ratio' is larger than $\frac{2}{81}$. In Table 4.1 we show the contributions to the $t\bar{t} \to e\mu + X$ signal from the following sources : i) both leptons come directly from the top decay; ii) at least one lepton is coming from the decay of a τ; and iii) leptons coming from the decays of a b or c quark are involved (but no leptons from τ, since these events are counted in the previous category). These contributions were determined at the generator level, with detector geometry and the signal region transverse momentum cuts. After reconstruction and lepton identification cuts are applied, the small contribution of leptons from b and c quarks will be further supressed since they are less isolated, and less likely to pass implicit isolation cuts such as HAD/EM and $Lshr$, than the first generation leptons from top. It is seen that direct semileptonic decays of both top quarks account for over ~ 80 % of the signal.

For determining $\epsilon_{Geom,P_T}^{e\mu}$, we use the particle momenta at the generator level and impose the detector geometry. Vertex smearing is simulated using a Gaussian with a width of 35 cm, reproducing the real size and shape of the interaction region.

The geometrical cuts used for electrons and muons (CMUOs and CMIOs), representing the fiducial cuts already described in Chapter 3, are the following :

- Electrons must have a Z coordinate at the strip chamber radius (R_{CES} = 184 cm) in the interval 217 cm > $|Z_{R=R_{CES}}|$ > 9 cm, that is, 9 cm away

from the 90° crack and within the outer edge of tower 8 (out to $|\eta| < 1.0$). In addition, the distance at $R = R_{CES}$ to the 15° ϕ boundaries between calorimeter modules is required to be greater than 2.5 cm.

- The CMUO region is defined by the muon chamber geometry (out to $|\eta| < 0.63$). The chambers are located at a radial distance $R_{CMU} = 349$ cm from the beam-line, and the Z coordinate at this radius must be in the interval 235 cm $> |Z_{R=R_{CMU}}| > 9$ cm. In addition, the distance at $R = R_{CMU}$ to the 15° boundaries must be greater than 7.3 cm, to avoid the 2.4° gaps between muon modules. This is the nominal chamber geometry and we have not included edge inefficiencies or the effect of multiple scattering. Events failing to be classified as CMUOs due to such (small) inefficiencies are picked-up as CMIOs anyway so we are justified in ignoring chamber edge effects for purposes of acceptance.

- The CMIO region is defined as having $|\eta| < 1.2$, where η is the pseudo-rapidity in detector coordinates and is determined by extrapolation to the EM calorimeters. The same 90° and 15° crack cuts defined for electrons are used.

The acceptance of geometrical and P_T cuts was determined for two different calculations : ISAJET and PAPAGENO. We find that at high mass, both calculations agree to better than 10 % and we have taken the intermediate value as the acceptance. The associated systematic uncertainty is taken as half the difference in acceptance between the two calculations. Table 4.2 show this acceptance as a function of the top quark mass. At low top mass, the agreement between both calculations is not as good and we estimate a systematic uncertainty of ~ 30 % on the acceptance for $M_{top} = 30$ GeV/c^2. It is also possible to decompose $\epsilon^{e\mu}_{Geom.P_T}$ into two terms; first $\epsilon^{e\mu}_{P_T}$,an acceptance to the P_T cuts (normalized to $\frac{2}{81}$); and second, $\epsilon^{e\mu}_{Geom}$, an acceptance to the fiducial geometry cuts (after the P_T cuts have been imposed).

$$\epsilon^{e\mu}_{Geom.P_T} = \epsilon^{e\mu}_{Geom} \cdot \epsilon^{e\mu}_{P_T} \tag{4.3}$$

The separate geometrical and P_T acceptances are listed in Table 4.5 as a function of top mass and it is seen that the P_T acceptance falls quickly with decreasing top mass and is only ~ 4 % at $M_{top} = 28$ GeV/c^2, giving rise to a large systematic uncertainty.

4.3.2 Electron Reconstruction Efficiency

We now discuss the determination of the efficiency of our electron selection criteria for electrons from top decay with $E_T^e > 15$ GeV that go into the fiducial region of the calorimeter. Discussion of systematic errors due mainly to the uncertainty in the top quark fragmentation will be deferred to Chapter 5. In Chapter 3 we determined the efficiency of the electron cuts for isolated electrons from a $Z^0 \to e^+e^-$ sample. Because the top is heavy, its decay products will be emitted at large angles with respect to its direction. Hence, in general, in the decay $t \to l\nu b$, the lepton will be well separated (isolated) from the decay products of its companion b quark. One way of characterizing the degree of lepton isolation is by measuring the transverse energy inside a cone of radius $R \equiv \sqrt{(\Delta\phi)^2 + (\Delta\eta)^2} = 0.4$, excluding the lepton energy. To set the scale of what an "isolated" electron looks like in terms of this variable, we can see how it is distributed in the $Z^0 \to e^+e^-$ sample in Figure 3.16. This distribution is shown in Figures 4.9 and 4.10 for electrons with $E_T^e > 15$ GeV from top-quarks with masses of $M_{top} = 28$ GeV/c^2, 70 GeV/c^2. Most of the top electrons are in fact isolated, with a tail of less isolated top electrons. For comparison, electrons with $E_T^e > 15$ GeV from $b\bar{b}$ Monte Carlo are shown in Figure 4.11 and it is seen that they are relatively "non-isolated".

Among the non isolated electrons there will be an extra inefficiency from the cases in which extra particles hit the calorimeter cells occupied by the electron. We account for this by decomposing the efficiency for electrons from top into the following terms:

$$\epsilon^e_{top} = \epsilon^e_{iso} \cdot \epsilon^e_{conv} \cdot \epsilon^e_{over} \tag{4.4}$$

The first term is the efficiency for an isolated electron inside the fiducial region of the CEM to pass the electron cuts and was found in Chapter 3 to be $\epsilon^e_{iso} = 0.77 \pm 0.03$. The second term is the inefficiency introduced by the photon conversion cuts which is $\epsilon^e_{conv} = 0.95$. The third term ϵ^e_{over} is the efficiency to "jet overlap", or in other words, it represents the fraction of (non-isolated) events that will fail the electron identification cuts because they overlap with particles from the b jet. In such an overlap case, the calorimetric micro-isolation cuts (inside the three tower cluster) of HAD/EM and $Lshr$ can be failed. We can use the top Monte Carlo to estimate this efficiency due to overlapping particles. For this we take a sample of very isolated top electrons, defined as having $E_T^{R=0.4} - E_T^e < 2$ GeV, and we compare ϵ_{Cal}, the efficiency for surviving the calorimeter HAD/EM and $Lshr$ cuts, for this sample with that for the total sample of electrons. Namely,

$$\epsilon^e_{over} = \frac{\epsilon^{all}_{Cal}}{\epsilon^{iso}_{Cal}} \tag{4.5}$$

Table 4.3 lists ϵ^{all}_{Cal}, ϵ^{iso}_{Cal}, and ϵ^e_{over} for various top masses. Also the total top electron identification efficiency, evaluated using Equation 4.4 is listed as a function of M_{top}. The overall top electron identification efficiency within the fiducial region is $\sim$ 69 % and fairly independent of M_{top}.

4.3.3 Muon Reconstruction Efficiency

We determine the top muon efficiencies in a similar way as we did for electrons. Again, we defer the discussion of systematic uncertainties due manily to the top quark fragmentation to Chapter 5.

The only difference now, is that the analysis isolation cuts cuts are somewhat different for CMIOs than for CMUOs. For both types of object, there is a calorimeter micro-isolation cut requiring that the energy deposition in the tower traversed by the muon be consistent with that of a minimum ionizing particle, namely the $E^{tower}_{EM} < 2$ GeV, $E^{tower}_{HAD} < 6$ GeV, and $E^{tower}_{EM} + E^{tower}_{HAD} > 0.1$ GeV cuts. A further explicit isolation cut is then applied on CMIOs, requiring $E_T^{R<0.4} - E_T^{tower} < 5$ GeV. Given these cuts, we decompose the total efficiency for

muons from top decay into the following terms :

$$\epsilon^\mu_{top} = \epsilon^\mu_{iso} \cdot \epsilon^\mu_{over} \ . \tag{4.6}$$

The first term is the efficiency for an isolated muon (CMUO or CMIO) to pass the muon selection cuts and was determined in Chapter 3 to be $\epsilon^\mu_{iso} = 0.97 \pm 0.02$ from the $Z^0 \to \mu^+\mu^-$ sample. The second term ϵ^μ_{over}, the efficiency to 'jet overlaps', represents loss in efficiency due to non-isolated top muons and is determined using the Monte Carlo to find the fraction of muons that do not fail the tower cuts due to overlapping particles ($\epsilon^\mu_{over\ tower}$), and the fraction of muons that also pass the CMIO cone isolation cut ($\epsilon^{CMIO}_{cone\ cut}$):

$$\epsilon^\mu_{over} = \epsilon^\mu_{over\ tower} \cdot \epsilon^{CMIO}_{cone\ cut} \ . \tag{4.7}$$

Similarly as we did for electrons, the tower efficiency is determined by comparing a sample of very isolated muons (defined as having $E_T^{R<0.4} - E_T^{tower} < 2$ GeV) with the total sample of muons :

$$\epsilon^\mu_{over\ tower} = \frac{\epsilon^{all}_{Cal}}{\epsilon^{iso}_{Cal}} \ . \tag{4.8}$$

Table 4.4 shows the total efficiency for top muons , where we have required the muon to have $P_T > 15$ GeV/c and to go into the fiducial region, as a function of top mass. The table also lists various terms entering the determination of ϵ^μ_{top}.

4.3.4 The total $t\bar{t} \to e\mu + X$ efficiency

We have already shown the determination of the various terms entering the the detection efficiency $\epsilon^{e\mu}_{Total}$ for $t\bar{t} \to e\mu + X$ in the signal region. We define $\epsilon^{e\mu}_{Rec}$ to be the combined $e\mu$ selection efficiency , that is

$$\epsilon^{e\mu}_{Rec} = \epsilon^e_{top} \cdot \epsilon^\mu_{top} \ . \tag{4.9}$$

The total $e\mu$ detection efficiency is then

$$\epsilon^{e\mu}_{Total} = \epsilon^{e\mu}_{Trig} \cdot \epsilon^{e\mu}_{P_T} \cdot \epsilon^{e\mu}_{Geom} \cdot \epsilon^{e\mu}_{Rec} \ . \tag{4.10}$$

In order for an event in the $t\bar{t} \to e\mu + X$ signal region to fail the trigger, it must fail the 12 GeV electron trigger (as seen earlier this has a probability of about 2 %), the $e\mu$ or 9 GeV Muon trigger, the 25 GeV Missing E_T trigger, 60 GeV Jet trigger , 120 GeV Total E_T trigger etc.. About half the $t\bar{t} \to e\mu + X$ events will have a Muon trigger. An important fraction (depending on M_{top})of the events will also have a Missing E_T trigger due to the presence of neutrinos and muon (muons appear as missing energy to the calorimetry). It is reasonable to assume that the probability of failing all these triggers simultaneously is about 1 % or less, and we estimate the trigger efficiency for $t\bar{t} \to e\mu + X$ in the signal region to be

$$\epsilon^{e\mu}_{Trig} = (99.0 \pm 0.5)\% \ . \tag{4.11}$$

Table 4.5 lists the other terms of Equation 4.10 as a function of M_{top}, and the results are plotted in Figure 4.8. The total $t\bar{t} \to e\mu + X$ detection efficiency is 0.6 % and 12 % at M_{top} = 28 GeV/c^2 and 70 GeV/c^2, respectively. Or in other words, including the branching ratio, 0.02% and 0.3% of the total $t\bar{t}$ cross section is detected in the $e\mu$ channel for M_{top} = 28 GeV/c^2 and 70 GeV/c^2, respectively.

4.4 THE DATA

The data shown in this section correspond to an integrated luminosity of 4.4 pb^{-1} processed by an expressline or Spin Cycle (Chapter 3). From this output stream, all events containing at least one electron with $E_T^e > 15$ GeV passing the electron selection cuts of table 3.1 were kept. As was seen earlier, this choice of E_T^e threshold ensures high (~ 98 %) trigger efficiency for electrons. A sample of 17646 events with electron candidate is obtained. Then the photon conversion cuts (Chapter 3) were applied, removing 5144 events. The electron E_T^e spectrum of the resulting sample of 12502 events is shown in Figure 4.12.

Backgrounds to the inclusive electron sample come primarily from photon conversions and from charged pions depositing most of their energy in the EM calorimeter. As seen earlier, the unidentified conversion background is estimated to be 5%. The charged pion background was estimated by studying the uncut

HAD/EM distribution of the inclusive electron sample after all other cuts are applied. The efficiency to the $HAD/EM < 0.05$ cut is known to be 57% for test-beam pions (Figure 3.3) and 95% for non-isolated electrons from a conversion sample. This information together with the numbers of events passing and failing the HAD/EM cut is sufficient to estimate the number of electrons and pions in the sample. With this method, a charged pion background of ~ 20% is inferred [70].

The inclusive electron spectrum has a shoulder near E_T^e = 40 GeV, corresponding mostly to electrons from W and Z decay. Electrons in the falling component of the spectrum below the W region are believed to arise predominantly from semileptonic decays of b quarks. The shape of the spectrum and the isolation properties of electrons with $E_T^e \lesssim 20$ GeV are in good agreement with ISAJET [5] and most remarkably, there is a signal of D^0 charm mesons accompanying the electron [76]. D^0s from $\bar{B} \to D^0 e^- \nu$ are expected in (68 ± 15)% of the semileptonic B-meson decays [77]. The decay $D^0 \to K^- \pi^+$ occurs (3.8 ± 0.4)% of the time [35], and is searched for by reconstructing the invariant mass of oppositely-charged track pairs inside a cone of R=0.6 about the electron. The charge of the electron in the decay determines the charge of the kaon (e^+K^+ or e^-K^-) and this is used to assign a mass (kaon or pion) to each track. The invariant mass of $K\pi$ system shown in Figure 4.13, reveals an unambiguous D^0 signal near its mass of 1864.7 ± 0.6 MeV/c^2 [35]. As expected, no such peak is obtained when the kaon mass is assigned to the 'wrong' sign track. The rate of signal events is consistent, within uncertainties, with the hypothesis that $B\bar{B}X \to eX'$ is the dominant source of electrons.

After the electron selection, the muon cuts of Table 3.2 are applied with a threshold P_T^μ >5 GeV/c if the candidate has an associated muon chamber track (CMUO), and P_T^μ >10 GeV/c if not (CMIO). Although our signal region is P_T^{muon} >15 GeV/c, we have kept low thresholds for the muon to be able to 'see' some of the background. The higher CMIO threshold was picked to reject fake-muon backgrounds. In summary, the analysis thresholds used to select $e\mu$ events (from the Spin output stream) for the top search are :

$$\text{Spin Sample Thresholds} \begin{cases} E_T^e & > 15 \text{ GeV} \\ P_T^\mu & > 5 \text{ GeV}/c \quad \text{if CMUO} \\ & \text{or} \\ & > 10 \text{ GeV}/c \quad \text{if CMIO}. \end{cases} \tag{4.12}$$

The electron and muon selection give a total of 41 opposite-sign $e\mu$ events. Figure 4.14 shows the scatter plot of E_T^e vs. P_T^μ for these events. Similar plots are found in figures 4.15 and 4.16 for 28 and 70 GeV/c^2 $t\bar{t}$ for integrated luminosities of 3 and 80 pb^{-1}, respectively. There is only one event in the signal region, where 33 and 7.5 events are expected from 28 and 70 GeV/c^2 $t\bar{t}$ respectively.

In Figures 4.17 to 4.19 we compare the distribution of P_T^{min} (the smallest of E_T^e and P_T^μ) versus $\Delta\phi_{e\mu}$ (the dilepton azimuthal separation) for the data and the $t\bar{t}$ Monte Carlo samples. The CDF data are concentrated at low P_T^{min} and are clustered near the 0° (colinear) and 180° (back-to-back) regions in $\Delta\phi_{e\mu}$. We will see in the next section that this angular distribution is characteristic of $b\bar{b}$. The candidate event is well separated from the bulk of the data. For the $t\bar{t}$ Monte Carlo, the events have larger P_T, and a more uniform $\Delta\phi_{e\mu}$ distribution which gets flatter as M_{top} increases. The latter is because the decay products of a heavy top are emitted at large angles, so the lepton direction is only weakly correlated with the parent quark direction.

The event in the signal region has an isolated electron with E_T^e of 31.7 GeV and an isolated opposite sign muon with P_T^μ of 42.5 GeV/c with a dilepton azimuthal opening angle of 137°. Other characteristics of the event include the presence of a second muon candidate with a transverse momentum of 9.9 GeV/c in the forward muon detector, and two small calorimeter clusters with transverse energy depositions of 14 GeV and 5 GeV. Figures 4.20 and 4.21 show a CTC display and a calorimetry display for the candidate. Table 4.7 summarizes some of the properties of the event.

The lepton isolation and the missing E_T distributions for the CDF data are

also different from those for $t\bar{t}$. As isolation variable we use :

$$Iso = \frac{E_T^{R<0.7} - E_T^e}{E_T^e}, \tag{4.13}$$

with an analogous definition for muons. Figures 4.22 to 4.24 show the distribution of electron isolation for the CDF data and the $t\bar{t}$ Monte Carlo. The leptons in CDF data are predominantly non-isolated, whereas they are quite isolated for $t\bar{t}$ Monte Carlo.

Our definition of missing E_T is :

$$\overrightarrow{E_T^{miss}} = \left[-\left(\sum_i E_{T_i} \cos\phi_i\right) + P_T^\mu \cos\phi_\mu\right]\hat{x} + \left[-\left(\sum_i E_{T_i} \sin\phi_i\right) - P_T^\mu \sin\phi_\mu\right]\hat{y} \tag{4.14}$$

$$E_T^{miss} = |\overrightarrow{E_T^{miss}}|, \tag{4.15}$$

where E_{T_i} is the transverse energy deposited in tower i of the calorimeter and ϕ_i its azimuthal coordinate. We have corrected for the muon momentum, which is unseen by the calorimeter, but do not correct for the energy deposited by the muon in its tower. Figures 4.25 to 4.27 show the E_T^{miss} distribution for the CDF data and the $t\bar{t}$ Monte Carlo. The missing E_T becomes very different from the data only for the higher mass top.

So far we have only presented opposite-sign data. Same-sign events are expected from sequential decays of heavy flavors. The number of $t\bar{t}$ same-sign events with $P_T^{min} > 15$ GeV/c is less than $\sim 5\%$ of the opposite-sign events in this region; same-sign events are not included as part of the signal. For completeness, in Figures 4.28 and 4.29, we show the E_T^e versus P_T^μ and the P_T^{min} versus $\Delta\phi_{e\mu}$ plots for the same-sign data of our sample. There are 22 same-sign events in the sample. We note that the $\Delta\phi_{e\mu}$ distribution has no peak near 0° (the opposite-sign data has), and postpone the discussion and comparison with the $b\bar{b}$ expectation for the next section. It is interesting to note that there are 2 same-sign events with $P_T^{min} > 15$GeV/c. One of them, with $E_T^e = 79$ GeV and P_T^μ=16 GeV/c, has an isolated electron with a non-isolated muon candidate, and can be interpreted as a $W \to e\nu$, produced at high P_T, with a jet punching through. The other, with $E_T^e = 23$ GeV and P_T^μ=19 GeV/c has a fairly isolated muon with a

back-to-back nonisolated electron, and can be interpreted as a $b\bar{b}$ event with one misidentified lepton, or as a dijet event (both leptons fake). The fact that these same-sign events are present, implies that for future higher luminosity samples we may expect some non-isolated, easy-to-remove background in the signal region.

4.5 COMPARISON WITH $b\bar{b}$ BACKGROUND MONTE CARLO

In this section we show data with an integrated luminosity of 1.8 pb^{-1} processed by the Production inclusive muon output stream. The cuts imposed by this filter for $e\mu$ triggers were simply $P_T^\mu > 4$ GeV/c and $\delta X_{track-stub} < 10$ cm, so it is useful for studying low P_T $e\mu$ events.

At low P_T the CMIO requirements are not strong enough to ensure a clean sample, so we only considered CMUOs for this sample. The cuts of Tables 3.1 and 3.2 were applied on electrons and muons, with the following thresholds :

$$\text{Production Sample Thresholds} \quad \begin{cases} E_T^e & > 5 \text{ GeV} \\ P_T^\mu & > 5 \text{ GeV}/c \quad \text{and CMUO only .} \end{cases} \tag{4.16}$$

We also applied the standard photon conversion rejection cuts (Chapter 3). The resulting sample has $N_{opp} = 269$ opposite-sign and $N_{same} = 148$ same-sign events. The distribution of these events in the $P_T^\mu - E_T^e$ plane is shown in Figure 4.30.

We will be comparing with the CDF data with an ISALEP $b\bar{b}$ Monte Carlo sample with an integrated luminosity of 0.64 pb^{-1}. The Monte Carlo sample has $N_{opp} = 259$ and $N_{same} = 40$, and their distribution in the P_T^μ-E_T^e plane is shown in Figure 4.31.

When comparing rates we note : (1) the Monte Carlo rate for $N_{opp} - N_{same}$ is a factor of 2 higher than for the CDF data (467 pb vs. 232 pb), and (2) there are comparatively much fewer same-sign events in the Monte Carlo, (N_{same}/N_{opp} of 0.15 vs. 0.55). Full comparison of $b\bar{b}$ Monte Carlo and data goes beyond the scope of this thesis and is not yet complete. However we comment that (1) there is a

large theoretical uncertainty in the $b\bar{b}$ cross section, (2) the Monte Carlo has no $b\bar{b}$ mixing (this would enhance the same-sign sample), (3) we have not subtracted fake lepton backgrounds , (4) we do not know the efficiencies (trigger, selection) well enough for these low P_T leptons.

Despite the problems and limitations listed above, it is still instructive to look some more into the low P_T data. A first question is whether or not the sample is enriched in electrons and muons. Figures 4.32 and 4.33 show the electron variables for the CDF data, which can be compared with those for the Monte Carlo in Figures 4.34 and 4.35. Similarly, Figures 4.36 and 4.37 show the muon identification variables for the CDF data and the Monte Carlo respectively. There is fairly good agreement for most of the distributions, indicating a high content of electrons and muons in the CDF data.

Next we show a comparison of some distributions that suggest that in fact we are observing QCD heavy flavor production. The missing E_T distribution is shown for the data in Figure 4.38 and for the Monte Carlo in Figure 4.39. The distribution of the electron isolation variable $Iso = (E_T^{R<0.7} - E_T^e)/E_T^e$ is shown for data and for Monte Carlo in Figures 4.40 and 4.41 respectively. There is good agreement in both of these variables.

A more revealing distribution is that of the azimuthal separation between the electron and muon, $\Delta\phi_{e\mu}$. First we look at this variable at the generation level. Figure 4.42 shows $\Delta\phi_{e\mu}$ for both same-sign and opposite-sign events for Monte Carlo events generated with $P_T^{min} > 5$ GeV/c $|\eta^e| < 1.0$, and $|\eta^\mu| < 0.6$ to reflect the geometry of the detector. The contributions of directly produced $c\bar{c}$ and the sum $b\bar{b} + c\bar{c}$ are shown separately, together with the total which also includes the higher order processes of flavor excitation and gluon splitting. All histograms are normalize to the total number of events $N_{same} - N_{opp}$. One important observation is that there is a peak near $\Delta\phi_{e\mu} = 0°$ only for the opposite-sign sample. This peak is built up mostly of two sources of similar magnitude : (1) cascade decays from the direct $b\bar{b}$ events ($b \to cl_1\nu$ with the subsequent $c \to l_2 s\nu$ decay), and (2) higher order contributions, predominantly from gluon splitting ($g \to b\bar{b}$, with a semileptonic decay of each b or cascade decay of one b). Similar $\Delta\phi_{e\mu}$ distributions

are shown for the Monte Carlo events after detector simulation and reconstruction in Figure 4.43. The same qualitative features already mentioned are seen, but we observe that the opposite-sign, $\Delta\phi_{e\mu} \sim 0°$ peak is now smaller than before reconstruction, relative to the peak at $\Delta\phi_{e\mu} \sim 180°$. This may be understood because two leptons in the same 'jet' are harder to reconstruct. Finally, in Figure 4.44 we show the $\Delta\phi_{e\mu}$ distributions for the CDF data. Again we see in the data a peak in the opposite-sign (and not in the same-sign) $\Delta\phi_{e\mu} \sim 0°$ region. This means that the small $\Delta\phi_{e\mu}$ data has very low fake lepton backgrounds (punchthroughs, fake electrons and remaining photon conversions), which have an azimuthal distribution that cannot depend on the pair sign. We interpret the sign distribution of the small opening angle data as evidence for b production, although we are not yet able to infer the relative contributions of the lower and higher order production mechanisms. For the back-to-back data it is no longer as clear that the backgrounds are as small. There is a moderate excess of opposite-sign data, and backgrounds should be subtracted before a complete discussion.

4.6 BACKGROUNDS TO THE CANDIDATE EVENT

We now discuss possible backgrounds to the high P_T event found in the signal region. First we discuss the possibility that at least one of the leptons in the event is fake (misidentified particle), and then we consider possible dilepton backgrounds from Z^0 decays or diboson (WW and WZ) decays.

Fakes

Let us assume the possibility that the muon in the event is fake. Then the background process is electron+jets where one jet fragments into a 'single particle' that mimics a muon. The number of such events expected in our sample can be estimated as the actual number of e+jets events in the inclusive electron sample, multiplied by the probability that a jet fluctuates into a single particle (P_{single}), and multiplied by the probability for a single particle to be non-interacting (P_{punch}).

Namely,

$$N^{bg}_{e+jets} = N_{e+jets} \times P_{single} \times P_{punch} \tag{4.17}$$

We find the number of events with $E_T^e > 30$ GeV and at least one jet with $E_T^{jet} > 30$ GeV to be $N_{e+jets} = 175$. Jet fragmentation studies provide an estimate of the probability for a jet to fragment into a single particle. Figure 4.45 shows CDF results for the fragmentation function $D(Z) = dN/dZ$, where $Z = P_{long}/P_{jet}$ is the fraction of the jet's momentum carried away by the track [78]. Near the muon track in our event ($P_T^{\mu} = 42.5$ GeV/c), there exists a nearby cluster of 5 soft tracks (Figure 4.20) adding up to $P_T = 5.6$ GeV/c which conceivably could belong to the same jet. In that case the momentum fraction of the track would be of about $z = 42.5/48.1 = 0.88$. An upper limit on P_{single} can be obtained by integrating two last bins (Z between 0.8-0.9 and 0.9-1.0) of the fragmentation plot of Figure 4.45. Since the error bars in the last bins are large, we take as the fragmentation function the value at the bin plus the error bar which takes into account systematic and statistical uncertainties. This gives $P_{single} = 0.0006$. If the bin of Z between 0.7-0.8 is also included then $P_{single} = 0.002$ and we take this as a more conservative upper limit.

Based on test-beam data, the non-interactive pion punch-through probability was found to be $(0.7 \pm 0.1)\%$ in reference [48]. So the background due to real or fake electron + fake muon is :

$$N^{bg}_{e+jets} \lesssim 175 \times 0.002 \times 0.008 = 0.003 \text{ events} . \tag{4.18}$$

The probability for the event having a real muon + fake electron is similarly very small.

Background from Z^0, WW and WZ

We have estimated the signal region ($P_T^{mu} > 15$ GeV/c) backgrounds from $e\mu + X$ final states of the processes $Z^0 \to \tau\tau$, $Z^0 \to b\bar{b}$, and from WW and WZ production and decay. The results are summarized in Table 4.6. The efficiencies for geometrical and P_T cuts, ϵ_{Geom,P_T} were determined at the generator level. For

$Z^0 \to b\bar{b}$ we use an $e\mu$ reconstruction efficiency of $\epsilon^{e\mu}_{Rec} \sim 0.35$ (or about 0.6 per lepton). For the other processes, which give isolated leptons, we used $\epsilon^{e\mu}_{Rec} = 0.71$, obtained from the Z^0 lepton efficiencies in Chapter 3.

In the signal region, we expect 1.1 events from $Z^0 \to \tau\tau$, 0.2 event from $Z^0 \to b\bar{b}$, 0.17 from WW, and 0.015 from WZ. From this alone, one could conclude that the event in the signal region is probably $Z^0 \to \tau\tau$. However, we now argue that this is not the case. Figure 4.46 show E_T^e vs P_T^μ for Monte Carlo $Z^0 \to \tau\tau \to e\mu + X$ events generated inside the signal region. The $\Delta\phi_{e\mu}$ distribution is also shown in this figure. The P_T spectrum is rapidly falling and only $\sim 2\%$ of the events have $P_T^{\tau_{min}} > 30$ GeV/c; in addition, most of the events are back-to-back, with only $\sim 6\%$ with $\Delta\phi_{e\mu}$ below 140°. Overall, the topology of the event in the signal region would be extremely unusual for a $Z \to \tau\tau$. This is also true for $Z \to b\bar{b}$, where the P_T spectrum falls even more sharply (as evidenced by the smaller value of $\epsilon_{Geom_P_T}$ in Table 4.6) because the B-meson which decays semileptonically only carries part of the momentum of the produced b-quark (Figure 1.14).

Parenthetically, the event in Figure 4.14 with $E_T^e = 37$ GeV and $P_T^\mu = 11$ GeV/c, has back-to-back, isolated leptons, and no significant extra activity in the calorimetry. We consider this event to be a $Z^0 \to \tau\tau$ candidate, and displays of it are shown in Figures 4.47 and 4.48.

The E_T^e vs P_T^μ and $\Delta\phi_{e\mu}$ distributions are shown in Figure 4.49 for Monte Carlo $WW \to e\mu + X$ events generated inside the signal region. In these variables, the topology of the event in the signal region is not inconsistent with WW. However, the presence of the forward muon and of the 14 GeV jet in the event and the small cross section for this process make it extremely unlikely for it to be WW. The forward muon makes it plausible for the event to be WZ, or W-Drell-Yan (where the dimuon is from Z or Drell-Yan). Here the rate is already small, and the additional jet makes it even less likely.

4.7 CONCLUSIONS

We have motivated and defined a signal region for the $t\bar{t} \to e\mu + X$ search and have determined the detection efficiency as a function of M_{top}. With this approach, we have searched for the top in a data sample with integrated luminosity of 4.4 pb^{-1} collected during the 1988-89 CDF run. In addition, we have studied a sub-sample of data with lower P_T thresholds. The bulk of the data appears to be consistent with expectations from QCD heavy flavor production, and only one $t\bar{t}$ candidate event was found in the signal region. We find that this event is difficult to explain in terms of known sources of background.

	M_{top} (GeV/c^2)					
	28	40	60	70	80	90
i)	0.94	0.87	0.82	0.80	0.78	0.82
ii)	0.02	0.03	0.07	0.08	0.09	0.12
iii)	0.04	0.10	0.11	0.12	0.13	0.06

Table 4.1: The contributions to the $t\bar{t} \rightarrow e\mu + X$ signal : i) both leptons come directly from the top decay; ii) at least one lepton is coming from the decay of a τ; and iii) leptons coming from the decays of a b or c quark are involved

M_{top} [GeV/c^2]	$\epsilon^{e\mu}_{Geom.,P_T} \pm stat. \pm sys.$
28	$0.0103 \pm 0.0015 \pm 0.0030$
40	$0.043 \pm 0.002 \pm 0.007$
60	$0.142 \pm 0.007 \pm 0.009$
70	$0.209 \pm 0.008 \pm 0.008$
80	$0.294 \pm 0.012 \pm 0.015$
90	$0.324 \pm 0.013 \pm 0.013$

Table 4.2: Acceptance to the η and P_T cuts normalized to the double semileptonic branching ratio of $\frac{2}{81}$. The acceptance has been taken as the intermediate value between the ISAJET and PAPAGENO calculations, the associated systematic uncertainty is half the difference of the acceptances.

M_{top} [GeV/c^2]	ϵ^{all}_{Cal}	ϵ^{iso}_{Cal}	ϵ^{e}_{over}	ϵ^{e}_{top}
28	0.894	0.943	0.948	0.69 ± 0.02
40	0.904	0.954	0.948	0.69 ± 0.02
60	0.892	0.949	0.940	0.69 ± 0.01
70	0.868	0.928	0.935	0.68 ± 0.01
80	0.858	0.920	0.933	0.68 ± 0.01
90	0.902	0.943	0.957	0.70 ± 0.01

Table 4.3: The top electron efficiencies. ϵ^{e}_{top} is the total electron detection efficiency inside the fiducial volume, including losses due to overlapping particles and to the photon conversion cuts. Only the Monte Carlo statistical uncertainty is included.

M_{top} GeV/c^2	$\epsilon^{all}_{over\ lower}$	$\epsilon^{\mu\mu}_{over\ lower}$	$\epsilon^{\mu}_{over\ lower}$	$\epsilon^{CMIO}_{cosmic\ cut}$	ϵ^{μ}_{top}
28	0.923	0.958	0.963	0.948	0.89 ± 0.02
40	0.918	0.963	0.953	0.953	0.88 ± 0.02
60	0.900	0.971	0.927	0.951	0.86 ± 0.01
70	0.898	0.972	0.924	0.950	0.85 ± 0.01
80	0.898	0.976	0.920	0.943	0.84 ± 0.01
90	0.926	0.969	0.956	0.968	0.90 ± 0.01

Table 4.4: The top muon efficiencies. ϵ^{μ}_{top} is the total muon detection efficiency inside the fiducial volume, including losses due to overlap with other particles. Only Monte Carlo statistical errors are included.

M_{top} GeV/c^2	$\epsilon^{e\mu}_{P_T}$	$\epsilon^{e\mu}_{Geom}$	$\epsilon^{e\mu}_{Rec}$	$\epsilon^{e\mu}_{Total}$
28	0.035	0.30	0.61	0.0064 ± 0.011
40	0.120	0.36	0.61	0.0260 ± 0.015
60	0.398	0.36	0.59	0.083 ± 0.004
70	0.520	0.40	0.58	0.121 ± 0.006
80	0.783	0.38	0.57	0.167 ± 0.008
90	0.896	0.36	0.63	0.203 ± 0.010

Table 4.5: The $t\bar{t} \to e\mu + X$ efficiencies for: i) the P_T cuts, ii) geometric acceptance (after P_T cuts), iii) dilepton reconstruction (after P_T and geometry cuts), and iv) total. Only the Monte Carlo statistical uncertainty is included.

	$Z^0 \to \tau\tau$	$Z^0 \to b\bar{b}$	WW	WZ
σ [pb]	200	910	7	2
$B\tau \to e\mu$ [%]	6.1	2.1	2.5	0.74
ϵ_{Geom,P_T}	0.030	0.0056	0.32	0.32
$\epsilon^{e\mu}_{Rec}$	0.71	~ 0.35	0.71	0.71
σ_{obs} [pb]	0.26	0.037	0.039	0.0034
Events in 4.4 pb^{-1}	1.1	0.2	0.17	0.015

Table 4.6: Backgrounds to $t\bar{t} \to e\mu + X$. Here, $\sigma_{obs} = \sigma \cdot B\tau \cdot \epsilon_{Geom,P_T} \cdot \epsilon^{e\mu}_{Rec}$.

Run 19250, Event 20435.

	Charge	P_T [GeV/c]	η	ϕ [degrees]
Central Electron	+	31.7	−0.81	132
Central Muon	−	42.5	−0.80	269
Forward Muon	+	9.9	−2.0	98
Jet 1		14	1.1	341
Jet 2		5	−2.8	88

Table 4.7: Characteristics of the top candidate event. Calorimeter E_T is used in the P_T column for the electron and jet clusters.

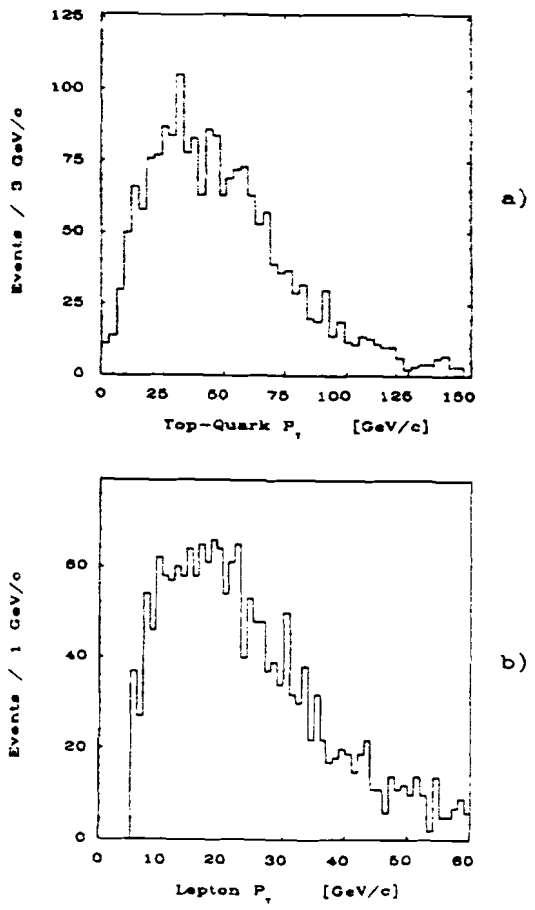

Figure 4.1: The generated P_T spectra of a) the top quark, and b) the leptons from t-decay , for direct $t\bar{t}$ pair production at $M_{top} = 70$ GeV/c^2.

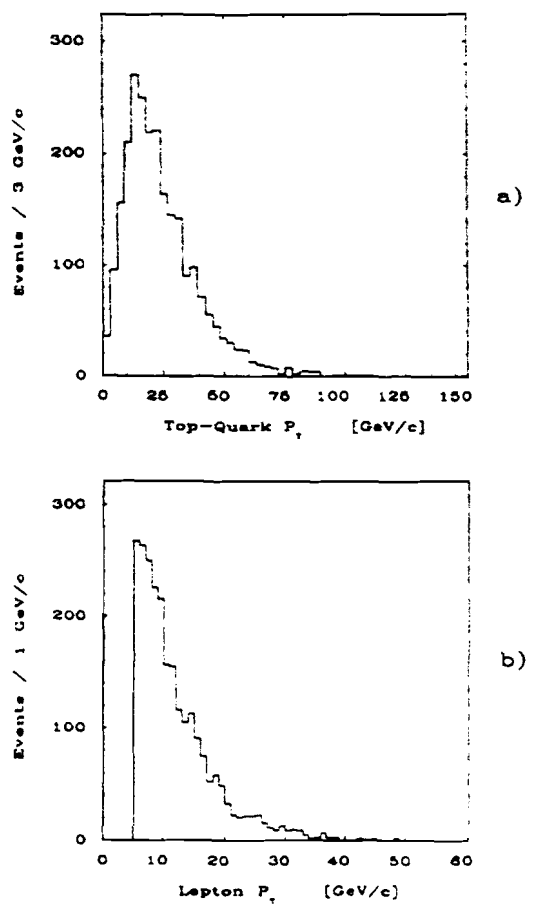

Figure 4.2: The generated P_T spectra of a) the top quark, and b) the leptons from t-decay , for direct $t\bar{t}$ pair production at $M_{top} = 28$ GeV/c^2.

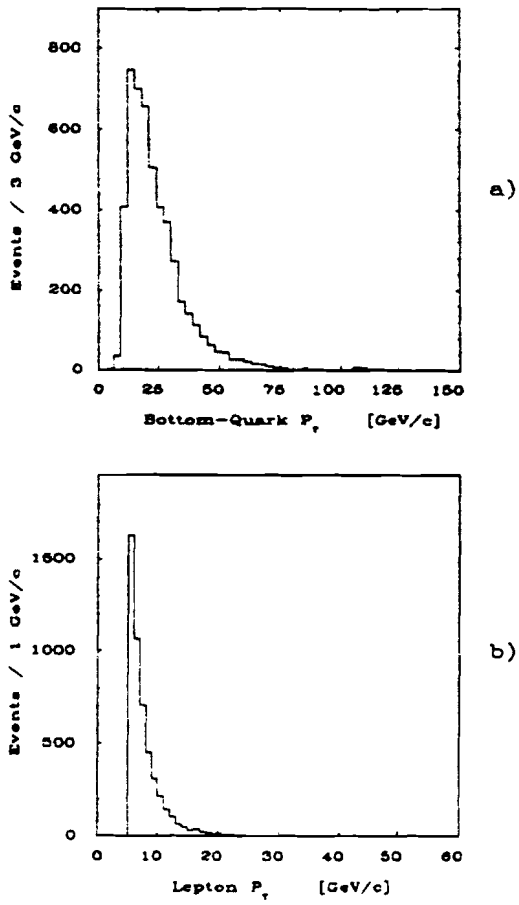

Figure 4.3: The generated P_T spectra of a) the bottom quark, and b) the leptons from b-decay , for direct $b\bar{b}$ production.

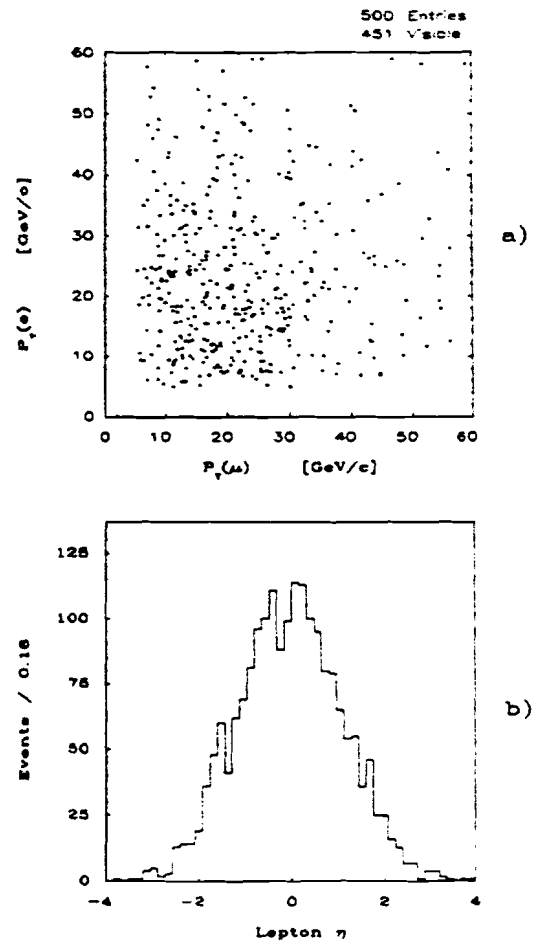

Figure 4.4: a) E_T^e versus P_T^μ , and b) lepton pseudorapidity distribution, for $t\bar{t}$ pairs of $M_{top} = 70$ GeV/c^2.

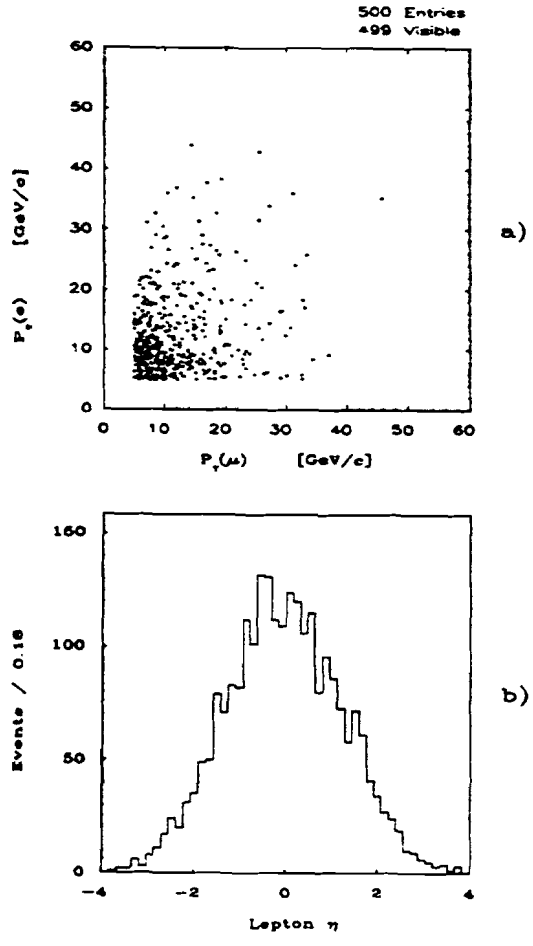

Figure 4.5: a) E_T^e versus P_T^μ , and b) lepton pseudorapidity distribution, for $t\bar{t}$ pairs of $M_{top} = 28$ GeV/c^2.

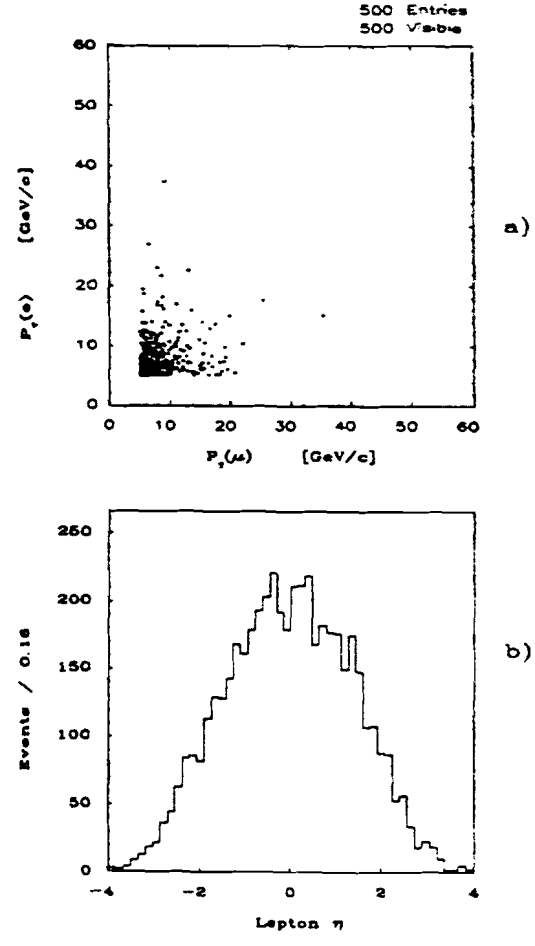

Figure 4.6: a) E_T^e versus P_T^μ , and b) lepton pseudorapidity distribution, for directly produced $b\bar{b}$ pairs.

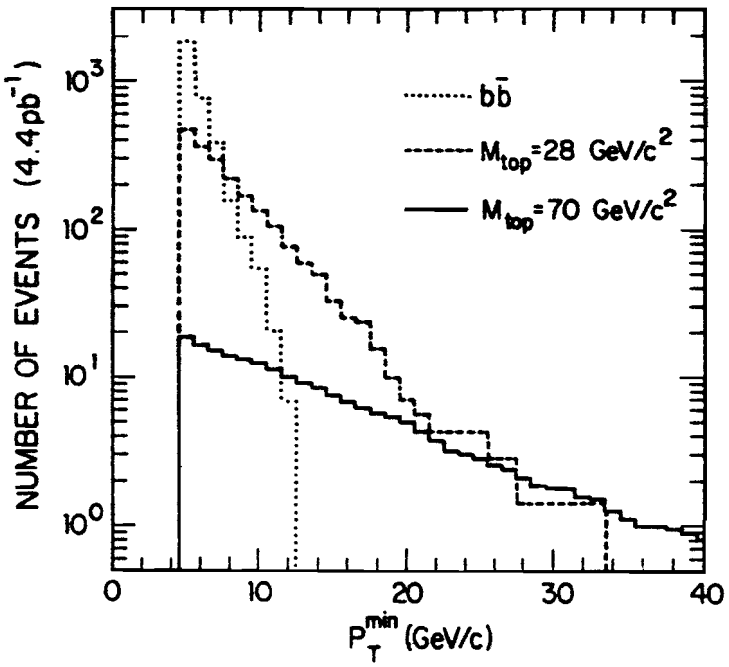

Figure 4.7: The expected number of opposite-sign events for 4.4 pb^{-1} with $E_T^e > P_T^{min}$ and $P_T^\mu > P_T^{min}$ as a function of the threshold P_T^{min} for ISAJET $t\bar{t}$ and $b\bar{b}$ events.

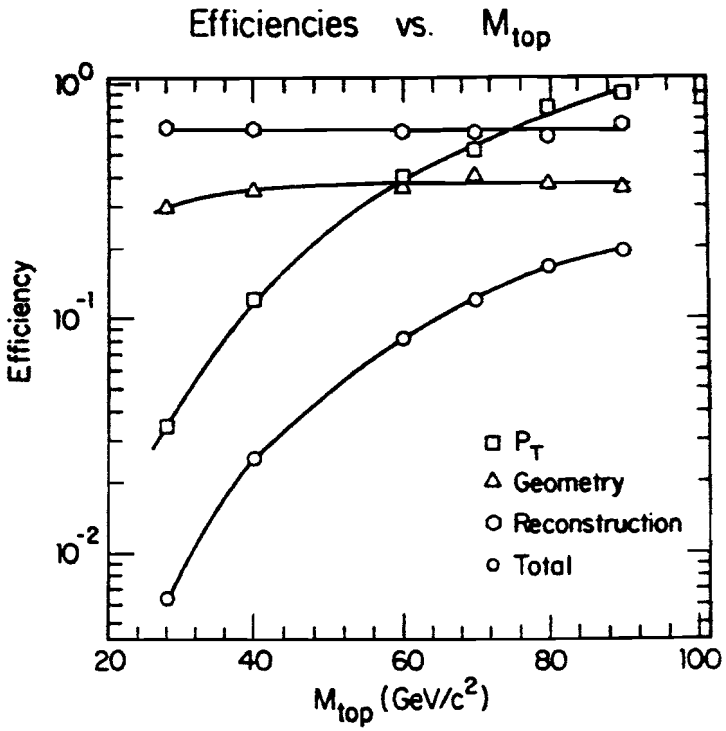

Figure 4.8: The $t\bar{t} \rightarrow e\mu + X$ efficiencies for: i) the P_T cuts , ii) geometric acceptance (after P_T cuts), iii) dilepton reconstruction (after P_T and geometry cuts), and iv) total.

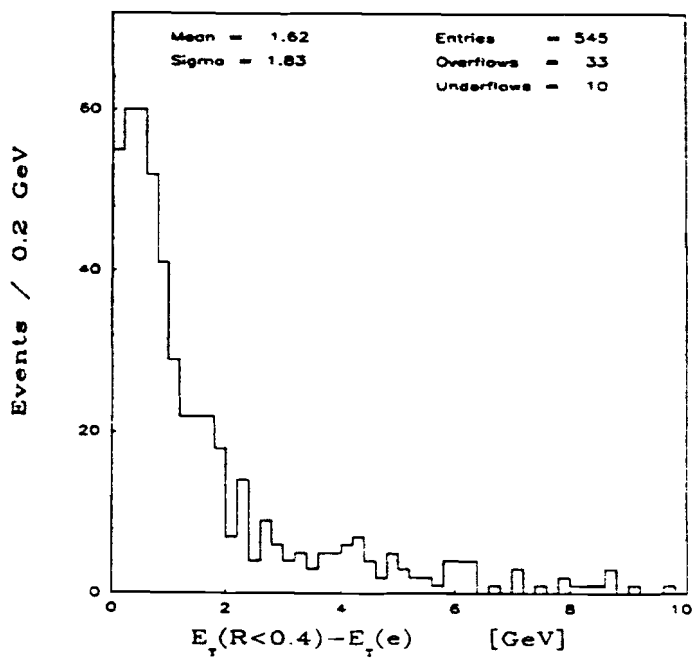

Figure 4.9: The transverse energy inside a cone of R= 0.4 about the electron, excluding the electron transverse energy, for electrons from top decay for M_{top} = 28 GeV/c^2.

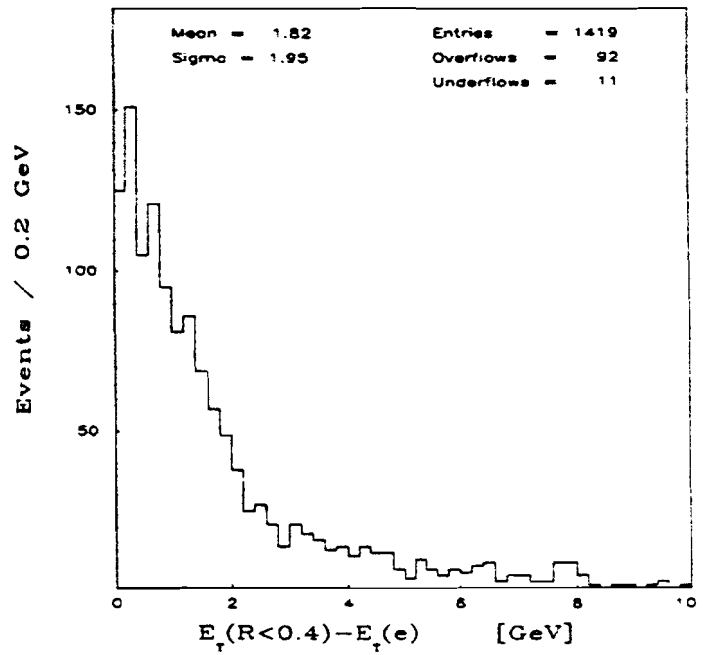

Figure 4.10: The transverse energy inside a cone of R= 0.4 about the electron, excluding the electron transverse energy, for electrons from top decay for M_{top} = 70 GeV/c^2.

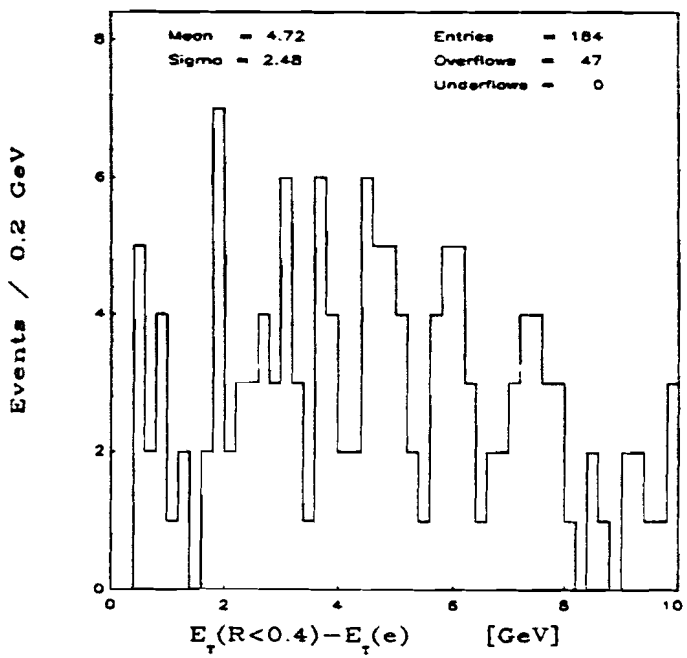

Figure 4.11: The transverse energy inside a cone of R= 0.4 about the electron, excluding the electron transverse energy, for electrons from $b\bar{b}$ Monte Carlo.

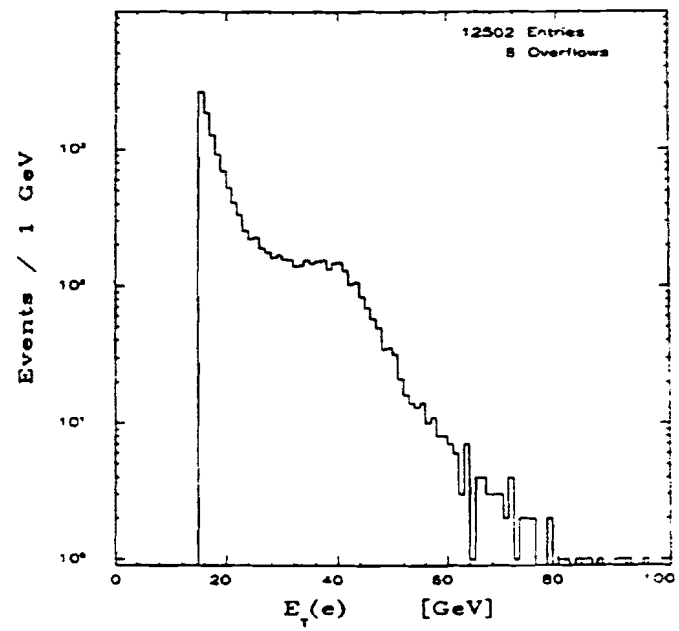

Figure 4.12: Inclusive electron spectrum for CDF data with integrated luminosity of 4.4 pb^{-1}.

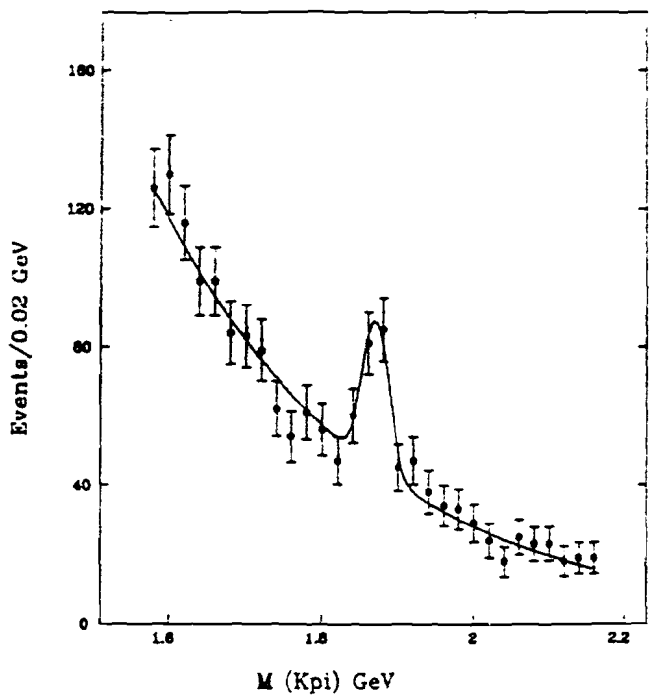

Figure 4.13: $K\pi$ invariant mass for track pairs near an electron. The peak corresponds to $D^0 \to K\pi$ decays from $B \to D^0 e\nu$. From reference [76].

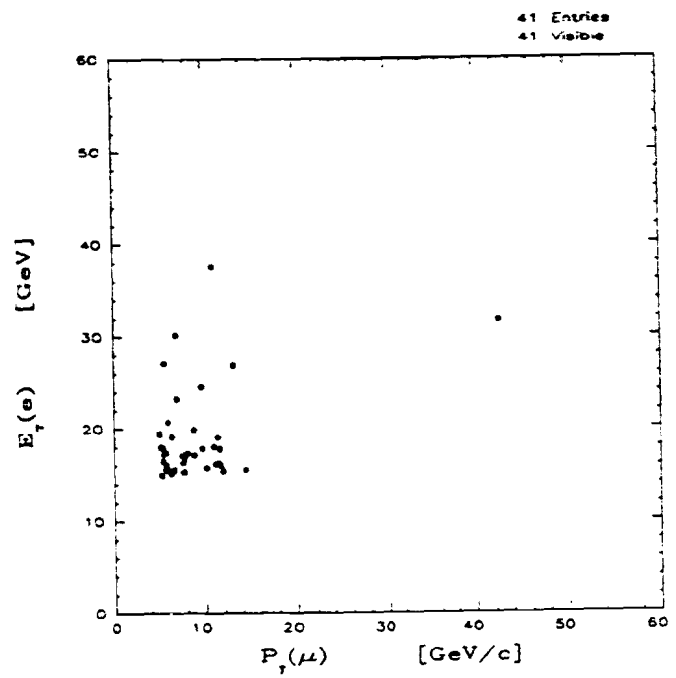

Figure 4.14: Electron transverse energy vs. muon transverse momentum for CDF data with an integrated luminosity of 4.4 pb^{-1}. Only opposite-sign events are shown in this figure.

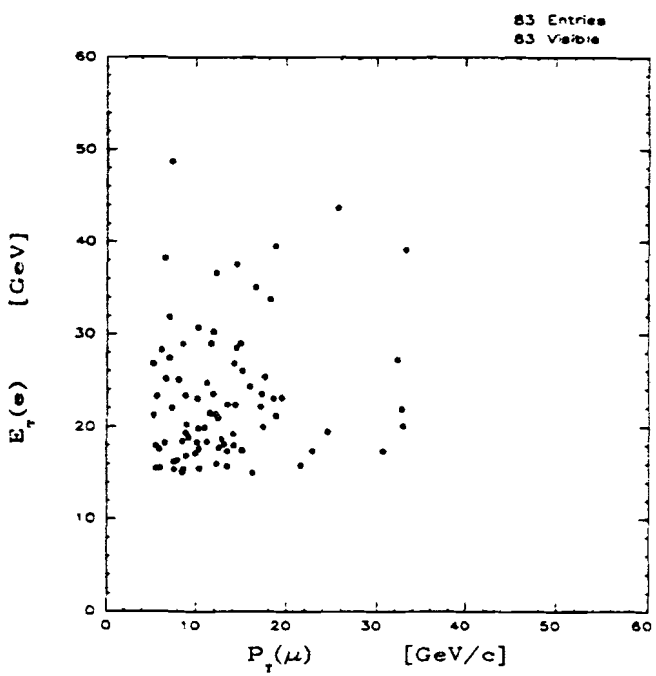

Figure 4.15: Electron transverse energy vs. muon transverse momentum for $t\bar{t}$ Monte Carlo data (M_{top} = 28 GeV/c^2) with an integrated luminosity of 3 pb^{-1}. Only opposite-sign events are shown in this figure.

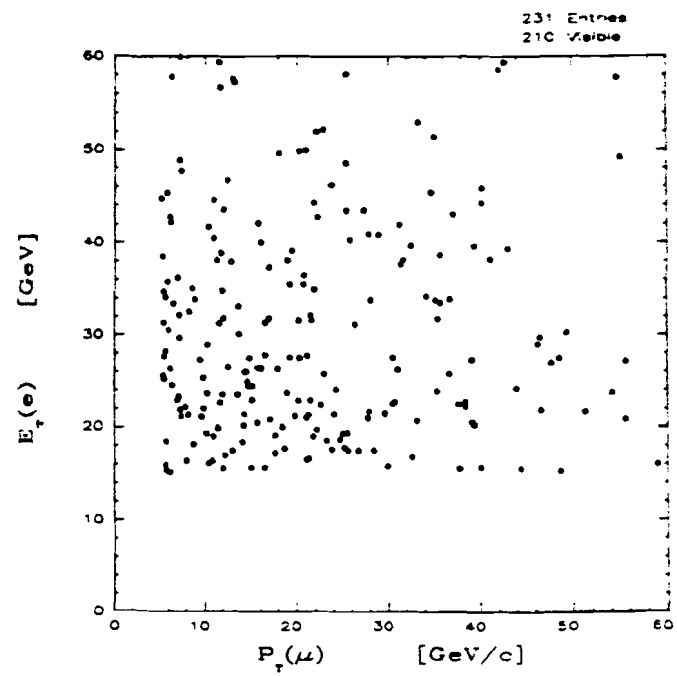

Figure 4.16: Electron transverse energy vs. muon transverse momentum for $t\bar{t}$ Monte Carlo data (M_{top} = 70 GeV/c^2) with an integrated luminosity of 80 pb^{-1}. Only opposite-sign events are shown in this figure.

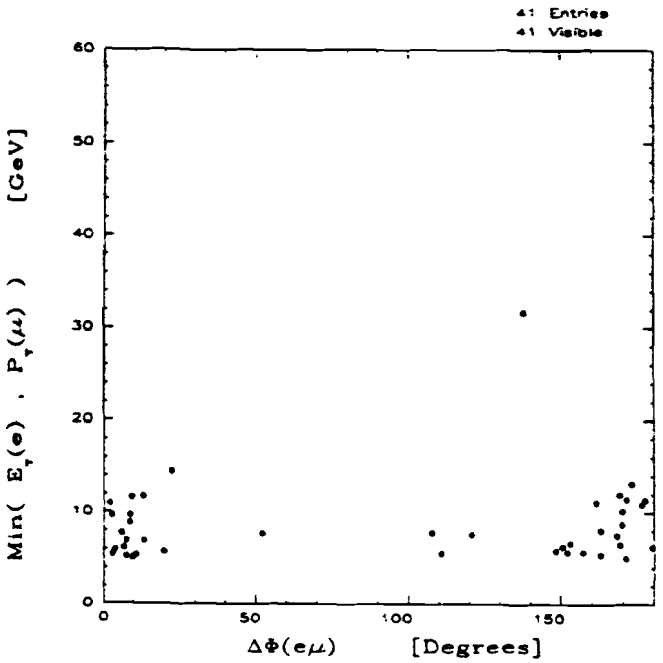

Figure 4.17: P_T^{min} =Min(E_T^e, P_T^μ) versus the azimuthal separation between electron and muon for CDF data with an integrated luminosity of 4.4 pb^{-1}. Only opposite-sign events are shown in this figure.

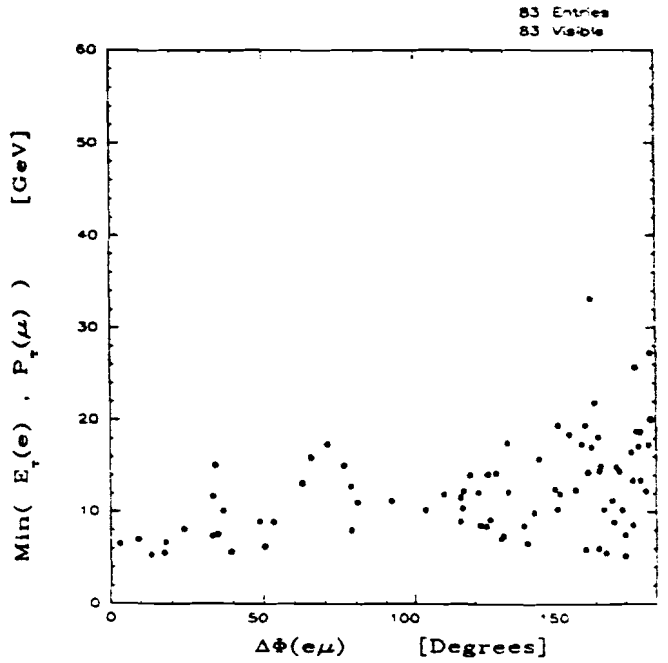

Figure 4.18: P_T^{min} =Min(E_T^e, P_T^μ) versus the azimuthal separation between electron and muon for $t\bar{t}$ Monte Carlo data (M_{top} = 28 GeV/c^2) with an integrated luminosity of 3 pb^{-1}. Only opposite-sign events are shown in this figure.

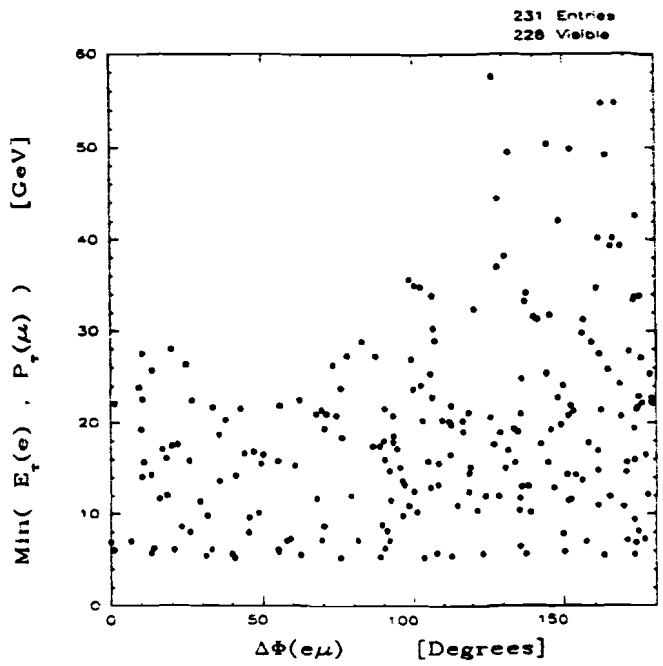

Figure 4.19: P_T^{min} =Min(E_T^e, P_T^μ) versus the azimuthal separation between electron and muon for $t\bar{t}$ Monte Carlo data (M_{top} = 70 GeV/c^2) with an integrated luminosity of 80 pb^{-1}. Only opposite-sign events are shown in this figure.

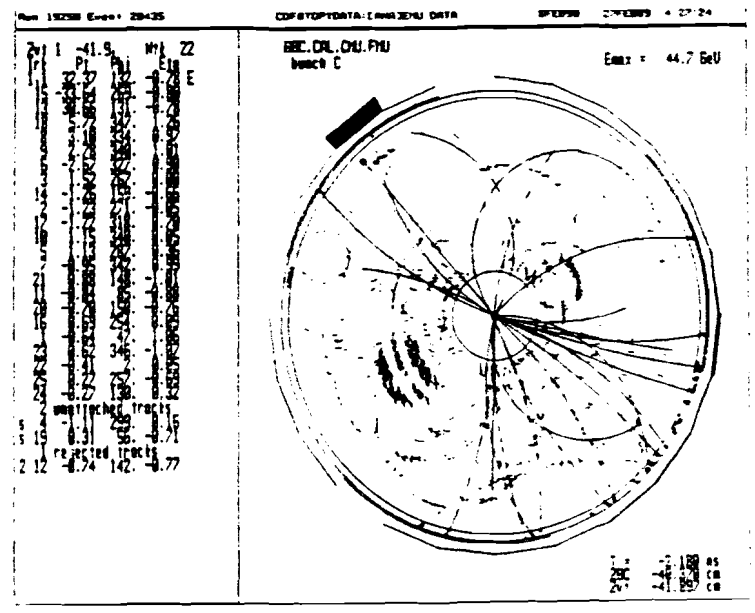

Figure 4.20: A CTC display of the top candidate event.

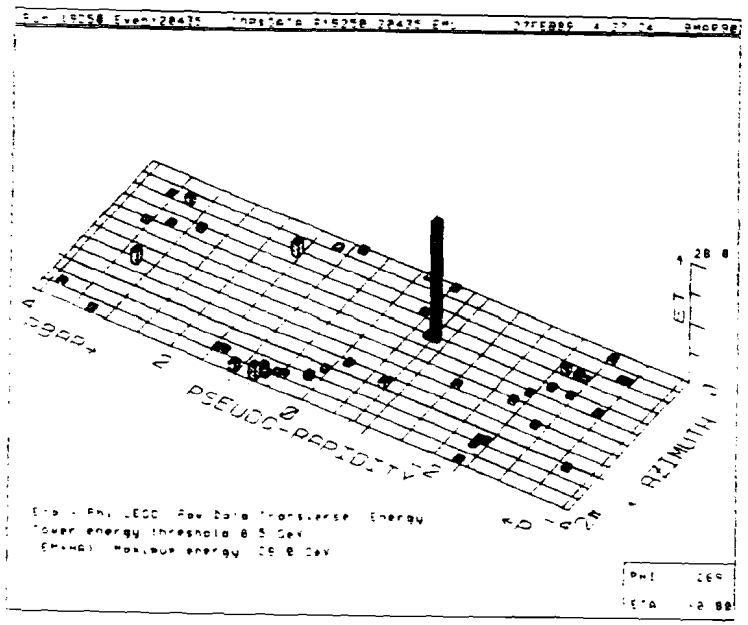

Figure 4.21: A calorimeter display of the top candidate event.

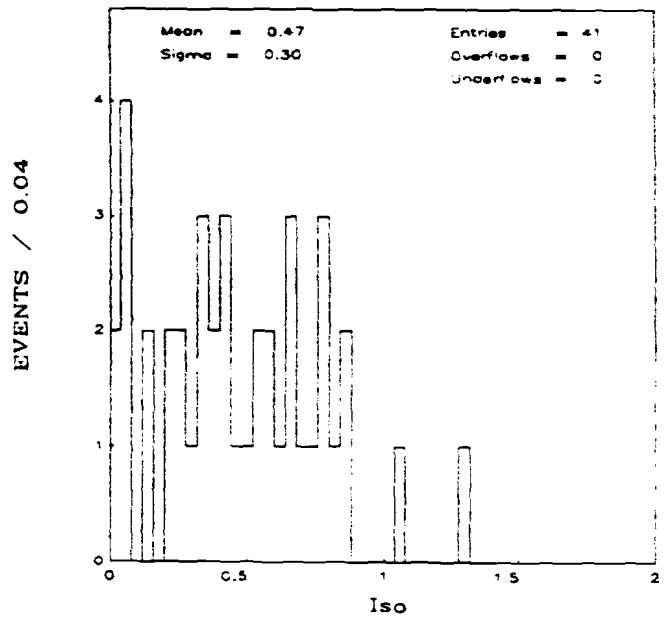

Figure 4.22: Electron isolation, $Iso = (E_T^{R<0.7} - E_T^e)/E_T^e$, for CDF data with an integrated luminosity of 4.4 pb^{-1}. Only opposite-sign events are shown in this figure.

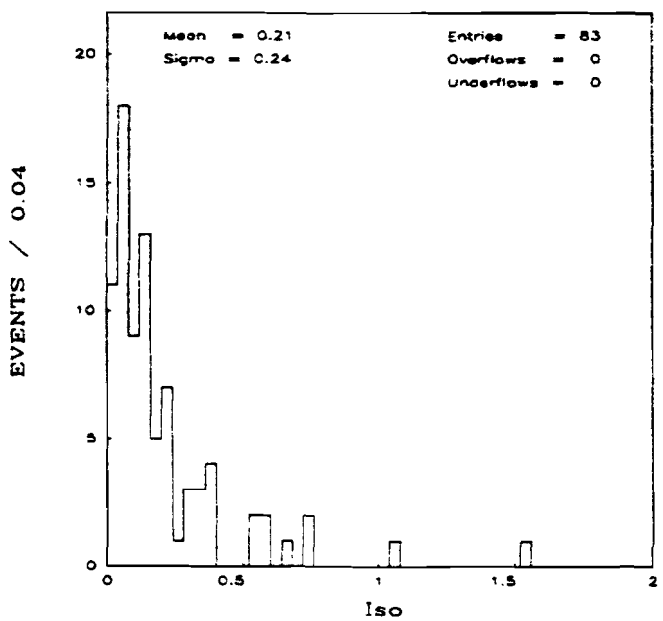

Figure 4.23: Electron isolation, $Iso = (E_T^{R<0.7} - E_T^e)/E_T^e$, for $t\bar{t}$ Monte Carlo data (M_{top} = 28 GeV/c^2) with an integrated luminosity of 3 pb^{-1}. Only opposite-sign events are shown in this figure.

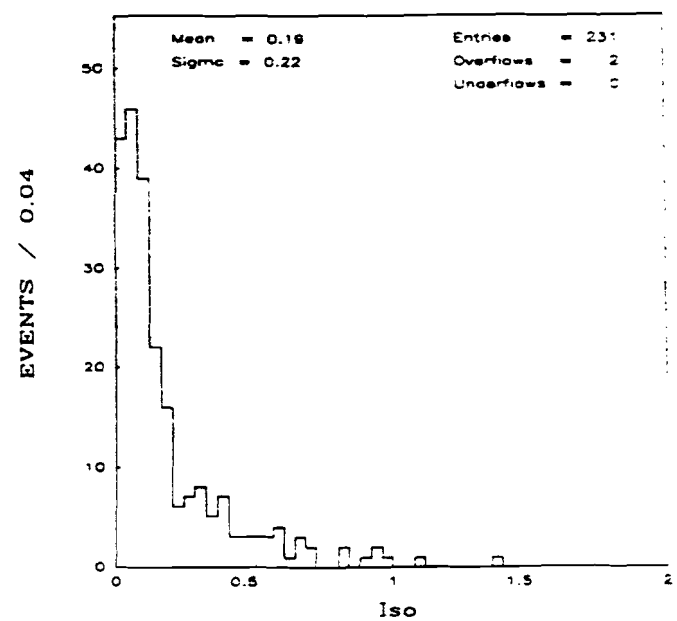

Figure 4.24: Electron isolation, $Iso = (E_T^{R<0.7} - E_T^e)/E_T^e$, for $t\bar{t}$ Monte Carlo data (M_{top} = 70 GeV/c^2) with an integrated luminosity of 80 pb^{-1}. Only opposite-sign events are shown in this figure.

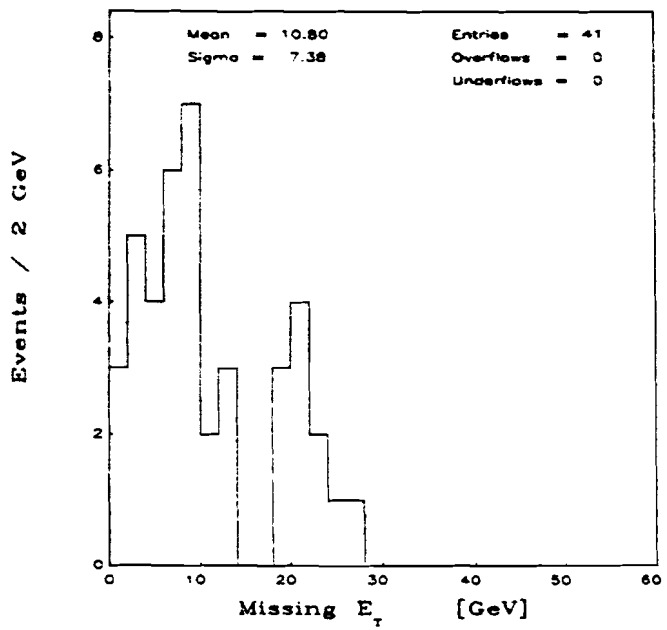

Figure 4.25: Missing transverse momentum for CDF data with an integrated luminosity of 4.4 pb^{-1}. Only opposite-sign events are shown in this figure.

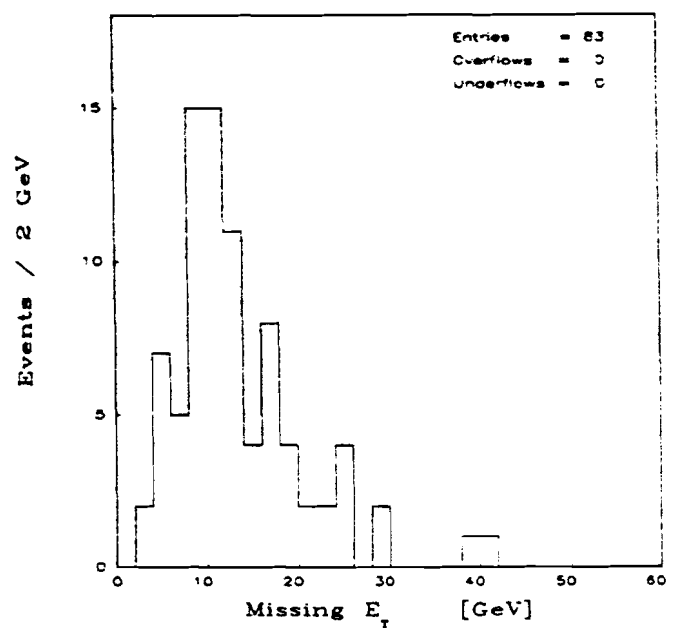

Figure 4.26: Missing transverse momentum for $t\bar{t}$ Monte Carlo data (M_{top} = 25 GeV/c^2) with an integrated luminosity of 3 pb^{-1}. Only opposite-sign events are shown in this figure.

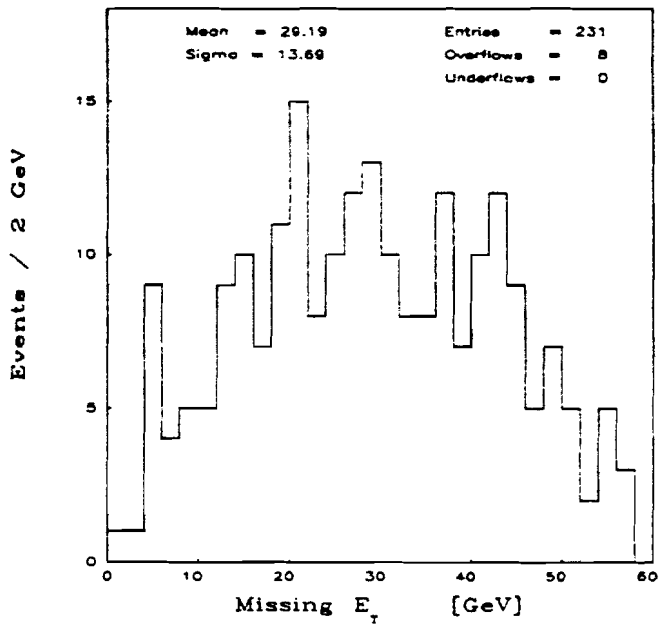

Figure 4.27: Missing transverse momentum for $t\bar{t}$ Monte Carlo data (M_{top} = 70 GeV/c^2) with an integrated luminosity of 80 pb^{-1}. Only opposite-sign events are shown in this figure.

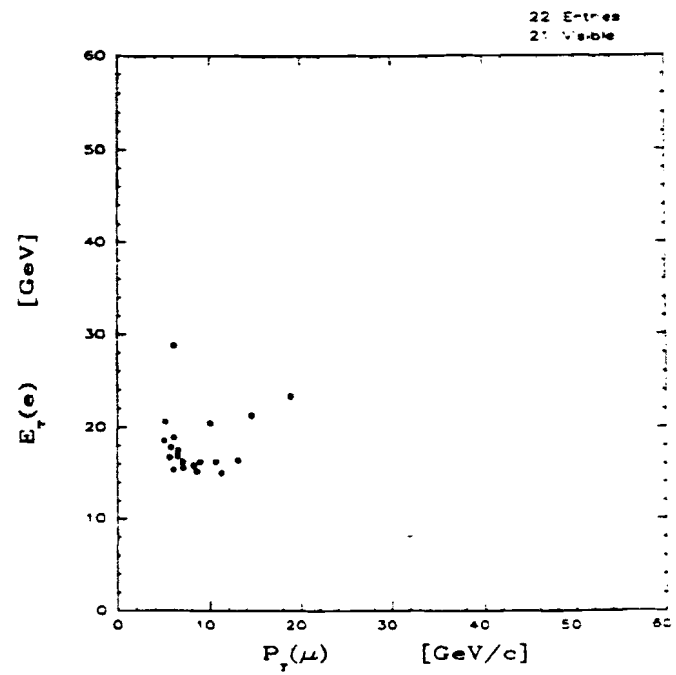

Figure 4.28: Electron transverse energy vs. muon transverse momentum for CDF data with an integrated luminosity of 4.4 pb^{-1}. Only same-sign events are shown in this figure.

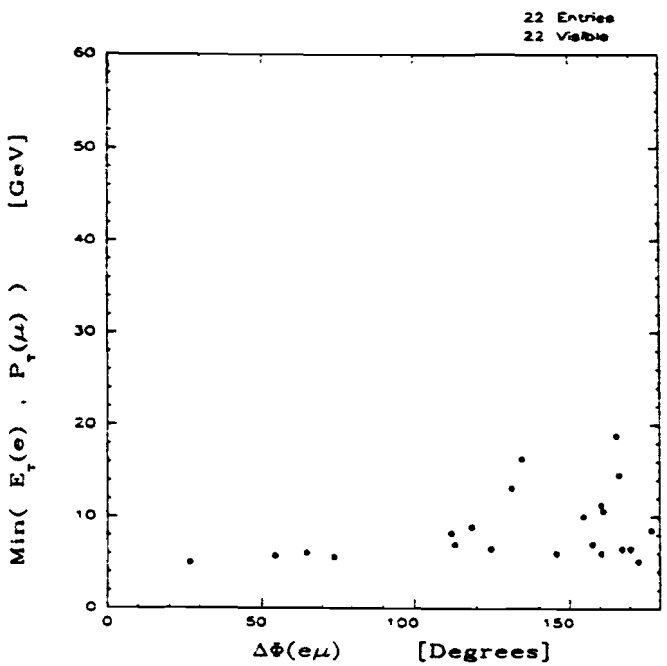

Figure 4.29: Min(E_T^e, P_T^μ) versus the azimuthal separation between electron and muon for CDF data with an integrated luminosity of 4.4 pb^{-1}. Only same-sign events are shown in this figure.

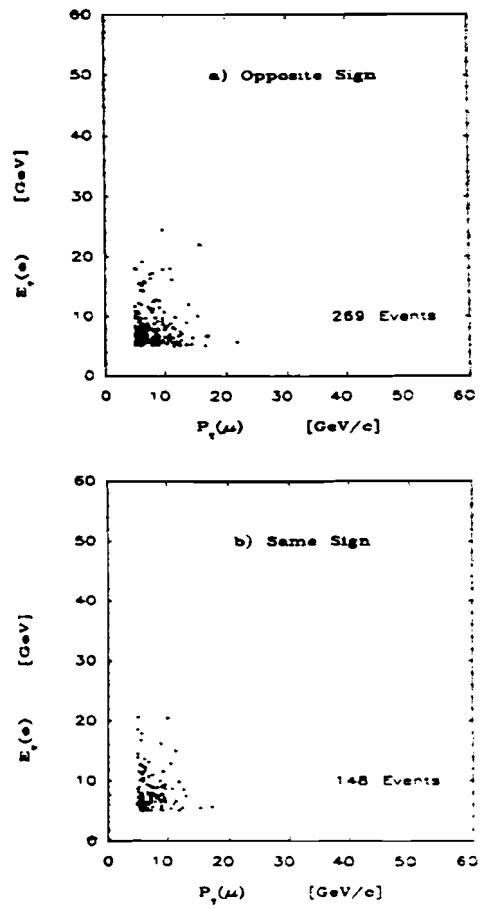

Figure 4.30: E_T^e vs. P_T^μ for CDF low threshold, $e\mu$ data with an integrated luminosity of 1.8 pb^{-1}. a) Opposite-sign data, and b) same-sign data.

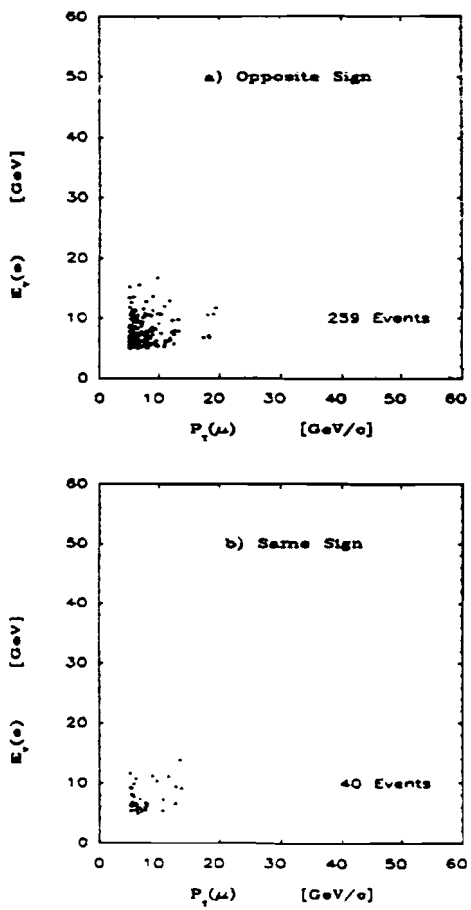

Figure 4.31: E_T^e vs. P_T^μ for $b\bar{b}$ Monte Carlo data with an integrated luminosity of 0.64 pb^{-1}. a) Opposite-sign data, and b) same-sign data.

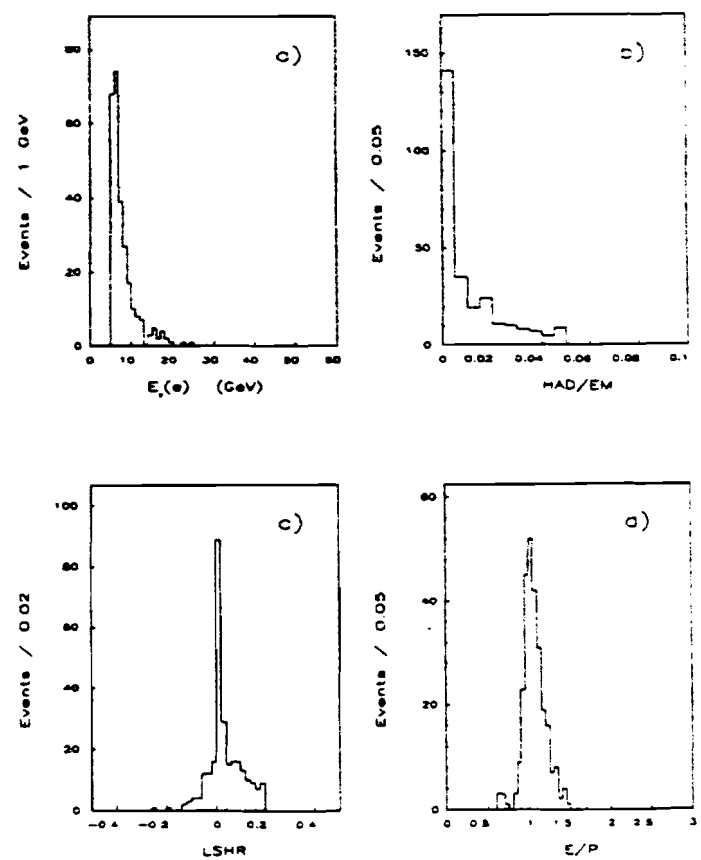

Figure 4.32: Electron variables for CDF low threshold opposite-sign $e\mu$ data. a) Transverse momentum (E_T^e), b) Hadronic to electromagnetic energy ratio (HAD/EM), c) Lateral sharing ($Lshr$), and c) Ratio of calorimeter energy to track momentum (E/P).

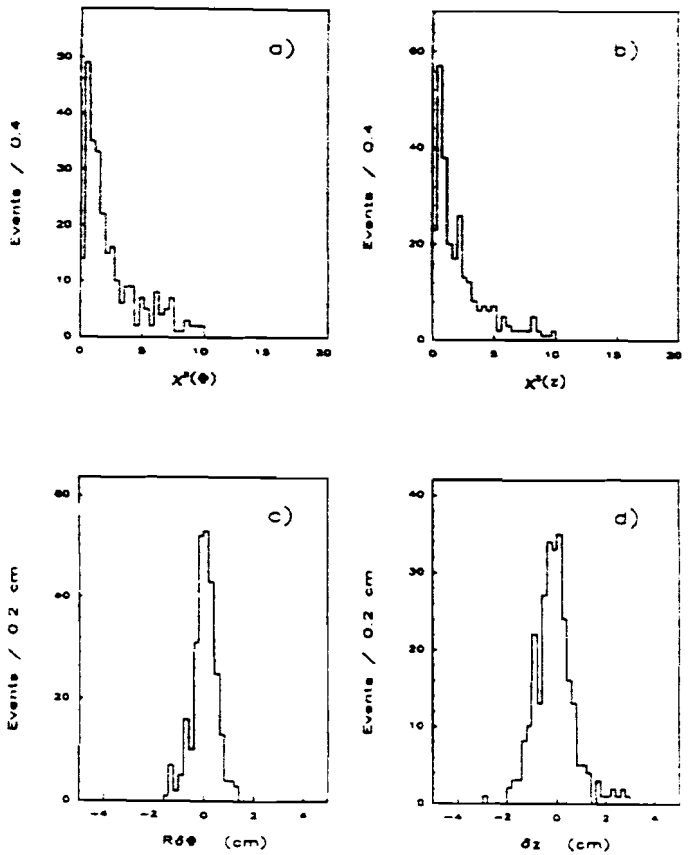

Figure 4.33: Electron variables for CDF low threshold opposite-sign $e\mu$ data. a) Strip chamber χ^2_ϕ, b) strip chamber χ^2_z, c) track-strip matching in ϕ ($R\delta\phi$), d) track-strip matching along z (δz).

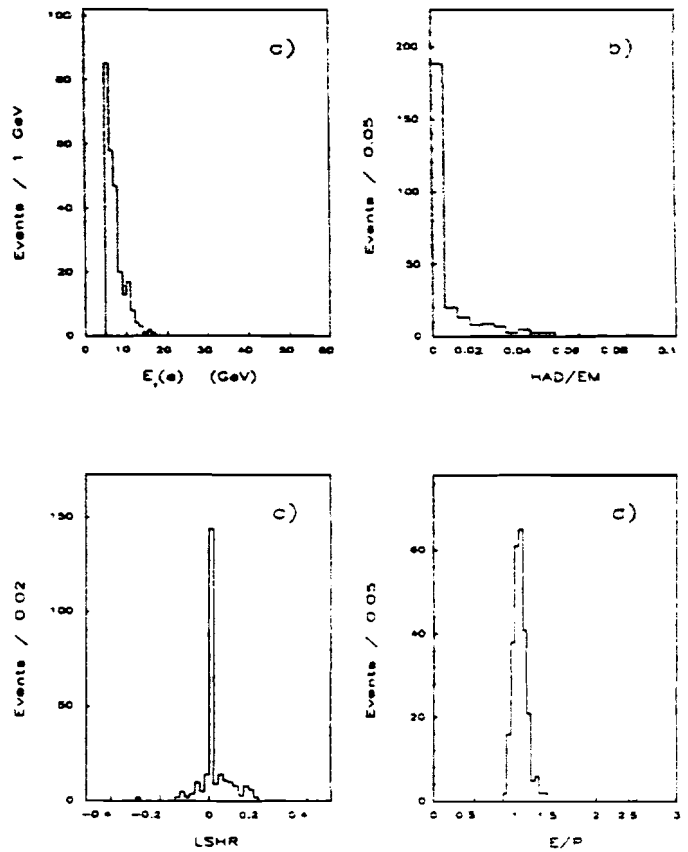

Figure 4.34: Electron variables for $b\bar{b}$ Monte Carlo opposite-sign data. a) Transverse momentum (E_T^e), b) Hadronic to electromagnetic energy ratio (HAD/EM), c) Lateral sharing ($Lshr$), and c) Ratio of calorimeter energy to track momentum (E/P).

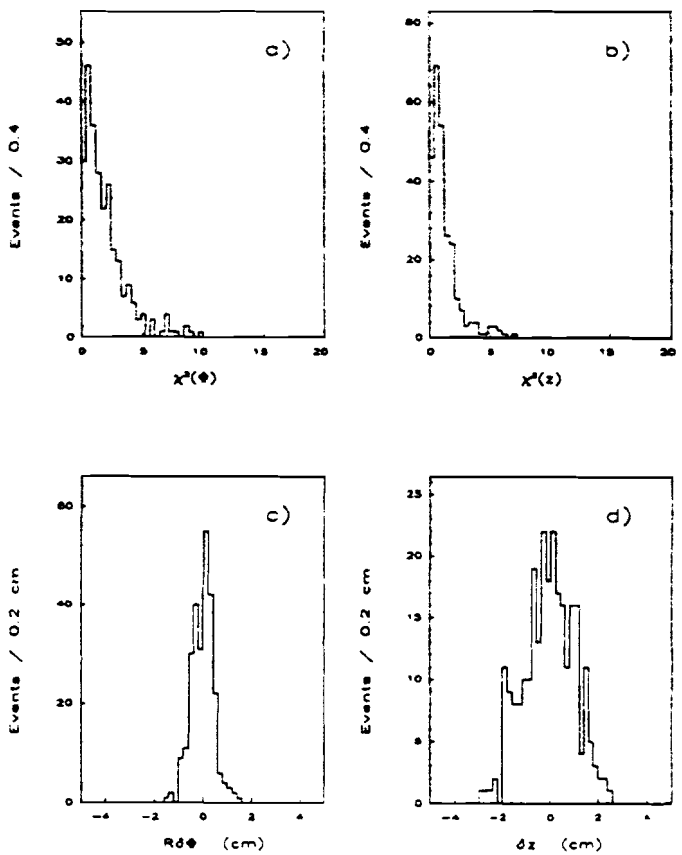

Figure 4.35: Electron variables for $b\bar{b}$ Monte Carlo opposite-sign data. a) Strip chamber χ^2_ϕ, b) strip chamber χ^2_z, c) track-strip matching in ϕ ($R\delta\phi$), d) track-strip matching along z (δz).

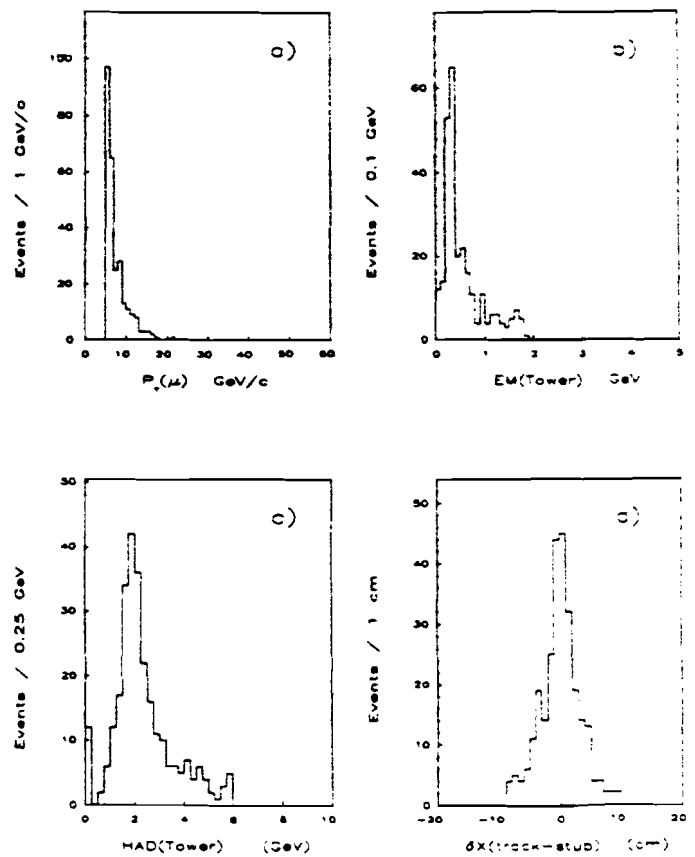

Figure 4.36: Muon variables for CDF low threshold opposite-sign $e\mu$ data. a) Transverse momentum P_T^μ, b) E_{EM}^{tower}, c) E_{HAD}^{tower}, d) matching in azimuth $\delta X_{track-stub}$.

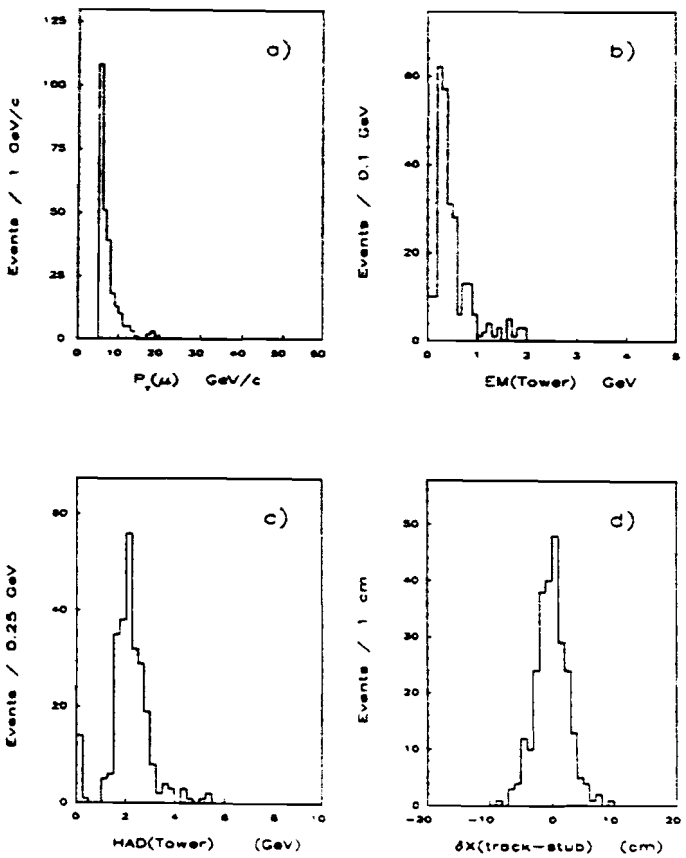

Figure 4.37: Muon variables for $b\bar{b}$ Monte Carlo opposite-sign data. a) Transverse momentum P_T^{μ}, b) E_{EM}^{tower}, c) E_{HAD}^{tower}, d) matching in azimuth $\delta X_{track-stub}$.

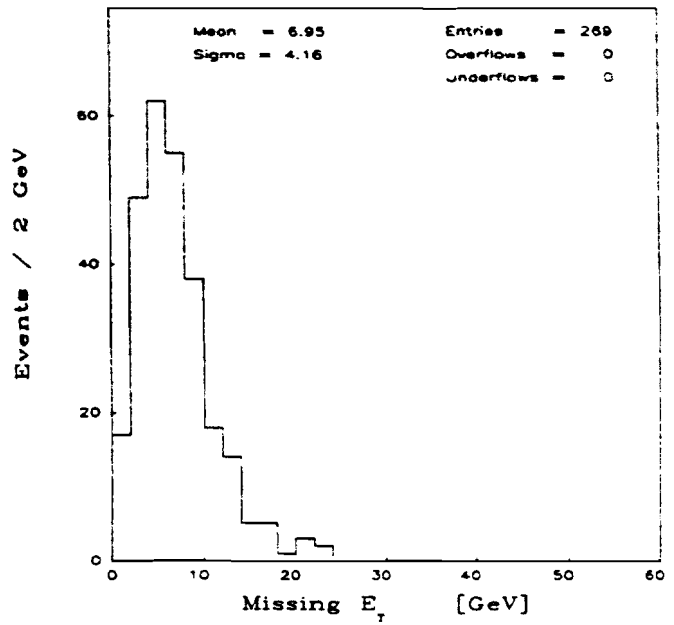

Figure 4.38: Missing transverse energy for CDF low threshold, opposite-sign $e\mu$ data with an integrated luminosity of 1.8 pb^{-1}.

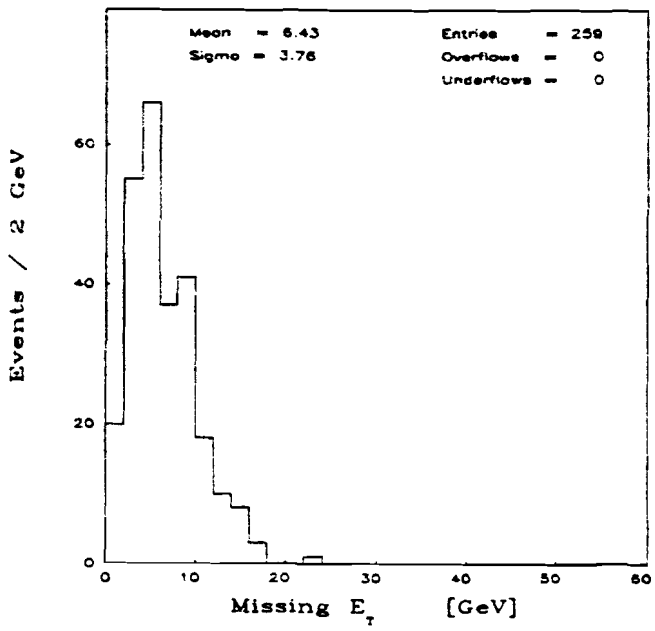

Figure 4.39: Missing transverse energy for $b\bar{b}$ Monte Carlo opposite-sign data with an integrated luminosity of 0.64 pb^{-1}.

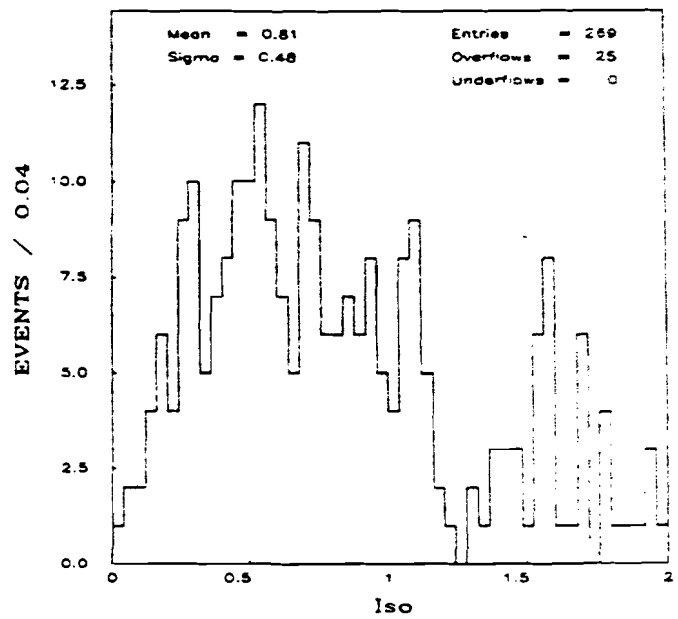

Figure 4.40: Electron isolation, $Iso = (E_T^{R<0.7} - E_T^e)/E_T^e$, for CDF low threshold, opposite-sign $e\mu$ data with an integrated luminosity of 1.8 pb^{-1}.

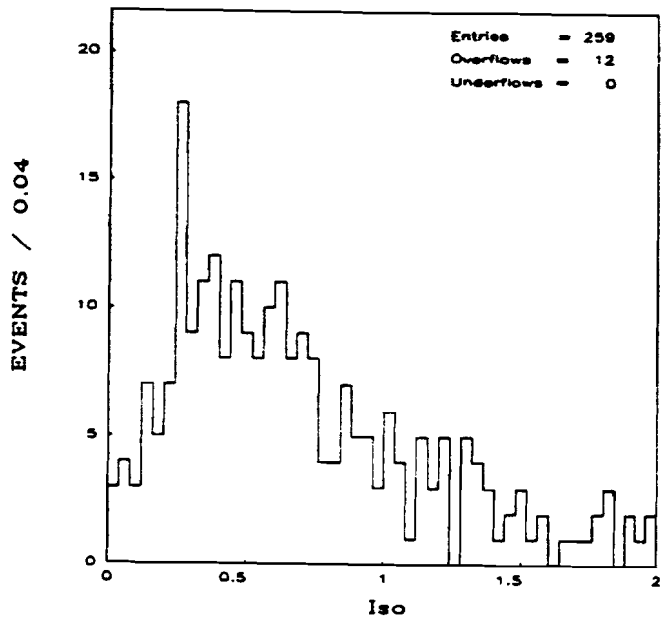

Figure 4.41: Electron isolation, $I_{so} = (E_T^{R<0.7} - E_T^e)/E_T^e$, for $b\bar{b}$ Monte Carlo opposite-sign data with an integrated luminosity of 0.64 pb^{-1}.

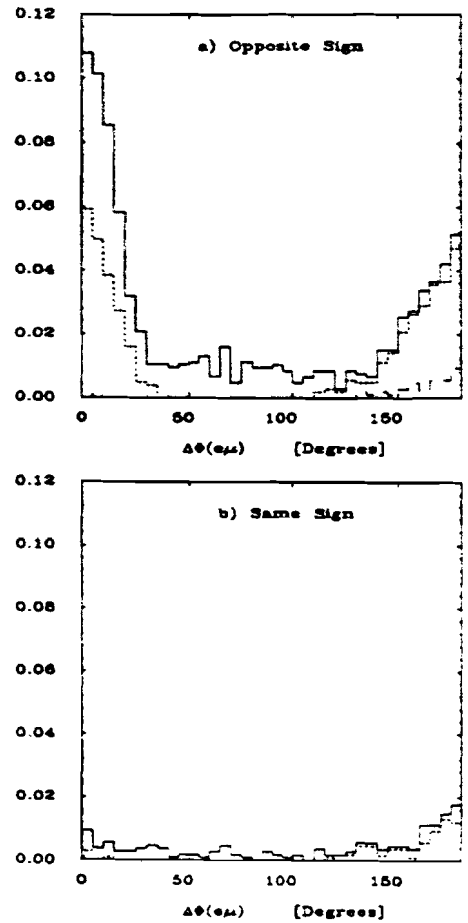

Figure 4.42: $\Delta\phi_{e\mu}$ for a) opposite-sign and b) same-sign, for the generated events. The dashed line is for direct $c\bar{c}$; the dotted line for direct $b\bar{b} - c\bar{c}$; and the solid line is the total, including gluon splitting and flavor excitation.

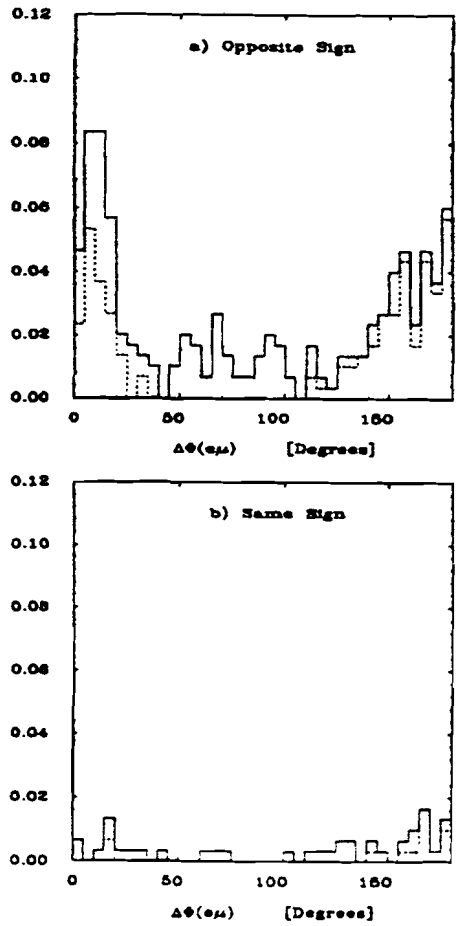

Figure 4.43: $\Delta\phi_{e\mu}$ for a) opposite-sign and b) same-sign, after reconstruction. The dotted line is for direct $b\bar{b} + c\bar{c}$; and the solid line is the total, including gluon splitting and flavor excitation.

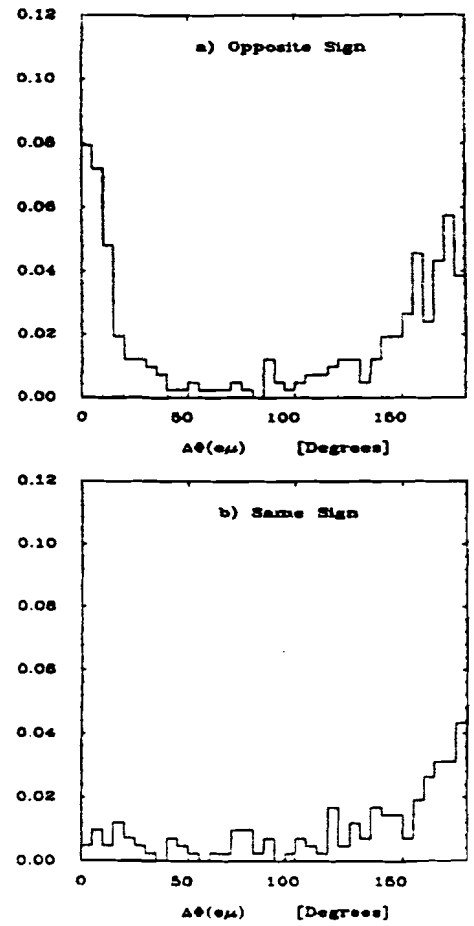

Figure 4.44: $\Delta\phi_{e\mu}$ for a) opposite-sign and b) same-sign, for CDF low-threshold data. The curves are normalized to $N_{opp} + N_{same}$.

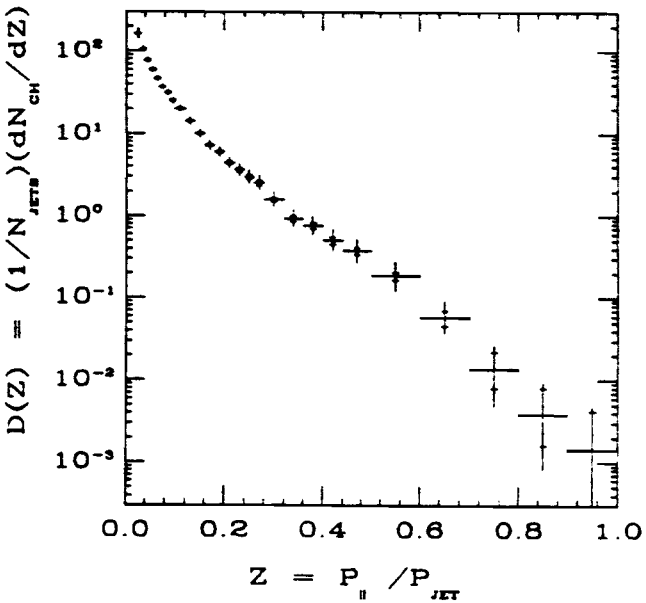

Figure 4.45: CDF jet fragmentation function, from reference [78].

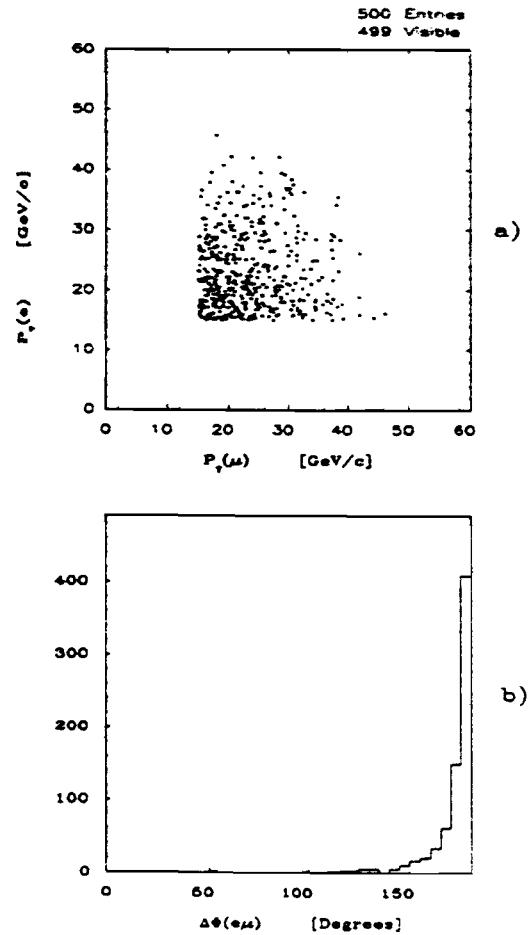

Figure 4.46: The distributions of a)E_T^e vs. P_T^μ, and b) $\Delta\phi_{e\mu}$, for $Z^0 \to \tau\tau \to e\mu + X$ events generated with $P_T^{min} > 15$ GeV/c.

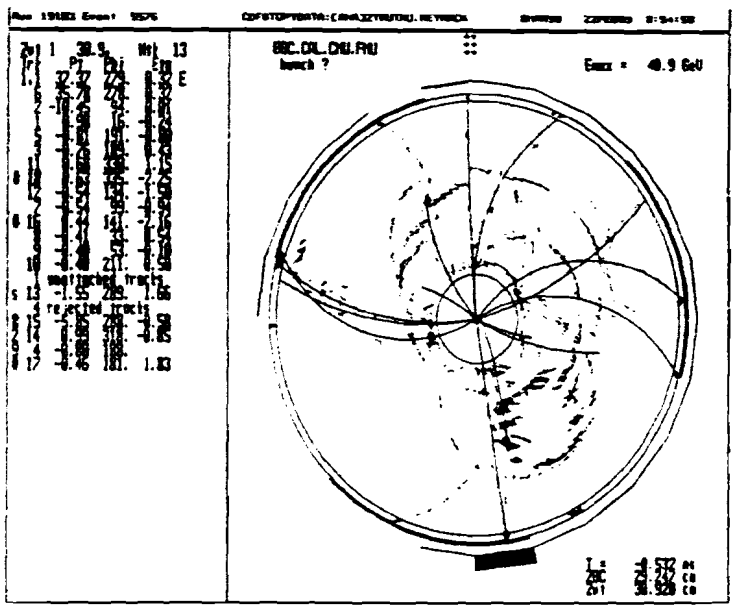

Figure 4.47: A CTC display of a the $Z^0 \to \tau\tau \to e\mu + X$ candidate event.

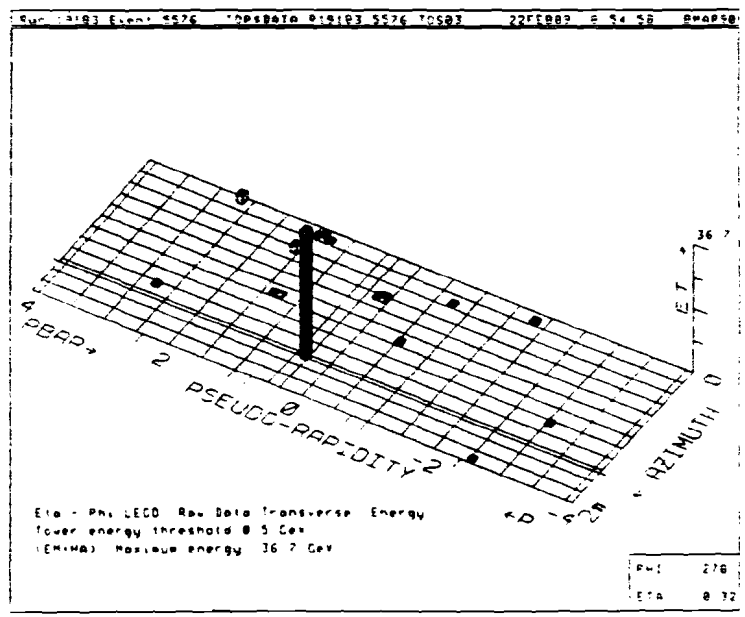

Figure 4.48: A calorimeter display of the $Z^0 \to \tau\tau \to e\mu + X$ candidate event.

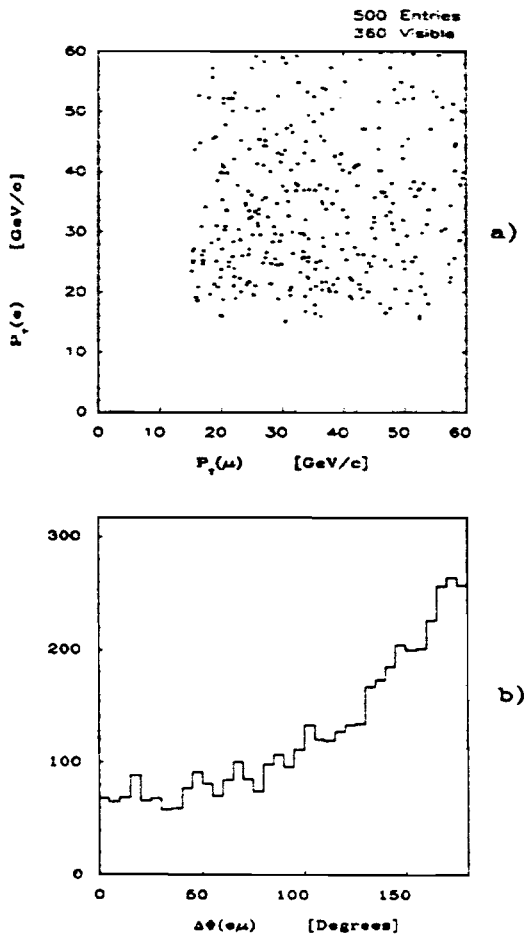

Figure 4.49: The distributions of a)$E_T^{\not{e}}$ vs. P_T^{μ}, and b) $\Delta\phi_{e\mu}$, for $WW \to e\mu + X$ events generated with $P_T^{min} > 15$ GeV/c.

Chapter 5

DATA ANALYSIS III : TOP QUARK MASS LIMITS

5.1 SYSTEMATIC UNCERTAINTIES

We now estimate the the various systematic uncertainties on the measured $t\bar{t} \to e\mu + X$ cross section, which is related to the number of $e\mu$ events in the signal region through the following equation :

$$\sigma_{t\bar{t}} \cdot Br = \frac{N_{t\bar{t}}^{e\mu}}{\int \mathcal{L}dt \cdot \epsilon_{Total}^{e\mu}} \tag{5.1}$$

Thus, systematic uncertainties arise from our limited knowledge of the integrated luminosity ($\int \mathcal{L}dt$) and of the $t\bar{t} \to e\mu + X$ detection efficiency ($\epsilon_{Total}^{e\mu}$).

Uncertainty in Luminosity

The integrated luminosity was measured using the beam-beam counters (Section 2.2.4). The portion of the inelastic $p\bar{p}$ cross section accepted by the BBC (about 74%), has been estimated to be $\sigma_{BBC} = (44 \pm 6)$ mb using extrapolations of lower energy data together with a Monte Carlo determination of the geometrical acceptance [52]. The systematic error in σ_{BBC} is propagated into the integrated luminosity, which is the ratio of the number of BBC East · West coincidences to the BBC cross section. For our data sample, $\int \mathcal{L}dt = 4.4$ pb^{-1} with a systematic uncertainty of 15%.

Uncertainty in the $t\bar{t} \to e\mu + X$ Detection Efficiency

The detection efficiency $\epsilon_{Total}^{e\mu}$ is listed in Table 4.5 for different values of M_{top}. Only statistical errors are included in Table 4.5; we now discuss the systematic uncertainties involved.

- Top Quark Fragmentation.

  Top-quark fragmentation affects the lepton isolation and thus has an impact on the lepton detection efficiency.

  To estimate the uncertainty in detection efficiency introduced by uncertainty in the fragmentation, the value of the ϵ parameter of the Peterson parametrization was changed in ISAJET from $\epsilon = 0.2/M_{top}^2$ to $\epsilon = 1.5/M_{top}^2$ and the effect on the electron identification efficiency was evaluated [79]. The larger value of ϵ resulted in a decrease in electron efficiency which we have multiplied by 2 to account for the muon in our analysis. This leads to uncertainties in the $e\mu$ detection efficiency of 30% and 10% for $M_{top} = 28$ GeV/c^2 and $M_{top} = 70$ GeV/c^2 respectively. This is a conservative estimate (overestimate), since the study of reference [79] used electron isolation cuts not applied in our analysis.

- Acceptance to Geometrical and P_T Cuts.

  Theoretical uncertainty in the η and P_T spectra of the leptons from top decay will result in a systematic uncertainty in the $t\bar{t} \to e\mu + X$ detection efficiency. In order to estimate such an uncertainty, we have compared the ISAJET and PAPAGENO calculations for $t\bar{t}$ production [80]. The acceptance for the signal region momentum and geometrical cuts ($\epsilon_{\eta,P_T}^{e\mu}$) is determined for each of the Monte Carlo calculations, and we find ~ 10 % agreement at high mass. At low top mass the agreement is less good: PAPAGENO gives a smaller acceptance, and it is found that the difference is due predominantly to the P_T cuts. We have taken our estimate of $\epsilon_{\eta,P_T}^{e\mu}$ to be the intermediate value between the ISAJET and PAPAGENO calculations, and we use half the difference in the acceptances as our estimate of the systematic uncertainty. The resulting uncertainties vary from 30% to 4% for 28 GeV/c^2 and 70 GeV/c^2 respectively.

- Lepton Selection.

  An additional uncertainty is associated with the knowledge of the efficiencies for isolated leptons (ϵ_{iso}^{e} and ϵ_{iso}^{μ}) which were determined in Chapter 3 for leptons from Z^0 decay, and were used as a factor in the determination of $\epsilon_{T_{total}}^{e\mu}$. We estimate a 4% flat uncertainty on this lepton selection, corresponding to sum in quadrature of the statistical uncertainties obtained from our Z^0 studies (Chapter 3) for electrons (3%) and muons (3%).

Total Systematic Uncertainty

Table 5.1 is a summary of the systematic uncertainties discussed above. We have also included a column with the Monte Carlo statistical error in the total efficiency (from Table 4.5). The various uncertainties are added in quadrature to obtain a total systematic error which varies from 48% to 20% from $M_{top} = 28$GeV/c^2 to 70 GeV/c^2. At high mass the systematic errors are dominated by the uncertainty in luminosity; at low mass the uncertainty from the acceptance to the geometrical and P_T cuts, and the uncertainty from the top quark fragmentation becomes more important.

5.2 LIMITS ON $t\bar{t}$ PRODUCTION

We now show how a 95% Confidence Level (CL) upper limit on the $t\bar{t}$ cross section is obtained. For clarity we begin with a simplified case without taking into account systematic uncertainties, and after that we carry out the complete derivation including the systematic uncertainties [81].

Ignoring the Effects of Systematic Errors

If systematic errors are negligible in a counting experiment such as our search for $t\bar{t} \to e\mu + X$ events, the result of the count is distributed according to the Poisson distribution:

$$P_u(n) = \frac{e^{-u}u^n}{n!} \qquad (n = 0, 1, 2, \ldots), \tag{5.2}$$

where the mean u is the average number of observed events over a large number of experiments.

Confidence levels for Poisson distributions are usually defined in terms of quantities called 'upper limits' : the CL associated with a given upper limit N and an observed value n_0, is the probability that $n > n_0$ if the mean of the distribution is $u = N$. In other words, if the mean of the Poisson distribution is greater or equal than the upper limit N, then the probability of observing n_0 or fewer events is lower tha or equal to 1−CL. In our case, we observe $n_0 = 1$ events, so the 95% CL upper limit on the number of $e\mu$ events will be the mean of the Poisson distribution giving 5% as the probability for observing 0 or 1 event. This means solving for N in the equation :

$$P_N(0) + P_N(1) = e^{-N} + Ne^{-N} = 0.05 \ . \tag{5.3}$$

The solution is $N_{t\bar{t}}^{e\mu}(95\%CL) = 4.74$ for 1 observed event, ignoring systematic errors.

Including the Effects of Systematic Errors

If we now include systematic uncertainties, the result of our counting experiment will no longer be distributed strictly as a Poisson. There will be a new distribution $\mathcal{P}_u(n,\sigma)$, and the quantity σ will reflect how much it deviates from the Poisson. The underlying distribution is still Poisson, and we assume that its mean will fluctuate according to a Gaussian with a standard deviation equal to the total systematic uncertainty σ :

$$G_{u,\sigma}(\xi) = Ce^{\frac{-(\xi-u)^2}{2\sigma^2}} \tag{5.4}$$

Here, $G_{u,\sigma}(\xi)$ is the probability for the average of the underlying Poisson to be between ξ and $\xi + d\xi$. The normalization $C = C(\sigma)$ is chosen so that $\int_0^\infty G_{u,\sigma}(\xi)d\xi = 1$, that is, the Gaussian has been truncated not to allow negative numbers of events. The new distribution is then the convolution of the Poisson and the Gaussian :

$$\mathcal{P}_u(n,\sigma) = \int_0^\infty P_\xi(n)G_{u,\sigma}(\xi)d\xi \ . \tag{5.5}$$

As before, the 95% CL upper limit on the number of events is determined for a given value of σ by solving for N in the equation :

$$\mathcal{P}_N(0,\sigma) + \mathcal{P}_N(1,\sigma) = 0.05 \ . \tag{5.6}$$

We have solved equation 5.6 numerically using the systematic uncertainties of Table 5.1. The result for the upper limit on the number of events is shown in Table 5.2. For instance, for a systematic uncertainty of $\sigma = 20\%$, we find $N_{t\bar{t}}^{e\mu}(95\%CL) = 5.15$ for 1 observed event. This is to be compared with the smaller solution of equation 5.3, where systematic errors were ignored.

The Upper Limit Cross Section

The upper limit on the number of events can be converted into an upper limit on the $t\bar{t}$ production cross section with the use of equation 5.1, namely :

$$\sigma_{t\bar{t}}(95\%CL) = \frac{N_{t\bar{t}}^{e\mu}(95\%CL)}{\int \mathcal{L}dt \cdot A_{t\bar{t}}^{e\mu}} \ , \tag{5.7}$$

where

$$A_{t\bar{t}}^{e\mu} = \frac{\sigma_{obs}^{e\mu}}{\sigma_{t\bar{t}}} = \epsilon_{Total}^{e\mu} \cdot Br \tag{5.8}$$

is the $t\bar{t} \rightarrow e\mu + X$ acceptance or ratio between the observed channel cross section and the total $t\bar{t}$ production cross section. The acceptances $A_{t\bar{t}}^{e\mu}$ are listed in Table 5.2, using the values for $\epsilon_{Total}^{e\mu}$ of Table 4.5 and the branching ratio $Br = \frac{2}{81}$. Also listed in Table 5.2 are the 95% CL upper limits on the $t\bar{t}$ cross section, together with the theoretical expectations [26,28].

Top Mass Limits

The 95% CL upper limit on the $t\bar{t}$ cross section is also shown in Figure 5.1, along with the theoretical prediction for $\sigma_{t\bar{t}}$. The 95% CL upper limit cross section curve intersects the lower edge of the theoretical calculation band at $M_{top} = 72$ GeV/c^2. We have chosen to terminate the analysis at 28 GeV/c^2 at the low end. As we have seen, below this mass, the efficiency for detecting the t quark becomes small

and the systematic uncertainties become large. Top quarks in the mass range 28 to 72 GeV/c^2 are thus excluded at the 95% confidence level.

5.3 LIMITS ON THE MASS OF THE b' QUARK

The $e\mu$ signature can also be used to search for the production of pairs of fourth-generation bottom quarks ($b'\bar{b}'$). The cross section for pair production of charge $-\frac{1}{3}$, b' quarks, would be the same as that for $t\bar{t}$ [82]. Assuming the b' decays via the charged current interaction into a virtual W and a light quark (u or c), the lepton spectrum would be slightly harder resulting in higher detection efficiency (See Figure 5.2). Our limit on the t quark mass is then applicable to the b' if it is lighter than the top quark and has a decay lifetime sufficiently short that its decay products appear to come from the interaction vertex. With the assumptions stated above, a b' quark in the mass range 28 to 72 GeV/c^2 is excluded at the 95% confidence level. The most recent lower limits from other experiments are $M_{b'} > 46$ GeV/c^2 at the 95% CL from of e^+e^- collisions [4] and $M_{b'} > 54$ GeV/c^2 at the 95% CL from $p\bar{p}$ collisions [7].

M_{top} [GeV/c^2]	Monte Carlo Acceptance (η, P_T)	Monte Carlo Statistics	Lepton Selection	Fragmentation	$\int \mathcal{L}dt$	Total
28	0.30	0.17	0.04	0.30	0.15	0.48
40	0.17	0.06	0.04	0.26	0.15	0.36
60	0.06	0.05	0.04	0.15	0.15	0.23
70	0.04	0.05	0.04	0.10	0.15	0.20
80	0.05	0.05	0.04	0.10	0.15	0.20
90	0.04	0.05	0.04	0.10	0.15	0.20

Table 5.1: The systematic uncertainties on the expected number of $t\bar{t} \to e\mu + X$ events as a function of M_{top}.

M_{top} [GeV/c^2]	$A_{t\bar{t}}^{e\mu}$ $\times 10^{-4}$	$N_{t\bar{t}}^{e\mu}(95\%CL)$	$\sigma_{t\bar{t}}(95\%CL)$ [pb]	$\sigma_{t\bar{t}}^{Theory}$ [pb]
28	1.6	8.42	11.9×10^3	$(58^{+13}_{-16}) \times 10^3$
40	6.4	6.57	2.33×10^3	$(9.63^{+1.7}_{-2.6}) \times 10^3$
60	20.5	5.32	0.592×10^3	$(1.27^{+0.19}_{-0.36}) \times 10^3$
70	29.9	5.15	392	556^{+194}_{-160}
80	41.2	5.15	284	285^{+37}_{-77}
90	50.1	5.15	234	150^{+20}_{-40}

Table 5.2: The upper limits on the number of $e\mu$ events and on the $t\bar{t}$ production cross section , together with the theoretical cross section. $A_{t\bar{t}}^{e\mu}$ is the $e\mu$ channel acceptance.

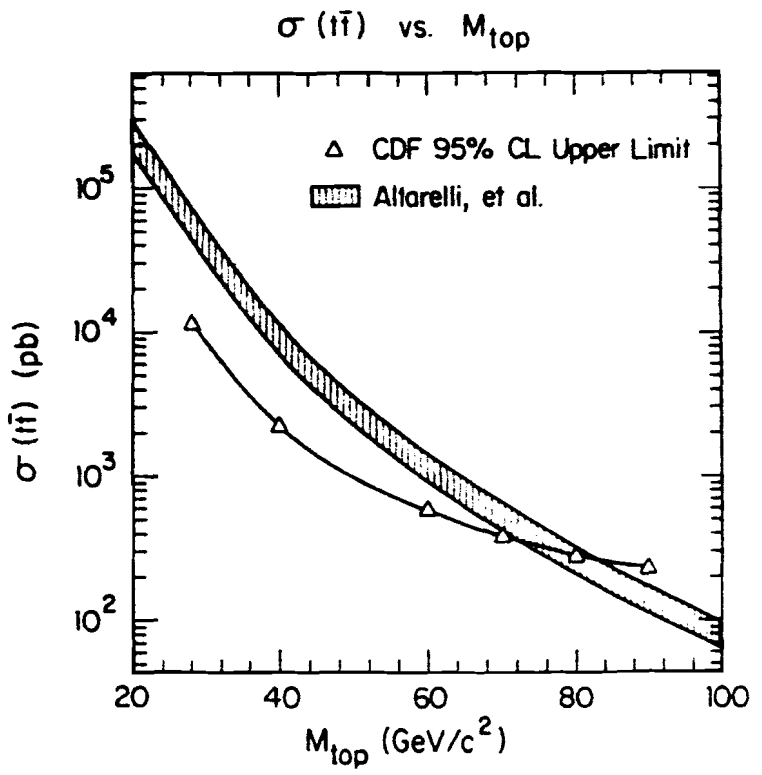

Figure 5.1: The 95% CL upper limit on the $t\bar{t}$ production cross section as a function of top quark mass. The shaded band shows the result of a theoretical calculation of the $t\bar{t}$ production cross section [26,28].

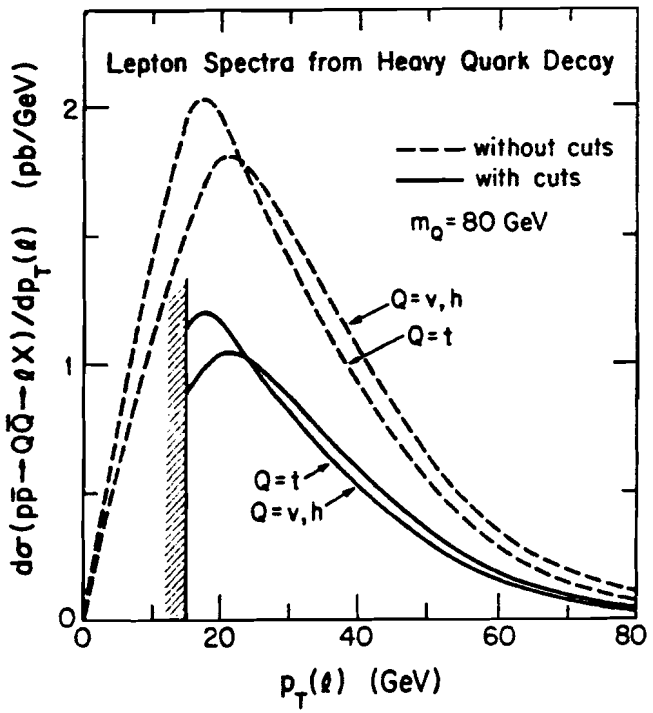

Figure 5.2: The spectrum for leptons from fourth generation, charge $-\frac{1}{3}$, b' quarks with charged current decays, compared to the spectrum of leptons from top decay. From reference [82].

Chapter 6

CONCLUSION AND OUTLOOK

We have exploited the good electron and muon identification capabilities of the CDF detector to carry out a search for the top quark in the $e\mu$ channel. We have shown that the $e\mu$ channel is very clean and hence a powerful tool for searching for the top, despite its low rate relative to other channels. No evidence for the top quark has been observed and our analysis excludes top quarks in the mass range 28 to 72 GeV/c^2 at the 95% CL. The same limits apply to a fourth-generation b' quark decaying via the charged current.

At this time, efforts continue at CDF to improve the sensitivity of the analyses. A natural extension of the $e\mu$ analysis, now including the ee and $\mu\mu$ dilepton modes, indicates that $M_{top} > M_W + M_{bottom}$, meaning that the top will decay into a real W boson and a bottom quark. With such a heavy top, the decay $Z^0 \to t\bar{t}$ is ruled out, and observing it is no longer possible at SLC or LEP-I. Chances for observation of the top at the CERN $p\bar{p}$ collider at $\sqrt{s}$ = 630 GeV are very slim because the decay $W \to t\bar{b}$ is now forbidden, and the remaining mechanism of direct production of $t\bar{t}$ pairs has a minute cross section. For the near future, prospects of discovery lie on the Fermilab Tevatron collider or at LEP-II. Searches at the LEP-II e^+e^- collider will be sensitive to top quark masses up to its beam energy of $\sim$ 100 GeV.

We now discuss the prospects of discovering the top quark at the Tevatron within the next few years. Two experiments, CDF and D0, are expected to be taking data simultaneously in consecutive runs projected for 1991 and 1993, with luminosities to tape of about 20 pb^{-1} and 100 pb^{-1} respectively. We base our discussion on estimates for the CDF detector. Two new hardware additions to CDF for 1991 will result in an improved sensitivity for the top. One is an upgrade

to the muon system. An intermediate muon system ($0.6 < |\eta| < 1.0$) will be added to allow better trigger acceptance and muon identification for all muon channels. Also, the central muon system will be upgraded with the addition of more steel for improved muon identification. The other is the installation of silicon microvertex detector (SVX) [83]. The SVX will open a new channel by making possible the identification of the B jet from the $t \to Wb$ decay. The B jets will be tagged by the presence of several tracks with large impact parameters. The device has an expected impact parameter resolution of 30 μm for 1 GeV/c tracks and of 10 μm for tracks with 10 GeV/c or above. This is to be compared with the B meson lifetime ($c\tau_B$) of 300 μm. Overall B-tagging efficiencies of $\sim$ 20% are expected for B jets with $P_T > 30$ GeV/c [84,85].

In Table 6.1 the $t\bar{t}$ production cross section is shown together with the estimated detected cross sections in the $e\mu$ channel and in the $l(e$ or $\mu)+$ jets channels. For the $e\mu$ channel we used our estimated signal region acceptances of 0.5% at 90 GeV/c^2 and 0.6% for 100 GeV/c^2 or larger. The main backgrounds for the $e\mu$ channel come from $Z^0 \to \tau\tau \to e\mu + X$ with a cross section of 0.26 pb, and from $WW \to e\mu + X$ with a cross section of 0.039 pb. Both backgrounds can be subtantially reduced with little effect on the $t\bar{t} \to e\mu + X$ signal by requiring some jet activity. In addition, the characteristic softer dilepton spectrum and back-to-back topology of the Z^0 decays further supress this background by large factors, with a small effect on the signal.

We have based our estimate for the $l+$ jets case on the $e+$ jets Monte Carlo study of reference [86], and have scaled the acceptance to include muons. The $l+$ jets selection requires P_T^l >20 GeV/c, $E_T^{miss} > 20$ GeV, and at least 2 jets with observed $E_T^{jet} > 20$ GeV. The acceptance for this selection ranges from $\sim$ 4% to 9% from 90 GeV/c^2 to 200 GeV/c^2. The $W+$ jets background for this channel has a cross section of $\sim$ 9 pb (as determined from the rates in our present CDF data), compared for example to 2.4 pb for the $t\bar{t}$ signal at M_{top}=120 GeV/c^2, so additional background rejection is needed. Raising the jet Et threshold and/or requiring more jets will help improve the signal to noise ratio. For a large statistics run, a presence of $t\bar{t}$ events in the $l+$ jets sample may be established by using the

jet multiplicity of the $Z+$ jets events to determine the contribution of $W+$ jets. Since in the $t\bar{t}$ events there will be a real W decaying into two quarks, searching for an excess of dijet masses near the W mass is also a possibility. We believe that a clean and promising way of establishing a $t\bar{t}$ signal in the $l+$ jets sample is to use the SVX to tag at least one B from the $t\bar{t}$ decay. A similar method, with less acceptance and with perhaps larger background, is to tag the B by its decay into a second soft lepton.

In Table 6.2 we show estimates of the number of events detected in our favorite two channels, $e\mu$ and $l+$ jets + B_{tag}, for the integrated luminosities expected for the CDF runs in 1991 and 1993. We have used B-tagging efficiencies of 20% for $M_{top} \geq 120$GeV/c^2; at 90-100 GeV/c^2, where the B jets are softer, we used 5-10%.

We believe that $\sim$ 4 events in the $e\mu$ channel, together with $\sim$ 2 events from ee and $\mu\mu$ (after Z^0 removal cuts) and accompanied by additional supporting evidence from the $l+$ jets, will be sufficient to establish the discovery of the top quark. It thus appears that the top quark will be observed at the Tevatron 1991 run if $M_{top} < 120$ GeV/c^2, and in the 1993 run if $M_{top} < 160$ GeV/c^2. If the silicon vertex detector operates succesfully, with the anticipated efficiencies, then it will be possible to stretch the sensitivity to top quarks as heavy as 140 GeV/c^2 in the 1991 run and 180 GeV/c^2 in the 1993 run. If the top has not been discovered by then, we will have to wait for future intense luminosity runs at the Tevatron or for future accelerators such as the Large Hadron Collider (LHC) (pp, $\sqrt{s}$ = 20 TeV) or the Superconducting Supercollider (SSC) (pp, $\sqrt{s}$ = 40 TeV).

M_{top} [GeV/c^2]	$\sigma_{t\bar{t}}$ [pb]	$\sigma_{t\bar{t}}^{e\mu}$ [pb]	$\sigma_{t\bar{t}}^{l-jets}$ [pb]
90	150	0.75	6.6
100	87	0.55	4.6
120	33	0.21	2.4
150	10	0.063	0.80
180	3.5	0.021	0.30
200	1.9	0.012	0.17

Table 6.1: The total $t\bar{t}$ production cross section, together with estimates of the CDF detected cross sections into the $e\mu$ and $l-jets$ channels.

	Events in 20 pb^{-1}		Events in 100 pb^{-1}	
M_{top} [GeV/c^2]	$e\mu$	$l-jets-B_{tag}$	$e\mu$	$l-jets-B_{tag}$
90	15	13	75	63
100	11	18	55	88
120	4.2	17	21	86
150	1.3	6	6.3	28
180	0.4	2	2.1	11
200	0.2	1	1.2	6

Table 6.2: The estimated number of detected $e\mu$ events, and of $l-jets$ events with at least one B jet tagged by the silicon vertex detector, for integrated luminosities of 20 pb^{-1} and 100 pb^{-1}.

References

[1] D. Decamp *et al.*, Phys. Lett. B235, 399 (1990).

[2] T. Kamae, Proceedings of the XXIV International Conference on High Energy Physics, Munich (1988), edited by R. Kotthaus and J. Kuhn, Springer-Verlag (1989), p. 156.

[3] C. Albajar *et al.*, Z. Phys. C37, 505 (1988); I.J. Kroll, Proceedings of the XXIV International Conference on High Energy Physics, Munich (1988), edited by R. Kotthaus and J. Kuhn, Springer-Verlag (1989), p. 1416.

[4] D. Decamp *et al.*, Phys. Lett. B236, 513 (1990).

[5] Results of a Top Quark search in the Electron – Jets channel at $\sqrt{s}$ = 1.8 TeV, F. Abe *et al.*, Phys. Rev. Lett. 64, 142 (1990).

[6] A Search for New Heavy Quarks in Electron-Muon Events at the Fermilab Tevatron Collider, F. Abe *et al.*, Phys. Rev. Lett. 64, 147 (1990).

[7] T. Akesson *et al.*, submitted to Z. Phys., F. Abe *et al.*, Phys. Rev. Lett. 64, 147 (1990).

[8] W. Bartel *et al.*, Phys. Lett. 146B, 437 (1984).

[9] S. Wu, Proceedings of the Lepton Photon Symposium, Hamburg (1987), edited by W. Bartel and R. Ruckl, p. 39.

[10] H. Albrecht *et al.*, Phys. Lett. 192B, 245 (1987).

[11] G. Kane and M.Peskin, Nucl. Phys. B195, 29 (1982).

[12] A. Bean *et al.*, Phys. Rev. D35, 3533 (1987).

[13] C. Albajar *et al.*, Phys. Lett. 186B, 247 (1987).

[14] M. Artuso *et al.*, Phys. Rev. Lett. 62, 2233 (1989).

[15] M. Kobayashi and T. Maskawa, Progr. Theor. Phys. 49, 652 (1973).

[16] G. Altarelli, P. Franzini, Z. Phys. C37, 271 (1988).

[17] J. Ellis *et al.*, Nucl. Phys. B304, 205 (1988).

[18] W. Marciano and A. Sirlin, Phys. Rev.D29, 945 (1984).

[19] D. Bardin *et al.*, Z. Phys. C32, 121 (1986).

[20] U. Amaldi *et al.*, Phys. Rev.D36, 1385 1987.

[21] P. Langacker, Phys. Rev. Lett. 63, 1920 (1989).

[22] H. Abramowicz *et al.*, Phys. Rev. Lett. 57, 298 (1986).

[23] J. Allaby *et al.*, Phys. Lett. B177, 446 (1986).

[24] Abrams *et al.*, Phys. Rev. Lett. 63, 724 (1989).

[25] M. Campbell, in Proceedings of the Fourteenth International Symposium on Lepton Photon Interactions, Stanford, California, August 1989 (to be published).

[26] P. Nason, S. Dawson and R.K. Ellis, Nucl. Phys. B303, 607 (1988).

[27] R.K. Ellis, Proceedings of the 7th Topical Workshop on Proton-Antiproton Collider Physics, Fermilab (1988), edited by R. Raja, A. Tollestrup, and J. Yoh, World Scientific (1989), p. 639.

[28] G. Altarelli, M. Diemoz, G. Martinelli and P. Nason, Nucl. Phys. B308, 724 (1988).

[29] M. Diemoz, F. Ferroni, E. Longo, G. Martinelli, Z. Phys. C39, 21 (1988).

[30] C. Peterson, D. Schlatter, I. Schmitt and P. Z. Zerwas, Phys. Rev. D27, 105 (1983).

[31] V. Barger and R. Phillips, Collider Physics, Addison-Wesley Publishing Company (1987).

[32] J. Rosner, in Proceedings of the 1988 Banff Summer Institute, edited by A. Kamal and F. Khanna, World Scientific (1989).

[33] W. Kwong, L. Orr and J. Rosner, Lepton Pairs from Heavy Quarks Produced in Hadron Colliders, IASSNS-HEP 88/45, submitted to Phys. Rev. D.

[34] J. Bensinger, P. Kesten, S. Tarem, A Study of Hadronic Top Decay Events Using Event Shape Measures, CDF-1036 (1989).

[35] The Particle Data Group, G.P. Yost *et al.*, Phys. Lett. B204, 74 (1988).

[36] H. Edwards, Ann. Rev. Nucl. Part. Sci. 35, 605 (1985).

[37] R. Johnson, in Proc. of the 12-th Particle Accelerator Conference, Washington, D.C. (1987).

[38] G. Dugan, in Proc. of the 1989 IEEE Particle Accelerator Conference, Chicago, IL (1989).

[39] F. Abe *et al.*, Nucl. Instrum. Methods A271, 387 (1988).

[40] F. Snider *et al.*, Nucl. Instrum. Methods A268, 75 (1988).

[41] F. Bedeschi *et al.*, Nucl. Instrum. Methods A268, 54 (1988).

[42] L. Balka *et al.*, Nucl. Instrum. Methods A267, 272 (1988).

[43] F. Abe *et al.*, Phys. Rev. Lett. 63, 720 (1989).

[44] N. Solomey and B. Wicklund, Study of Electromagnetic Showers in the CDF Central Electromagnetic Calorimeter Strip Chamber, CDF-247 (1984).

[45] S. Bertolucci *et al.*, Nucl. Instrum. Methods A267, 301 (1988).

[46] K. Byrum *et al.*, Nucl. Instrum. Methods A268, 46 (1988).

[47] G. Ascoli *et al.*, Nucl. Instrum. Methods A268, 33 (1988).

[48] D. Smith, Study of Muons Associated with Jets in Proton-Antiproton Collisions at $\sqrt{s}$ = 1.8 TeV, PHD Thesis, University of Illinois at Urbana-Champaign (1989).

[49] T. Westhusing, Observation of $W \rightarrow \mu\nu$ decays in Proton-Antiproton Collisions at $\sqrt{s}$ = 1.8 TeV, PHD Thesis, University of Illinois at Urbana-Champaign, (1989).

[50] D. Amidei *et al.*, Nucl. Instrum. Methods A269, 51 (1988).

[51] H. Frisch *et al.*, Beam-beam counters for CDF, CDF-250 (1984).

[52] T.Liss , Luminosity Monitoring and Beam-Beam Counter Performance, CDF-552 (1988).

[53] G. Foster *et al.*, Nucl. Instrum. Methods A269, 93 (1988).

[54] E. Barsotti *et al.*, Nucl. Instrum. Methods A269, 82 (1988).

[55] T. Carroll *et al.*, The CDF Level-3 Trigger, CDF-895 (1989).

[56] J. Hauser, Guide to the Triggers Used in the 1988-1989 CDF Data Run, CDF-966 (1989).

[57] J. Proudfoot, A Central Electron Filter for Level 3, , CDF-633 (1988).

[58] M. Contreras, G.W.Foster, G.P.Yeh, A Search for T + Tbar → e + mu, CDF-881 (1989).

[59] J. Proudfoot, Central Electron 12 GeV Trigger Efficiency, CDF-1008 (1989).

[60] A. Gauthier, Milestones of the Central Muon Trigger, CDF-1029 (1989).

[61] A. Gauthier, Efficiency of the Level 1 Central Muon Trigger, CDF-937 (1989).

[62] A. Gauthier, Efficiency of the Level 2 Central Muon Trigger, CDF-1106 (1989).

[63] C. Campagnari *et al.*, Running Production on the Spin Output. CDF-794 (1988).

[64] A. Baden *et al.*, CDF ACP Production, CDF-845 (1988).

[65] A. Baden *et al.*, The V5.1 Production Package, CDF-955 (1989).

[66] J. Proudfoot, Electron Identification in the CDF Central Calorimeter, CDF-935 (1989).

[67] We thank Fumihiko Ukegawa for providing the description of the strip chamber χ^2 variables.

[68] K. Ragan, J. Walsh and H. Williams, Identification of Photon Conversions, CDF-902 (1989).

[69] M. Gold, Identification of Conversion Electron Pairs, CDF-913 (1989).

[70] J. Walsh, Top Quark Search in the Electron + Jets Channel, PHD Thesis, University of Pennsylvania (1990).

[71] F. Paige and S.D. Protopopescu, BNL Report No. BNL 38034, 1986 (unpublished).

[72] J. Freeman, Proceedings of the Workshop on Detector Simulation for the SSC, edited by L. E. Price, Argonne National Laboratory (1987), p. 190.

[73] I. Hinchliffe, note in preparation.

[74] The ISALEP version of ISAJET was first developed by UA1. Frank Paige has made the program available to CDF.

[75] E. Eichten, I. Hinchliffe, K. Lane and C. Quigg, Rev. Mod. Phys. 56 (1984) 579; (E) 58 (1986) 1065.

[76] F. Ukegawa and B.Wicklnnd did the D^0 analysis. Note in preparation.

[77] E. Thorndike and R. Poling, Phys. Rep. 157, 183 (1988). P. Tipton and E. Thorndike, CLEO internal note CBX 87-26.

[78] B. Hubbard, Jet Fragmentation Properties in $p\bar{p}$ collisions at $\sqrt{s} = 1.8$ TeV, PHD Thesis, University of California at Berkeley (1990).

[79] We thank Pekka Sinervo and John Walsh for making available the results of their fragmentation study.

[80] M. Austern and L. Galtieri, Top Cross Section and Acceptance Studies for $e\not{p}$ and $e + jets$ Channels, CDF-1007 (1989).

[81] We thank Cathy Newman Holmes for pointing out this method, and for providing a computer program for the calculations.

[82] V. Barger and R. J. N. Phillips, University of Wisconsin - Madison Preprint MAD/PH/508 (1989).

[83] C. Haber, The CDF Silicon Microstrip Vertex Detector, in Proceedings of the 7th Topical Workshop on Proton-Antiproton Collider Physics. Edited by R. Raja, A. Tollestrup and J. Yoh, World Scientific (1989).

[84] F. Bedeschi *et al.*, Silicon Vertex Detector Simulation, Tracking, Physics Estimates; CDF-601 (1988).

[85] F. Bedeschi, Private Communication.

[86] P. Sinervo. Breckenridge meeting (1989).